PLASMONIC METAMATERIALS AS AN OPTOELECTRONIC PLATFORM FOR ACTIVE AND NONLINEAR NANOPHOTONICS

A Dissertation
Presented to
The Academic Faculty

by

Shoufeng Lan

In Partial Fulfillment
of the Requirements for the Degree
Doctor of Philosophy in the
School of Electrical and Computer Engineering

Georgia Institute of Technology
May 2017

PLASMONIC METAMATERIALS AS AN OPTOELECTRONIC PLATFORM FOR ACTIVE AND NONLINEAR NANOPHOTONICS

Approved by:

Dr. Wenshan Cai, Advisor
School of Electrical and Computer Engineering
Georgia Institute of Technology

Dr. Michael Filler
School of Chemical and Biomolecular Engineering
Georgia Institute of Technology

Dr. Ali Adibi
School of Electrical and Computer Engineering
Georgia Institute of Technology

Dr. Azad Naeemi
School of Electrical and Computer Engineering
Georgia Institute of Technology

Dr. Bernard Kippelen
School of Electrical and Computer Engineering
Georgia Institute of Technology

Date Approved: May 2017

To my wife Peizhen, my son Chris, and the rest of my family,

without whom this work would not be possible.

ACKNOWLEDGEMENTS

Five years ago, I drove more than a thousand miles from Albuquerque to Atlanta to seek my Ph.D. degree at the Georgia Institute of Technology. I expected Georgia Tech to be a great place to perform scientific research, but I didn't expect it to become my home. So many people came out of the way to be kind, generous, and helpful. Thank you to you all.

Many, many thanks to my advisor and mentor, Professor Wenshan Cai. He combines a passion for research with unparalleled intelligence and a genuine concern for the well-being of his students. I am indebted to him for taking me into his group, and teaching me how to carry out research, to communicate ideas with other people, to have a vision of the scientific future, and to be a great human being in general. I still remember the days he taught me hand-by-hand how to set up experimental systems, to conduct numerical simulations, to generate beautiful artworks, and to write a journal paper word by word. The strong scientific foundation that he has given me will continue to guide and inspire me in my future career. It has been a true privilege to work for him, and I will always be grateful for all that he has taught me in the past five years.

I also owe a deep debt of gratitude to Professor Ali Adibi. His generosity over the past five years has been boundless, while, like a bad parasite, I was bugging him for all kinds of support for scholarships, awards, job positions, and so on. His kind support also acts in my research, in the classroom, in the OSA student chapter I served, in the conferences I attended, and all other places. I am truly grateful for his most generous support all these years.

Many thanks to the faculty and funding agencies who have provided me with the opportunity to pursue a Ph.D. degree. I would like to thank my proposal committee, including Professors Ali Adibi, Michael Filler, Bernard Kippelen, and Wenshan Cai, for their valuable advice and input. Their feedbacks and suggestions steered my Ph.D. research in the right direction. I would also like to thank my defense committee, including Professors Ali Adibi, Michael Filler, Bernard Kippelen, Azad Naeemi, and Wenshan Cai, for their generosity and kind support. Their insights are particularly helpful for my current and the future research. I have also had the opportunity to learn Integrated Photonics from Professor Adibi and Nanoelectronics from Professor Naeemi. Both classes have been inspiring. In addition, I would greatly acknowledge funding agencies, Georgia Institute of Technology, National Science Foundation (NSF), Air Force Office of Scientific Research (AFOSR), OPe. LLC, and CooperVision, and scholarships from the Materials Research Society (MRS), the International Society for Optics and Photonics (SPIE), and the Chinese Scholarship Council.

I am indebted to the dedication of my labmates, Lei Kang, Yonghao Cui, Sean Rodrigues, Mohammad Taghinejad, Kyutae Lee, Xueyue Zhang, Shengxiang Wang, and Jiahao. Your ideas have greatly inspired me, your kind assistances have made my life easy, and I have learned a lot from you in terms of experimental skills, fabrication techniques, numerical simulations, and so on. Thank you so much for being such a great team.

Of course, this thesis would not be possible without the unconditional support of my family. Words cannot express how grateful I am to my parents and my wife, who

sacrificed so much so that I could pursue my personal dreams. I am also indebted to my son, Chris, for his love and understanding.

I have consistently been humbled and amazed by the quality of Georgia Tech's faculty and students. I am grateful to the entire Georgia Tech community for providing me with a most memorable graduate experience.

Shoufeng Lan

February 2017

Atlanta, GA

TABLE OF CONTENTS

LIST OF FIGURES

LIST OF SYMBOLS AND ABBREVIATIONS

SYMBOLS

ω	Angular Frequency
n	Index of Refraction
η	Ellipticity
S	Poynting Vector
k	Wave Vector
λ	Wavelength
χ	Susceptibility
ϕ	Potential

ABBREVIATIONS

SHG	Second Harmonic Generation
OR	Optical Rectification
EFISH	Electric-Field-Induced Second Harmonic
EFIOR	Electric-Field-Induced Optical Rectification
TPPL	Two-Photon Photoluminescence
TE	Transverse Electric
TM	Transverse Magnetic
NIM	Negative-Index Material
SEM	Scanning Electron Microscopy
ALD	Atomic Layer Deposition

SUMMARY

The ultimate goal of this thesis was to develop meta-structured devices that simultaneously sustain both electrical and optical functionalities. To achieve this goal, this research focused on nonlinear optical phenomena to generate, modify or detect optical signals by applying electrical biasing. Metamaterials offer a unique platform to spur these optical phenomena due to their composition of nanostructured metals that provide strong spatial confinement of surface plasmon polaritons, thereby harnessing enormous energy densities on their surfaces. The metals serve a secondary function as electrodes for the extraction or manipulation of nonlinear optics in the media. Several applications of these devices are demonstrated herein. A diatomic plasmonic grating with alternate widths for the adjacent stripes was designed for not only the excitation of dark modes featured with an ultrasharp spectrum but also the generation of an electric potential via a plasmoelectric effect. An electrically tunable second-harmonic signal and optical rectification are both realized from a perfect absorber metamaterial. Beyond the solid state structures, electrically tunable harmonic generation was also demonstrated from plasmonic metamaterials in electrolyte solutions. Moreover, by applying electrically induced nonlinear optics, this thesis demonstrated a decade-old prediction, backward phase-matching in negative-index materials, using a plasmonic waveguide scenario. The results revealed the potential of plasmonic metamaterials as self-contained, dynamic electrooptic systems with intrinsically embedded electrical functions and exotic optical properties for signal processing, light switching, and sensing applications.

CHAPTER 1

INTRODUCTION

1.1 Nonlinear optics

Light with massless photons at high frequency can interact with matter to offer the ultimate means of carrying information with unparalleled data speed. When the flow of light is strong enough that the electromagnetic field is comparable with the atomic field, the light-matter interaction can be described by nonlinear processes. Here the term 'nonlinear' in the optical realm refers to the phenomenon that the induced polarization depends upon more than just the first power of the electric and magnetic field.

In 1961, Franken *et al.* observed a new nonlinear optical effect by generating the harmonic wave of a ruby laser with a quartz crystal [1], which was made possible by the production of monochromatic light beams of exceedingly high intensity [2]. At about the same time, Kaiser *et al.* reported a nonlinear luminescence with two-photon excitation [3]. Later the field of nonlinear optics was populated with other phenomena like four-wave mixing [4], sum- and difference-frequency generation [5, 6], surface harmonics and nonlinear light scattering [7, 8]. An important extension of nonlinear optical interactions is the optical parametric amplification observed in 1965 by Wang and Giordmaine separately [9, 10], with the theoretical investigations on the possibility of parametric gain being conducted by Kroll and other researchers [11]. Optical parametric amplification enables the radiation generated in a nonlinear crystal continuously variable over a considerable range.

The phase-matching condition, resulting from the conservation of photon momentum, is among the most vital aspects to consider when multiple frequencies are mixed in bulk nonlinear media. Strictly speaking, all materials are dispersive and the conversion efficiency of a nonlinear process is critically dependent on the relationship among the wave vectors involved. Taking second harmonic generation (SHG) as an example, phase-matching implies a wave-vector relation of $k_{2\omega} = 2k_{\omega}$ or a refractive index relation of $n_{2\omega} = n_{\omega}$. To achieve these parameters, the orientation or temperature of a nonlinear crystal must be fine-tuned [12], or an approximation can be reached by flipping the crystal axis in a periodic manner [13-15]. The specific scheme to fulfill the phase-matching requirement is critically dependent on the optical properties of the nonlinear medium, such as the material's chromatic dispersion, crystal anisotropy, wave-guiding characteristics, and thermal coefficient of the refractive index [16].

Under the electric-dipole approximation, where the relevant wavelengths are very much larger than atomic dimensions, the symmetry restriction is another vigorous concern for efficient even-order nonlinear conversion [17]. Basically, the nonlinear polarization is reversed with the reversal of the applied electric field when isotropy or a center of inversion is present, regardless of the complexity of the tensor relationship between them. To comply with this, the even order nonlinear susceptibility must vanish and thus preclude the even order nonlinear process in centrosymmetric materials [18].

1.2 Electrically active nonlinear optics

Light waves involved in nonlinear optics can be described as an oscillation of the electromagnetic field at an extremely fast speed. It would be quite reasonable to wonder

how nonlinear light-matter interactions react under a static field, so that active control can be embedded into the nonlinear process. Indeed, only one year after the first demonstration of the SHG in a ruby laser, an electric field induced second harmonic (EFISH) wave was discovered by applying a voltage on the calcite crystal [19].

1.2.1. Electric-field-induced second-harmonic generation

The EFISH signal is characterized by a quadratic relationship to the fundamental intensity but varies little with input angle, as opposed to the regular SHG whose signal changes sharply with angle due to the index-matching condition. While the regular SHG ($\omega + \omega \rightarrow 2\omega$) relies on the second order nonlinear susceptibility $\chi^{(2)}$, the EFISH generation ($\omega + \omega + 0 \rightarrow 2\omega$) is a third order nonlinear process enabled by an externally applied static or low-frequency field. As a result, the strict limitation of SHG in centrosymmetric materials is principally relaxed. Instead, the generation of the EFISH signal is possible in all materials, because of the ubiquity of the third-order susceptibility $\chi^{(3)}$. The technique of generating EFISH by actively involving a *dc* electric field has been used in electro-optic applications such as the characterization of organic nonlinear materials and the ultrafast detection of electrical signals in semiconductors. However, since the third-order nonlinear susceptibility $\chi^{(3)}$ is orders smaller than $\chi^{(2)}$, a gigantic voltage (kilovolts) has to be sacrificed to generate detectable EFISH in bulky optical crystals. Fortunately, EFISH in nanostructure changes the story, thanks to the nanometer scale separation between the two metallic electrodes in a plasmonic cavity filled with polymer [20]. With both second- and third-order nonlinear susceptibilities in the

dielectric medium, voltage-dependent nonlinear generation can reach a normalized magnitude of ~7% per volt under a moderate applied bias.

1.2.2. Electric-field-induced optical rectification

Similarly to SHG, the nonlinear optical rectification (OR, $\omega - \omega \rightarrow 0$) is a second- order nonlinear interaction, which is typically limited to crystals lacking a center of inversion symmetry. In analogy with the *dc* current in an electronic rectifier, a net time-averaged polarization is induced during the OR process, which can be qualitatively understood with the induced polarization from a sinusoidal electric field in a crystal with low symmetry needs not to be canceled by that with the applied field reversed [21]. The electric field induced optical rectification (EFIOR, $\omega - \omega + 0 \rightarrow 0$) was first demonstrated in 1977 by applying a potential difference of ~10 kilovolts across a centrosymmetric nonlinear medium sandwiched between two electrodes [22]. The applied electric field removes the center of symmetry and induced a *dc* polarization via the third-order nonlinear optical process. The exact solution of EFIOR was obtained in terms of Stokes parameters by solving the propagating wave equations [23]. Although both SHG and OR were discovered during the early days of nonlinear optics in the 1960s, OR received very limited attention for decades until being revived as a major scheme for generating terahertz radiation [24-26].

1.3 Plasmonics and metamaterials

Plasmonics confined to the surface is a result of the interaction between photons and free electrons. The plasmonic effect has been exploited by glass makers to generate colors since the fourth century, but the scientific investigation was not started until the

early 1900s [27]. After more than 50 years, Kretschmann and Otto laid the foundation for the experimental study by exciting the surface plasmonics with prism attached to metal surface [28, 29]. It is further developed to enhance Raman scattering of light from molecules on rough silver surface in 1970s [30]. With this effect, molecular concentrations down to the single-molecule level can be detected.

Modern plasmonics began with the observation of extraordinary opical transmission from a perforated metal thin film with holes ten times smaller than the wavelength of light [31]. The authors were able to explain the phenomena as a surface plasmon polariton (SPP), which is an interaion that couples photons to the free electrons in the metal. The ability to concentrate the light into minuscule structures enables the design of plasmonic components to pass the conventional diffraction limit [32-47]. In addition, plasmonic lasers realized with quantum dots or nanowires provide the coherent plasmonic light source demanded for nanocircuits [48, 49]. Plasmonics facilitated with dramatic enhancements of localized field intensity have also been investigated in the nonlinear optical regime [50-55]. Furthermore, plasmonic elements are widely used as functional unit cells in electromagnetic metamaterials whose properties can be designed at will via structural engineering [56].

The key for metamaterials to obtain electromagnetic properties expressed in terms of homogenized material parameters is to tailor the structural unit cells in a scale smaller than the wavelength of light. Metamaterials possess properties not found in nature in the linear regime, such as a negative refraction, but can also have added effects when submitted to nonlinear light-matter interactions. Take second harmonic generation as an example, the structural symmetry required is naturally broken with the disparity between

the two media composing the boundary by engineering of the unit cells. The field discontinuity with the rapid variation of the electric field normal to the surface, known as the electric-quadrupole contribution [57], further breaks the symmetry at the surface. Moreover, the unprecedented properties in metamaterials hold the potential to design novel phase-matching conditions for SHG [58].

1.4 Example of the exotic properties: Negative index of refraction

The refractive index described as an imaginary number $n = n' + n''$ is the formula for optics. While the imaginary part n'' designates the light absorption, the real part n' characterizes the phase velocity of light in the medium compared to that in vacuum. A negative index of refraction, meaning the real part is negative, represents a phase velocity directs against the flow of energy. This is highly unusual in the standpoint of conventional optics described in Maxwell's equations. However, it did not stop scientists, such as Dr. Veselago, pursuing the physics with exotic phenomena even lacking an actual material long time ago [59]. The prediction of the negative-index based superlens by Sir John Pendry [60] was revolutionary to the field, and opened the gateway of an entirely new era for the metamaterial [61, 62]. Later, the negative index was experimentally demonstrated in the optical range with pairs of metal rods and pairs of dielectric voids in metals nearly at the same time [63, 64]. The negative index was also realized at visible frequencies with a plasmonic waveguide [65].

CHAPTER 2

DARK PLASMONIC MODES IN DIATOMIC GRATINGS FOR PLASMOELECTRONICS

2.1. Overview

Energy harvesting and concentration at the nanoscale is at the root of unique capacities that nanophotonics offers for diverse applications ranging from light generation to optical modulation and photon detection. The development of new materials or structures for the manipulation of light in a highly unconventional manner has revolutionized the paradigm of photonics and optoelectronics [66-68]. Along this avenue, metallic nanostructures provide us with the means to collect and process optical energy through intense photon-charge interactions at the interface, thanks to the excitation of surface plasmon polaritons (SPP). The strong spatial confinement of SPP results in enormous energy density on surfaces of metallic structures, which in turn ensures the potential application of SPP for miniature optical components, devices, and systems. Since the turn of the century, the field of plasmonics has enjoyed sustained activity, which has not only enabled a wide range of unprecedented functionalities with a minimal device footprint [31, 32, 45, 47, 69], but also served as a versatile means for the exploration of light-matter interactions at the nanoscale [40, 55, 70, 71]. While it is common practice to design and implement plasmonic structures with tailored resonance behavior at a prescribed frequency range, the intrinsic damping of light energy in a plasmonic metal usually leads to spectral broadening of SPP resonances yielding a typical linewidth of ~50 nm in the visible and near-infrared regions [56, 72-79], hindering many

potential applications of plasmonics such as biochemical sensing and emission control. Therefore, the development of novel plasmonic systems with extremely sharp spectral features beyond what typical dipole-based resonances offer has become an urgent need.

Extremely sharp spectral features can be achieved by employing metallic nanostructures that support subradiant modes, as they can suppress radiative loss by not coupling to the continuum [80, 81]. A dark mode is an electromagnetic eigenmode that has a vanishing net electric dipole moment. Photons in a dark mode experience a long lifetime, which results in a high quality factor (Q) of the resonance, and therefore a narrow spectral linewidth. This unique feature makes dark modes an ideal candidate for applications such as enhanced biochemical sensing and optical filtering. Dark modes are also situated at the center of many novel optical phenomena including Fano resonance (FR) and electromagnetically induced transparency (EIT) [82, 83]. On the other hand, dark modes typically cannot be directly excited by linearly polarized light at normal incidence due to their subradiant nature [84]. The excitation of dark modes has been demonstrated using a variety of tailored far-field illumination methods such as oblique incidence [85, 86], evanescent excitation [87], spatial phase shaping [88], and radially polarized light [89]. Dark modes have also been enabled by engineering photonic nanostructures with a broken geometrical symmetry, for example, by using non-concentric cavities [90]. In this case, induced symmetry breaking allows the interaction between a dipolar mode and a disk plasmonic mode, leading to a hybridized mode with the nature of both dark and bright. A large family of nanostructures that exhibit dark modes consists of finite clusters (oligomers) of isolated plasmonic nanoparticles [74]. While individual metal nanoparticles may support dark modes originating from high-

order multipole resonances, dark modes in clusters can arise from the interaction of bright modes in coupled nanoparticles. Dark plasmonic modes have also been observed in metamaterials that feature a dolmen-type structure and an asymmetric split-ring array [91, 92]. To further exploit dark plasmonic modes for various applications in optoelectronics, we have to make the dark modes directly accessible in the far-field as well as compatible with existing technologies for chip integration and electrical control.

In this work, we design and demonstrate a one-dimensional plasmonic diatomic grating that supports a novel plasmonic dark mode. Each duty cycle of the diatomic grating consists of two nonequivalent metallic strips, and the asymmetric design leads to the excitation of a dark plasmonic mode under normal incidence. The dark plasmonic mode in our structure, occurring at a prescribed wavelength of ~840 nm, features an ultra-narrow spectral linewidth of about 5 nm, which represents a small fraction of the value commonly seen in typical plasmonic resonances. Moreover, the metallic strips in the diatomic grating naturally serve as a pair of electrodes that facilitates optoelectronic light manipulation and signal generation. We leverage the dark plasmonic mode in the metallic nanostructure and demonstrate a resonance-enhanced plasmoelectric effect, in which the photon-induced electric potential generated in the grating follows the resonance behavior in the spectral domain.

2.2. Dark plasmonic modes in diatomic grating

As mentioned before, the dark mode in an optical system is a subradiant eigenstate that weakly couples to the far-field. By virtue of the symmetric mismatch present in each unit cell of a diatomic grating, the grating structure can induce dark modes through destructive interference of fields from distinct sub-cells. We design a

plasmonic diatomic grating with two nonequivalent metallic strips of alternating width, 135 nm and 275 nm, in each period, and a fixed width of 70 nm for the dielectric gaps, as shown in Figure 2.1a. The unequal widths of the two metallic strips provide a symmetric

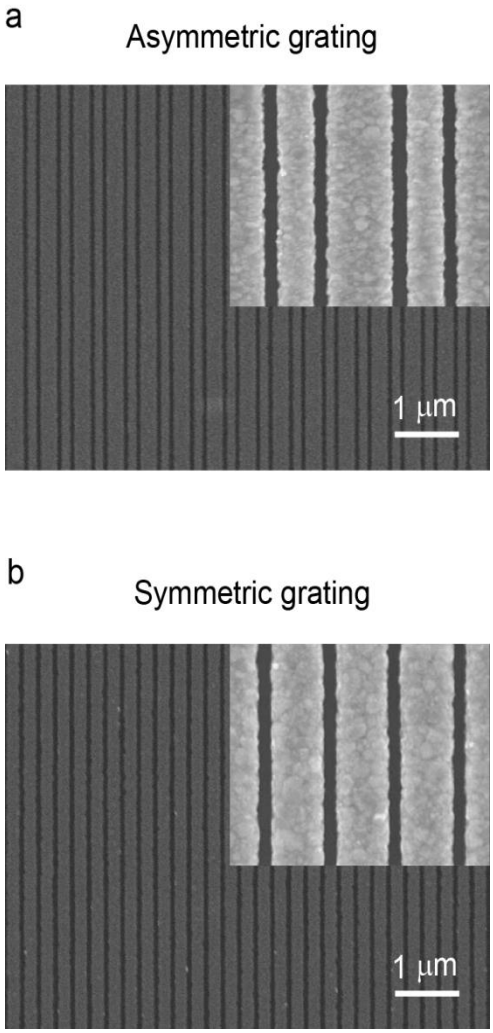

Figure 2.1. (a) SEM image of the diatomic (asymmetric) grating with each unit cell consisting of two nonequivalent metallic strips (135 nm and 275 nm, respectively). (b) SEM image of a symmetric grating with all strips having an identical width of 205 nm. For comparison, samples in (a) and (b) possess the same filling factor of the metal. Insets in (a) and (b) are close-ups of the gratings.

mismatch in each unit cell, leading to the existence of a dark mode in the diatomic grating. In this dark mode, the electric field profiles in the two sub-cells possess opposite polarities. With a π phase shift between them, the fields in the sub-cell pair destructively interfere, preventing the dark mode from radiating. The subradiant dark mode is associated with surface plasmons at the metal-dielectric interface when illuminated by a

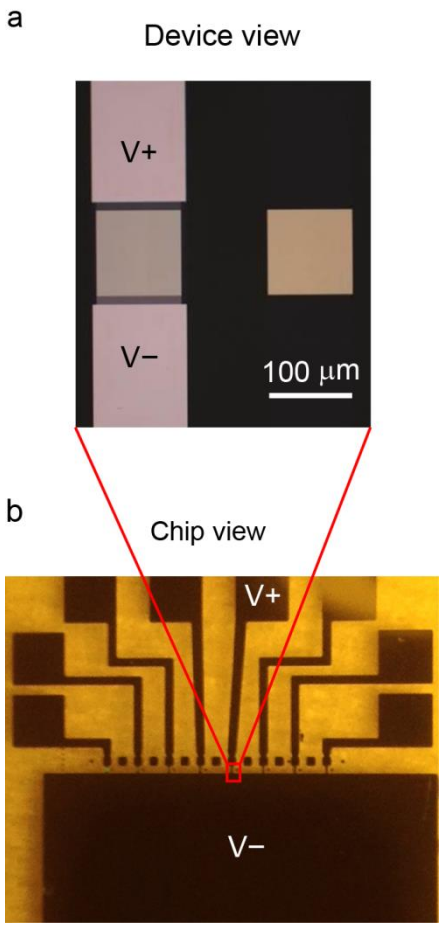

Figure 2.2. Dark-mode-enabled plasmonic devices with electrical connections. Part (a) shows the microscopic image of the diatomic grating, with each set of the metallic strips connected to a separate electrode. The electrode pair is connected to an external circuit for signal detection, as pictured in the optical image in (b).

linearly polarized wave with its electric field perpendicular to the grating strips. Moreover, each set of metallic strips in our structure is connected at one end to form a topologically continuous conducting film, in analogy to the interdigitated finger-like electrodes commonly used in photovoltaic cells. The connections of these alternating stripes provide an opportunity to simultaneously support optical and electrical functionalities in the structure in order to explore a variety of optoelectronic processes for electrically controlled light-matter interactions and conversion of optical information to electronic signals. Examples in this context include electric-field-induced second-harmonic generation, optical rectification, photoconductive response, the photon-drag effect, and more [20, 93-95]. To this extent, the diatomic grating, when connected to external circuits, may function as a self-contained plasmoelectronic platform that facilitates the generation and collection of electrical signals in response to incoming optical information, as will be demonstrated in the later part of this paper.

To prove the existence of a dark mode in our structure, we create two plasmonic gratings, one of an alternating width and one of a uniform width. In the asymmetric design, sub-cells of the diatomic grating distinguished by width are connected to a pair of electrodes marked with V+ and V−, as illustrated in Figure 2.2a and 2.2b. The control sample features a regular, symmetric grating with uniform strip width of 205 nm and identical gap size, 70 nm, in all unit cells, as depicted in Figure 2.1b. The asymmetric and symmetric samples thusly have the same overall filling fraction of the metal for comparison. The filling fraction (*ff*) is defined as $ff = 1-2w/p$, where w denotes the width of the dielectric gap between adjacent metallic strips, and p represents the periodicity of the grating. Under normally incident light, the geometrical symmetry in a regular grating

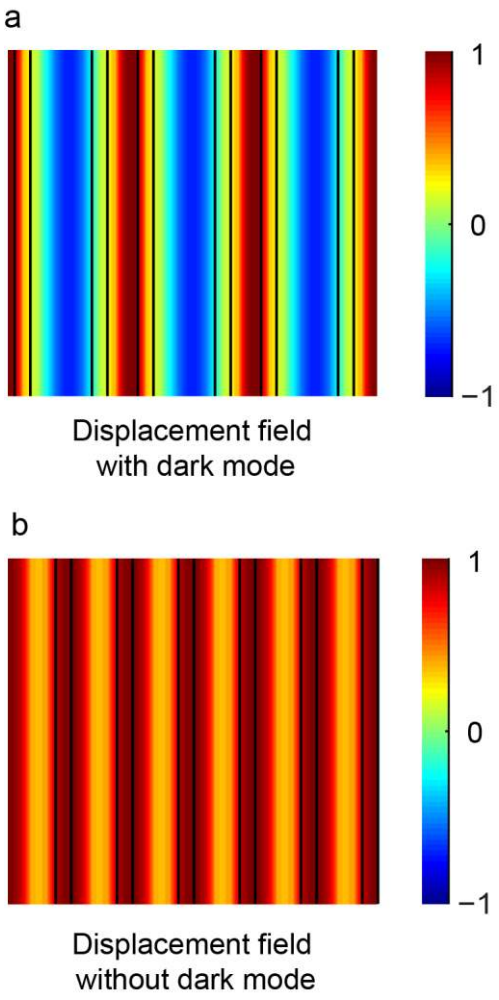

Figure 2.3. (a, b) Distribution of electric displacement field in the asymmetric and symmetric gratings, respectively, simulated at the wavelength of the dark mode resonance in the asymmetric structure. The diatomic grating features a dark plasmonic mode with a displacement field distribution of opposite polarities (blue and red) in the two sub-cells. In contrast, the symmetric grating exhibits identical distribution of the electric displacement in the adjacent sub-cells.

designates an identical field distribution in all cells. Because of the lack of discrepancy between sub-cells, electric fields in adjacent cells constructively interfere, and consequently the symmetric grating only affords a bright mode, which couples to the far-

field radiation. This is better visualized by comparing the distribution of electric displacement field in the two gratings, as illustrated in Figure 2.3a and 2.3b. In the asymmetric, diatomic grating that supports the dark plasmonic mode under normal incidence, the displacement field profiles in the two sub-cells shown in Figure 2.3a possess opposite polarities. This unique feature signals the direct excitation of dark modes in the diatomic grating. In contrast, the symmetric grating does not support the excitation of a dark mode under the same illumination condition. As a result, all strips of the symmetric grating embrace the same distribution of the displacement field and correspond to the tail of a bright mode, as illustrated in Figure 2.3b.

2.3. Dark plasmonic modes with exotic optical properties

A plasmon in a dark mode experiences a longer lifetime compared to its bright, radiative counterpart. As a result, the dark plasmonic mode has a higher quality factor (Q) featured with a narrower spectral linewidth. We first numerically simulate the transmission spectra of light through the diatomic and symmetric gratings under normal incidence in Figure 2.4. For TM polarization (red and blue), in which the electric field component of light is perpendicular to the grating strips, incoming photons are efficiently coupled into surface plasmonic resonances at the metal and dielectric interfaces when the momenta of the photon and the plasmon are matched. The geometrical asymmetry of the two sub-cells in each unit of the diatomic grating enables a dark plasmon, which has a characteristic feature of a sharp resonant peak, as seen in the transmission spectrum. The symmetric control pattern does not possess purposely induced geometric asymmetry, and therefore lacks a sharp feature in the transmission spectrum. When the incoming light is polarized parallel to the strips (TE), both gratings can be viewed as diluted metallic films with a limited amount of transmittance. As the asymmetric and symmetric gratings

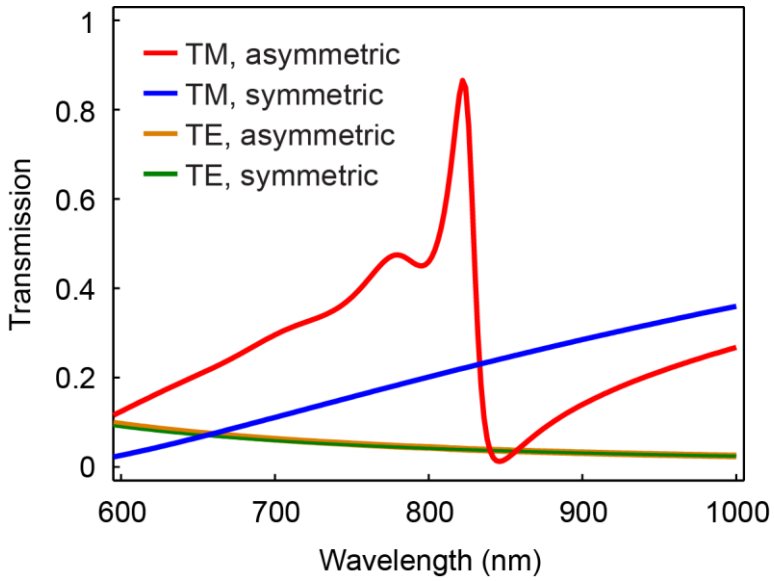

Figure 2.4. Simulated transmission spectra of both asymmetric and symmetric gratings under normal illumination. The TM (TE) polarization is defined for an impinging wave with its electrical field perpendicular (parallel) to the grating stripes.

share identical filling fractions of the metal, the same amount of TE-polarized light is transmitted through the two gratings, which is precisely illustrated in the brown and green curves in Figure 2.4. We note that the dark plasmonic mode cannot be attributed to Wood's anomaly, which has a resonant wavelength λ_R and can be written as $\lambda_R = n_s p$, where n_s is the refractive index of the substrate. This can be discerned by numerically simulating the transmission spectra of a symmetric grating with the same periodicity and substrate, where the sharp transmission peak either shifts or vanishes. In addition, the periodicity of the symmetric grating used for comparison is half of that of its asymmetric counterpart with the same filling factor. Comparison of the asymmetric grating that supports a dark plasmonic mode to a symmetric grating of the same periodicity is illustrated in Figure 2.15, which reveals that the symmetric grating only supports a bright plasmonic mode with a much broader spectral linewidth.

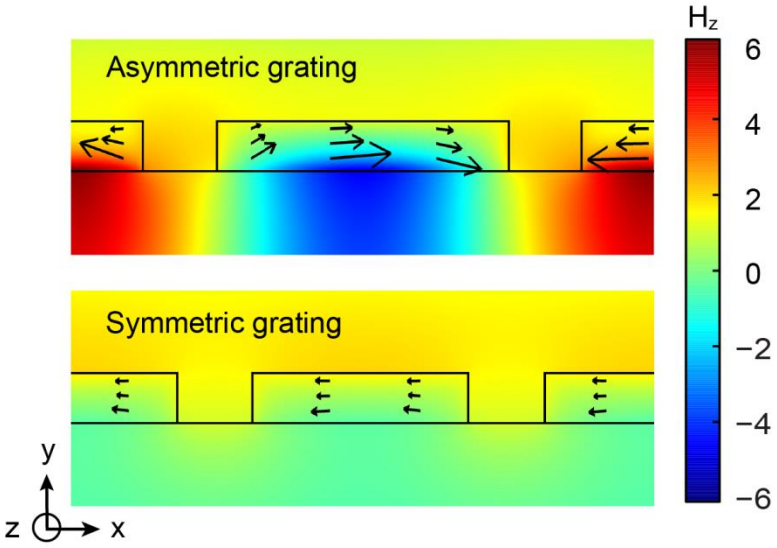

Figure 2.5. Field mapping in the gratings for the TM polarization at the wavelength of 830 nm. The magnetic field H_z, represented by the color mapping, is normalized to the magnetic field magnitude of the incoming light. The arrows represent the electric field distribution in the metallic strips. Similar to the displacement field distribution shown in Figure 1(d), the electric field exhibits out-of-phase behavior (phase contrast of π) in adjacent sub-cells, which indicates the existence of a dark plasmonic mode in the asymmetric, diatomic grating at the resonance of λ = 830 nm.

To further elucidate the origin of dark plasmonic modes, we simulate normalized field maps of the metallic gratings with TM polarized inputs at a wavelength of 830 nm in Figure 2.5. For the diatomic grating, a pronounced optical transmittance, visualized as the peak of the red curve in Figure 2.4, is enabled by the creation of the dark mode as shown in the distribution of the magnetic field component H_z in Figure 2.5, top. On the other hand, a low transmission is seen in the H_z mapping of the symmetric grating, as illustrated in Figure 2.5, bottom. This is because the symmetric grating allows only the direct excitation of a broadband bright mode, which is centered at a wavelength much shorter than the wavelength range of interest. The electric fields in

the plasmonic gratings, with both its vector amplitude normalized to that of the incident wave, are also plotted in Figure 2.5 with black arrows. In full consistency with the distribution of displacement field shown in Figure 2.3, both the electric and magnetic field distributions demonstrate the opposite parity of the fields in the two sub-cells of the diatomic grating. This near-π phase shift between the fields in adjacent sub-cells implies destructive interference between the fields, which leads to the generation of the dark, subradiant plasmonic mode.

The excitation of a surface plasmon can be treated as a process of momentum exchange between the input photons and the generated plasmons. The extra momentum required in this process can be introduced by using a grating. As a result, if the transverse component of the momentum of the incoming photon is varied, different surface plasmonic modes can be excited. We obtain the dispersion curves of the diatomic structure by computing the transmission of light

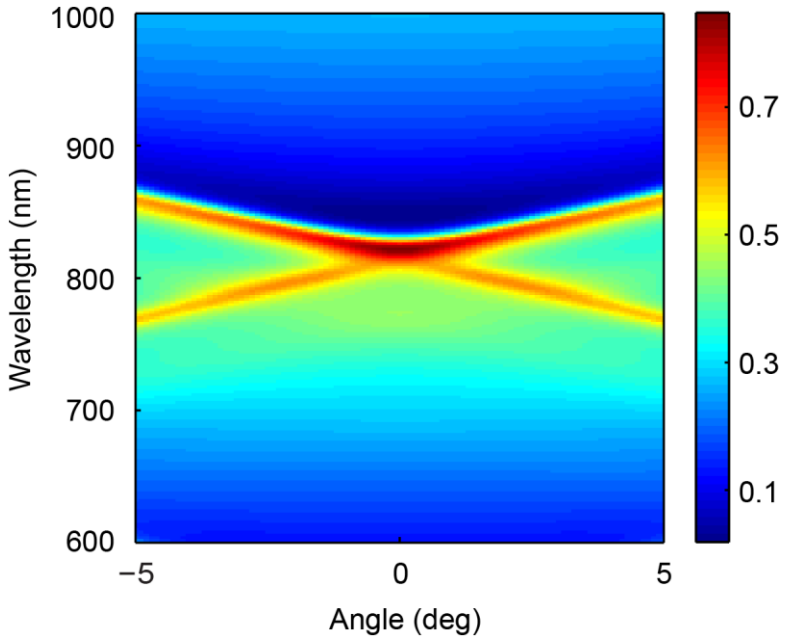

Figure 2.6. Transmission spectrum of the diatomic grating as a function of the incident angle of light, where 0° denotes the case of normal incidence. At oblique incidence, the dark plasmonic mode splits into two modes.

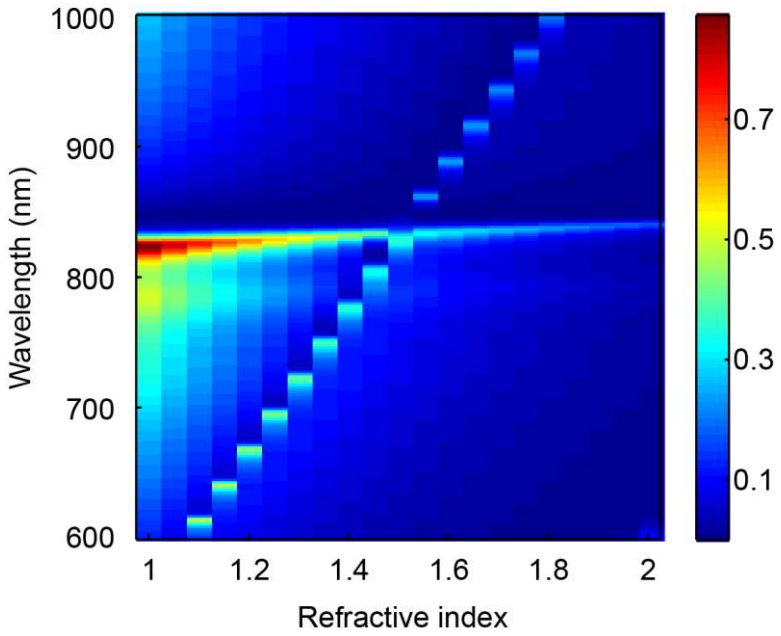

Figure 2.7. Optical transmission of the diatomic structure when covered with superstrates of various refractive indices. In terms of spectral location, the dark plasmonic mode is largely impervious to the change of the superstrate.

at varied incident angles in Figure 2.6. The dark plasmonic mode can be excited at normal incidence, which corresponds to a zero incident angle in the dispersion curve. More intriguingly, the mode shifts its resonant wavelength and splits into two modes at increased incident angles. The dark plasmonic modes in diatomic gratings arise from the geometrical asymmetry in the two nonequivalent sub-cells. The "darkness" of the dark mode, described in terms of linewidth and magnitude of the resonant peak, is mainly determined by the filling fraction *ff* and the difference parameter δ of two sub-cells. The difference parameter is defined as $\delta = |a_1 - a_2|/p$, where a_1 and a_2 are the width of the two sub-cells in each period. Simulated transmission spectra for diatomic gratings with various filling and difference factors are shown in Figure 2.16 of the supporting information. We further investigate the spectral behavior of the dark plasmonic mode with various refractive index of the cover material in Figure 2.7 and find that the spectral location of

the dark plasmonic mode is largely impervious to the change in the refractive indices of the surrounding material, as the resonant wavelength of this mode is essentially governed by the periodicity of the metallic grating.

2.4. Spectral characterization of dark plasmonic modes

We measured and analyzed the spectral responses of diatomic gratings that support geometrically induced dark plasmonic modes. Under TM illumination with the light polarized perpendicular to the grating strips, we excite surface plasmonic modes in metallic gratings under prescribed conditions. In particular, we observe a dark plasmonic mode evidenced by an ultra-

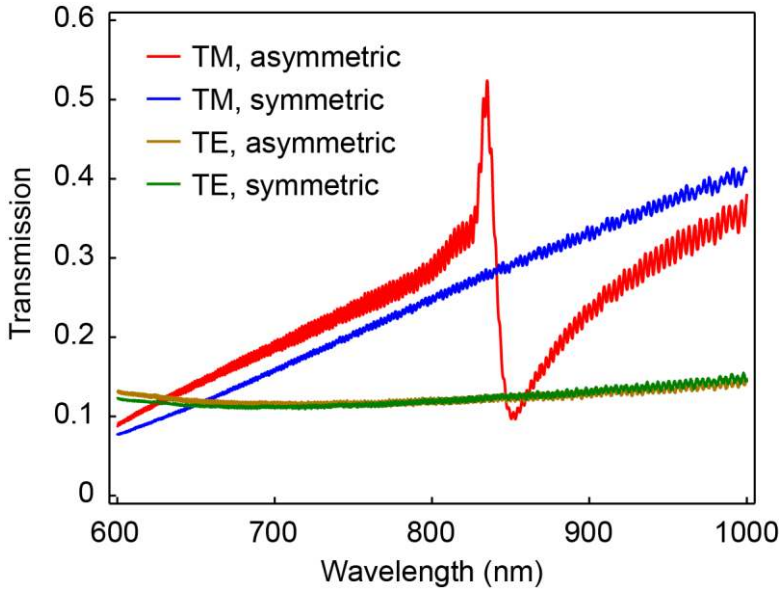

Figure 2.8. Measured transmission spectra of the asymmetric and symmetric gratings. A dark plasmonic mode is observed from the diatomic grating, as evidenced by the sharp transmission peak at a wavelength of ~835 nm under a TM polarized field. In contrast, the symmetric grating does not possess this spectral feature within the wavelength range shown. Under TE illumination, the asymmetric and symmetric gratings exhibit precisely the same transmission behavior.

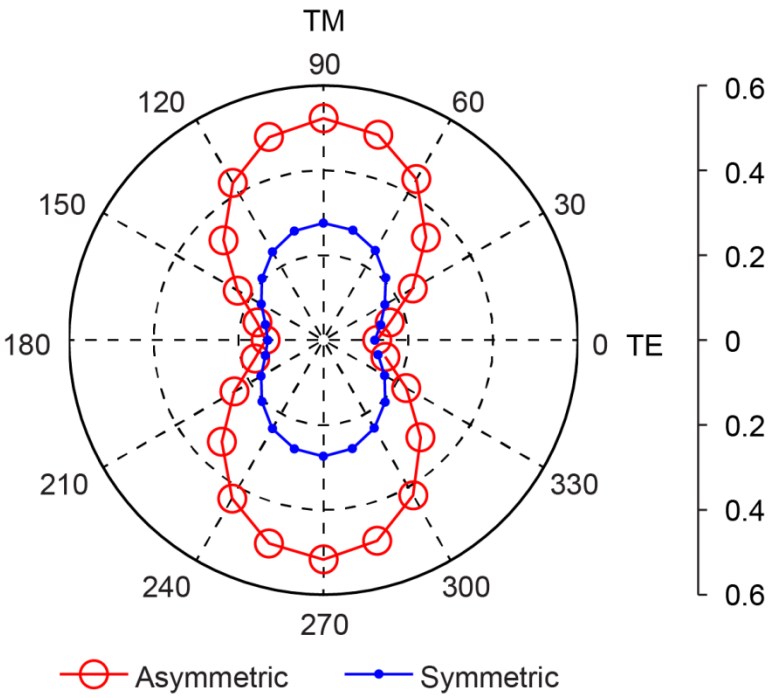

Figure 2.9. Optical transmission of the two gratings for a series of incident states of linear polarization. The data were collected at a wavelength of 835 nm. The 0° (90°) represents the input polarization parallel (perpendicular) to the grating strips, which corresponds to TE (TM) polarization of light.

sharp transmission peak with a spectral width of no more than 6 nm, when the diatomic grating is subjected to normal incidence of light at the wavelength of ~835 nm (Figure 2.8, red curve). This feature represents one of the sharpest resonance behaviors in any plasmonic systems and will be further discussed in the later part of the paper. As for the control sample with identical metallic strips, no geometrical asymmetry is introduced, and therefore the system is unable to support a dark mode, as indicated by the featureless spectrum in the wavelength range of interest. The overall transmission properties of the two gratings agree remarkably well with the numerical simulations in Figure 2.4. For TE illumination with the light polarized along the strips, the lack of geometrical confinement along the direction of the electric field component of the wave makes

the gratings a diluted metal that reflects back most of the light. Moreover, since the two gratings possess the same filling fraction of the metal, the measured transmission spectra are precisely identical for both the diatomic and symmetric gratings, as shown in Figure 2.8.

We also measure the light transmission at the characteristic wavelength of 835 nm for both gratings as a function of input polarization in Figure 2.9. As expected, the spectral responses in the gratings are polarization sensitive, as light can be effectively coupled to surface plasmons only when it is polarized perpendicularly to the metallic nanostrips. This is illustrated in Figure 2.9, where a much higher transmission is observed in the asymmetric grating than that of the symmetric grating at the input polarization of 90° (270°). Here, the polarization of 90° represents the TM case discussed before, which is necessary for the excitation of dark plasmonic modes in diatomic gratings. To further explore the geometrically induced dark plasmonic modes in diatomic gratings, we obtain the transmission spectra under TM illumination for gratings with varying geometrical parameters. The change of the filling fraction (*ff*) is realized by changing the gap width (w) while keeping the difference parameter (δ) and the periodicity (p) unaltered. We fabricated and tested a series of diatomic gratings whose gap width (w) ranges from 65 nm to 80 nm with a step size of 5 nm and the transmission spectra of these samples are illustrated in Figure 2.10a. In diatomic gratings, a narrower gap leads to a stronger interaction between the fields in the two sub-cells, and hence more pronounced features of the dark plasmonic mode. We observe, in Figure 2.10a an ultra-sharp transmission peak in the diatomic sample with a gap width of 65 nm, however, the same feature becomes barely visible when the gap width is increased to 80 nm. As for the symmetric gratings that do not support dark plasmonic modes, a narrower gap naturally makes the metallic structure more optically opaque, which results in a lower transmission shown in Figure 2.10b.

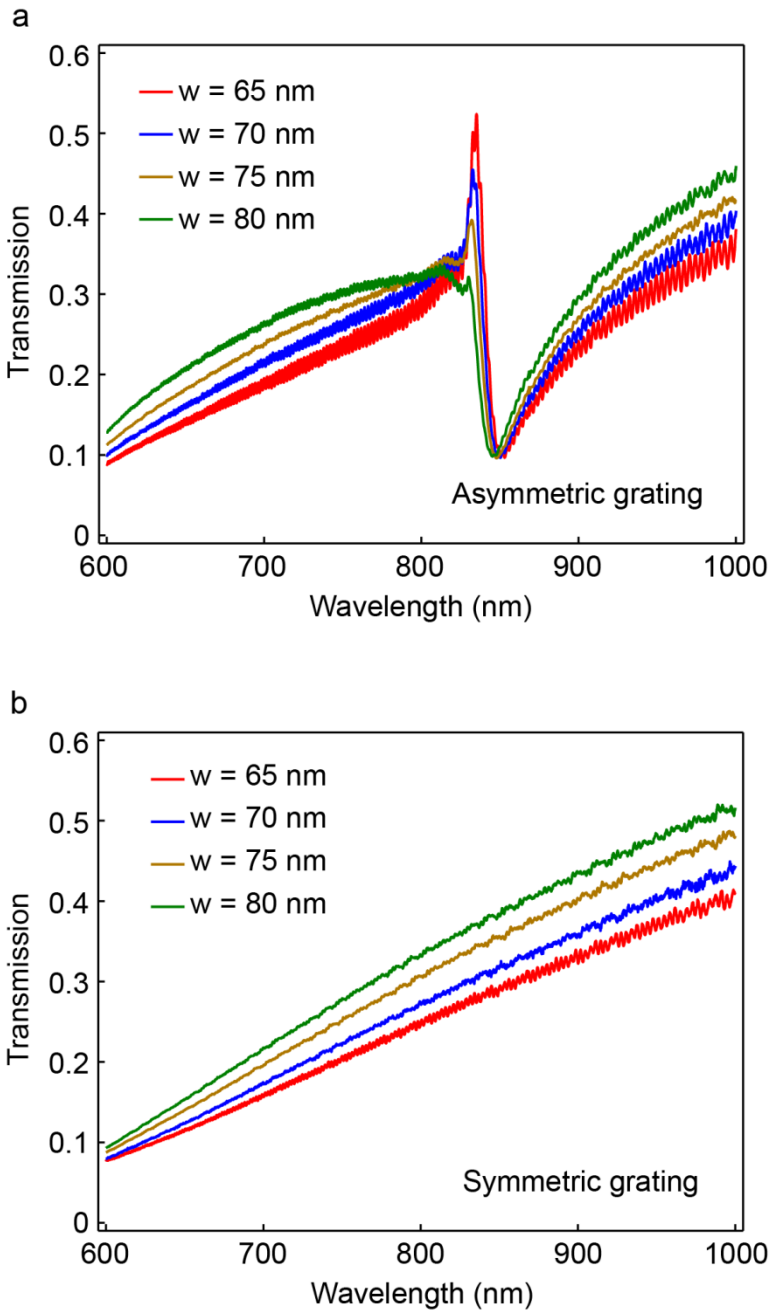

Figure 2.10. Transmission spectra of the two gratings under the TM polarization for a series of the gap size (*w*). For the diatomic grating, a narrower gap indicates stronger field coupling between adjacent sub-cells, which leads to a sharper spectral feature at the resonance.

2.5. Optoelectronics with dark plasmonic modes

As discussed in the earlier part of the paper, nanostructured metals simultaneously support electrical and optical functions in a unified platform, thereby facilitating a wide range of optoelectronic processes. Such processes include voltage-controlled light-matter interactions and photon-induced electric signal collection. As an example in this context, here we demonstrate optically induced generation of voltage signals in diatomic gratings. The schematic of the device is depicted in Figure 2.11, where the two metallic strips, distinguished by width, in each unit cell are connected to form a pair of electrodes. Under laser illumination, the plasmoelectric potential in the structure leads to a voltage drop across the gap, whose magnitude and spectral response are critically related to the dark plasmonic resonance in the diatomic structure.

In the experiment, the electrode formed by all wider strips is grounded, and the induced electric potential at the connected narrower strips is monitored under various testing conditions. We first measured the generated voltage signal when optically exciting the asymmetric grating at a series of wavelengths. During the measurement, the intensity of the incoming beam is kept at a

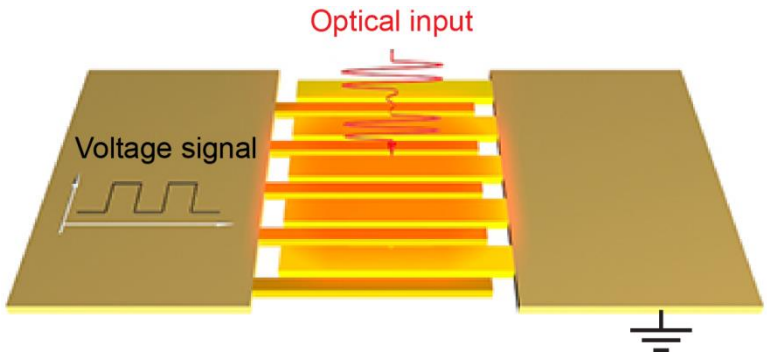

Figure 2.11. Device schematic for the detection of light-induced voltage signals. The two sets of the sub-cells in the diatomic grating are connected to a pair of electrodes. When light impinges on the diatomic grating, an induced potential difference can be measured across the electrode pair.

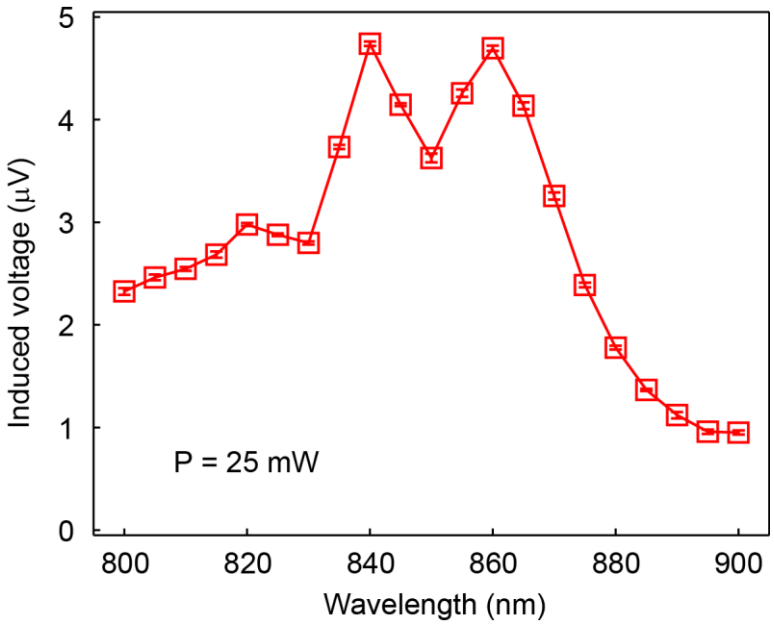

Figure 2.12. Measured voltage signals emerge from the sample when pumped at a series of excitation wavelengths. The diatomic grating is excited with an incident polarization perpendicular to the metallic strips. The power of the incident light is kept at a constant level of 25 mW for all incident wavelengths.

constant level (25 mW optical power for a beam diameter of ~50 μm), and the polarization of light is perpendicular to the strips to facilitate the excitation of the plasmonic modes. As expected, the measured voltage signal reaches its peak value at the wavelength of ~840 nm in Figure 2.12, thanks to the enhanced light-matter interaction enabled by the high-Q dark plasmonic mode. Plasmon-induced voltage generation closely correlates to the previously observed optical resonance behavior, not only in the overall spectral features but also the polarization behavior. As shown in Figure 2.13, when altering the angle of the linearly polarized incidence, the voltage signal increases as the input polarization rotates from 0° (TE) to 90° (TM) and reaches its maximum value at the TM polarization where the dark plasmonic mode is most efficiently excited. The aspect ratio, defined as I_{TM}/I_{TE} where I_{TM} (I_{TE}), represents the signal intensity for TM

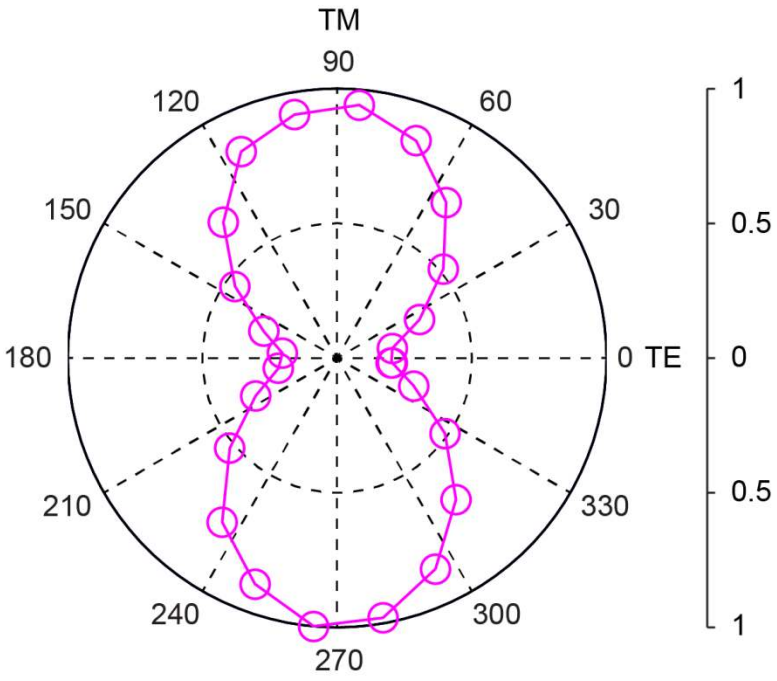

Figure 2.13. Dependence of the induced electrical signal on the polarization of the incident light at the resonance wavelength of the dark plasmonic mode, λ = 840 nm. The 0° (90°) angle represents the TE (TM) polarization of the illumination as defined before.

(TE) polarized input, exhibits a value of ~4.5 for both the optical transmission (Figure 2.9, red) and the induced voltage signal in Figure 2.13. This is because the strength of the plasmon-induced voltage generation is linearly proportional to the optical intensity, as confirmed in the dependence of the generated voltage as a function of the input light power shown in Figure 2.14.

While plasmonics has offered a unique opportunity to manipulate light at the deep-subwavelength scale, the spectral sharpness and quality factor of plasmonic resonances are substantially worse than what a dielectric resonator could offer. In general, plasmonic resonances including those featuring a Fano resonance or electromagnetically induced transparency [82, 83] typically exhibit a spectral linewidth of ~50 nm [56, 72-79], limited largely by the combined

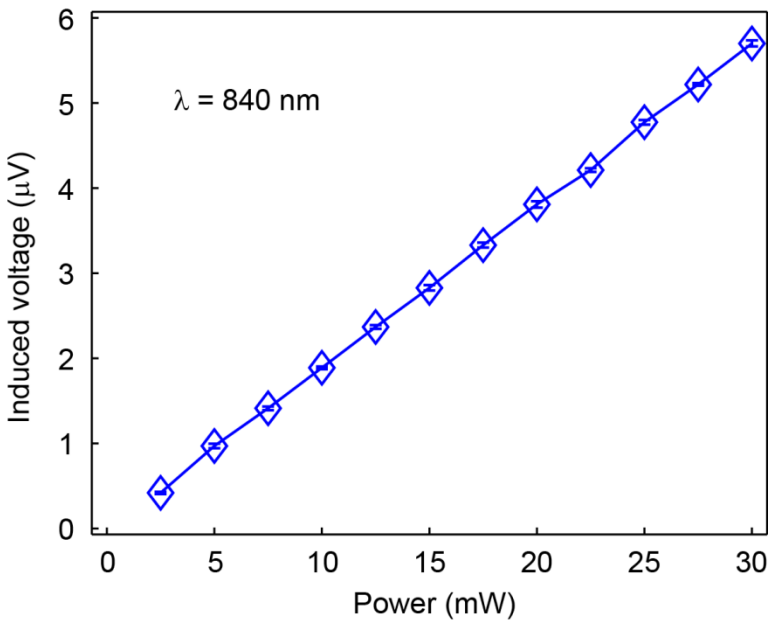

Figure 2.14. The induced voltage signal as a function of the light power at the excitation wavelength of 840 nm. The beam size is fixed at ~50 μm for all measurements. Error bars represents the standard deviation from five consecutive measurements. All solid lines are to guide the eye.

damping and radiative loss in nanometallic structures. The dark plasmonic modes presented in this work by the diatomic gratings feature an ultra-sharp transmission peak with a linewidth that has a full width at half maximum of ~5 nm as shown in Figure 2.8 and 2.10, one order of magnitude narrower than those seen in most plasmonic systems. In diatomic plasmonic gratings, the spectral linewidth of the dark mode is primarily determined by the geometrical difference factor (δ), which can be understood within the framework of light interference. Since the geometrically induced dark plasmonic modes result from the destructive interference between the fields in adjacent strips, a smaller contrast in the strip width progressively makes the phase difference of fields in neighboring strips closer to π leading to a better destructive interference and hence a darker plasmonic mode. As the radiative loss is effectively suppressed, the spectral

linewidth of the dark plasmonic mode is limited only by the dissipative losses in the metal. Another intriguing feature of our fabrication-friendly design lies in the fact that the spectral feature is governed by the in-plane geometry of the planar structure, which essentially relaxes the fabrication tolerances and the demand for surface flatness commonly seen in high-Q plasmonic resonators.

We also observed the generation of electrical signals in the plasmonic diatomic grating by connecting the two sets of nanostrips to a pair of electrodes. We attribute the voltage signals induced by the dark plasmonic mode to a plasmoelectric potential effect, where the generation of electric potential stems from the change of carrier density in metallic nanostructures under coherent illumination [96]. The thermodynamic behaviors of the free carriers in the two sets of strips are not precisely identical because of their distinct absorption resonances, which in turn yields different potentials and hence a voltage drop across the gap. The optically induced generation of plasmoelectronic potential is closely correlated to the linear resonance behavior, in terms of not only the overall spectral feature but also the polarization dependence as illustrated in Figure 4. Rigorously speaking, the magnitude of the generated plasmoelectronic potential is governed by the stored electromagnetic energy instead of the light absorption in the metal. The exact spectral behavior of the electromagnetic energy for both symmetric and asymmetric gratings is numerically simulated in Figure 2.17 of the supporting information. When the diatomic grating is coated with a polymer, the spectrum of the stored energy in the grating exhibits a double-peak characteristic, which is, in turn, translated to the spectral behavior of the induced voltage signal shown in Figure 2.12. For further interpretation of the observed voltage signals, we discuss and rule out the possibilities of other mechanisms that generate voltage signals with metals, such as the pyroelectric, the plasmon drag, and the thermoelectric effect. The

pyroelectric effect produces a voltage signal that gradually disappears over time [97], while the observed electric signal in our structure remains stable when the input light is kept constant. We also rule out the plasmon drag effect, given the absence of the direct photon-to-electron momentum transfer under normal incidence [95]. Furthermore, we exclude the thermoelectric effect because of the absence of temperature gradients in each metal stripe under uniform illumination [98]. A consistent microscopic theory of the plasmoelectronic effect in asymmetric periodic nanostructures would be beneficial for future works in this area.

2.6. Summary

In conclusion, we have demonstrated a diatomic grating that supports a dark plasmonic mode with an ultra-sharp spectral feature (~5 nm) and a high Q factor (~170) not commonly seen in nanometallic systems. Our results show that the radiative loss of the dark plasmonic modes can be efficiently suppressed by introducing an asymmetry within each unit cell of the diatomic grating. The two sets of metallic strips naturally serve as a pair of electrodes, facilitating optoelectronic functionalities for optically induced signal generation and electrically controlled photonic processes. We observed a resonance enhanced the plasmoelectric effect that closely correlates to the spectral and polarization behavior in the diatomic grating. The open cavity with a planar design offered a potential for easy integration with other nanophotonic materials and systems. Furthermore, thanks to the light concentrating ability combined with an ultra-sharp resonance feature at a relatively low loss, the dark plasmonic modes may offer exciting opportunities for diverse applications ranging from optical filtering to emission control and plasmonic lasing where enhanced light-matter interactions are needed.

2.7. Methods

2.7.1. Numerical simulation

A commercial finite-element solver (COMSOL) was used to model the optical responses of the plasmonic device. Perfectly matched layers were applied around the simulation domain. All geometrical parameters in the final structure are optimized for a pronounced resonance feature at a prescribed wavelength range. The silver gratings with a thickness of 50-nm were situated on top of a glass substrate, where the refractive index of the substrate was fixed at 1.5 for all wavelengths.

2.7.2. Device fabrication

The plasmonic devices were fabricated using standard microfabrication processes involving photolithography and electron beam (e-beam) lithography. First, a polymethyl methacrylate (PMMA) thin film was spin-coated on a microscope slide and patterned via e-beam lithography (JEOL JBX-9300FS EBL). Afterwards, a 50-nm thick silver film was deposited on top of the PMMA layer using e-beam evaporation (CVC evaporator). The patterns were transferred to the silver film after a lift-off process. The two electrodes were formed using e-beam evaporation (CVC evaporator) together with a photolithography process.

2.7.3. Characterization

A fiber coupled broadband light source (B&W Tek BPS120) was collimated and used for the characterization of the transmission spectrum. A linear polarizer was used to create polarized light at normal incidence. The light transmitted through the sample were collected by an objective (Mitutoyo, 20× Plan Apo NIR infinity-corrected) and transformed into a magnified

image of the sample on the conjugate plane, where light from the desired area was picked up by an iris and sent to a spectroscopy system for detection (Princeton Instruments, Acton SP 2300i and PIXIS 400). The transmission spectrum of the sample was normalized to that of the glass substrate. To test the electrical responses of the plasmonic devices, a tunable pulsed laser (Spectra-Physics Mai Tai HP) was introduced to the system, where light beams of controlled power and polarization state were used to excite the sample. Electrical signals were measured using a lock-in amplifier with the detected signal frequency-locked to an optical chopper.

2.8. Supporting information

2.8.1. Periodicity of Symmetric and Asymmetric Gratings

The resonance wavelength for the periodic structures is largely determined by the periodicity. For symmetric gratings, the periodicity is half of p, as defined in the manuscript, because two unit cells are contained in each period of p. For asymmetric gratings, because of the discrepancy in width of the adjacent metal strips, the periodicity is the same as p. Thus, the periodicity of the asymmetric grating at p = 550 nm is the same as that of the symmetric grating at p = 1100 nm. As a result, the resonant wavelengths for both gratings are in the wavelength range of interest as shown in Figure 2.15. As expected, the symmetric grating that does not support a dark mode has a broad resonance as shown in Figure 2.15, red. In addition, the asymmetric grating supports a dark mode featured with an ultra-sharp transmission peak as shown in Figure 2.15, blue.

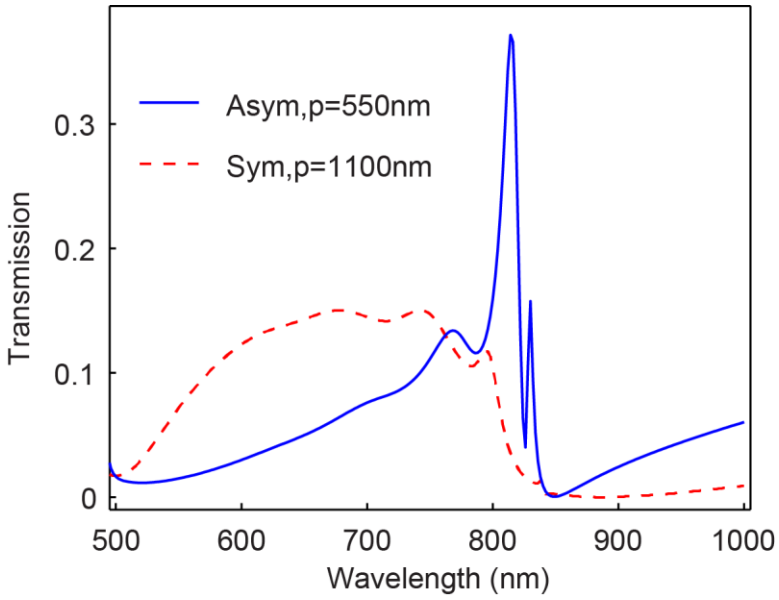

Figure 2.15. Simulated transmission spectra for asymmetric and symmetric gratings with the same overall periodicity and filling factor. For the asymmetric grating (blue), the periodicity has the same value as p defined in the manuscript. For the symmetric grating (red), the periodicity is half of p, where p is 1100 nm. For both gratings, the periodicity is 550 nm and the filling factor is 0.75.

2.8.2. Difference and Filling Factors

To study the evolution of dark plasmonic modes in diatomic gratings, we numerically simulate transmission spectra for various filling and difference factors. Figure 2.16 shows transmission spectra with the difference factor δ, defined as $\delta = |a_1 - a_2|/p$, varied from 0 to 0.6 by fixing the filling factor *ff* and the periodicity p at constant values of 0.75 and 550 nm, respectively. With fixed periodicity and varied difference factor, the resonant wavelength of the dark plasmonic mode shifts ~20 nm. This shift does not follow Wood's anomaly, which states that a resonant wavelength should remain constant when periodicity and substrate are left unchanged, so we can eliminate the Wood's anomaly as the cause of the

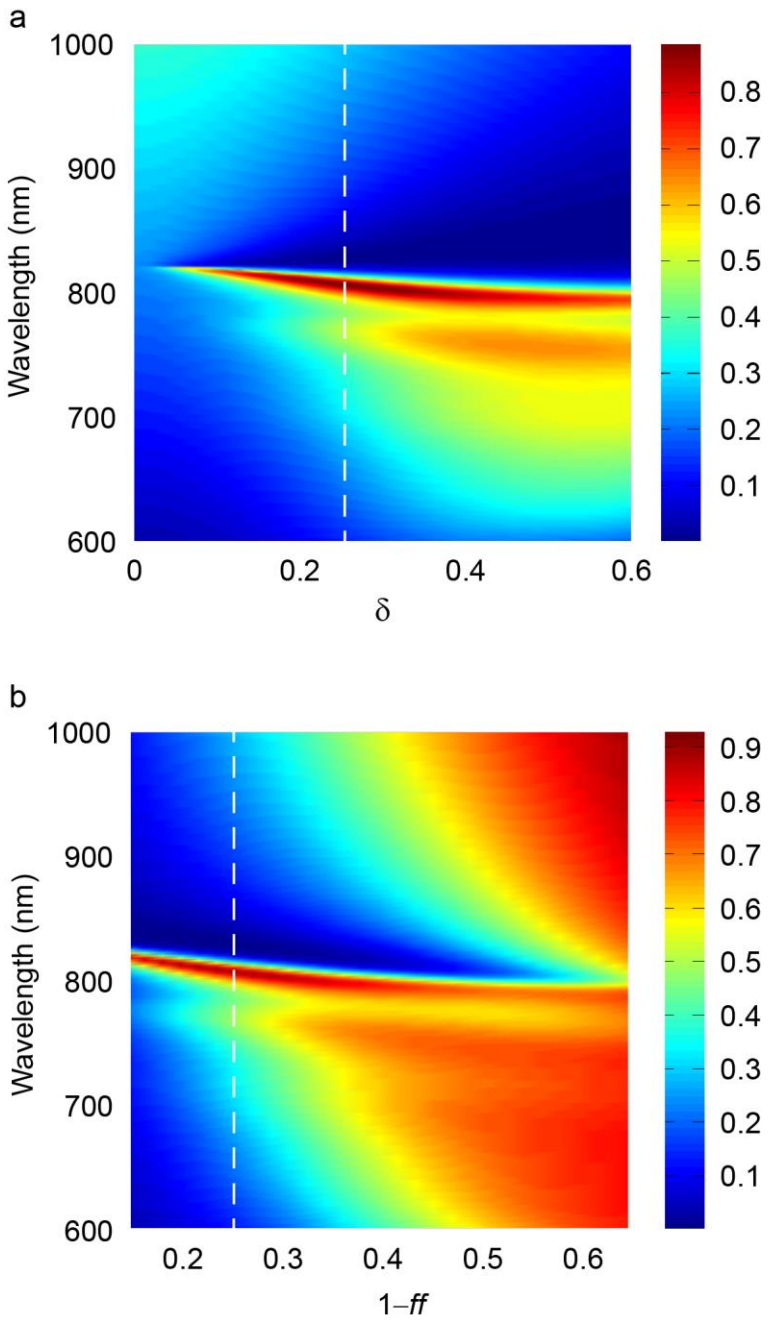

Figure 2.16. Simulated transmission spectra for asymmetric and symmetric gratings with the same overall periodicity and filling factor. For the asymmetric grating (blue), the periodicity has the same value as p defined in the manuscript. For the symmetric grating (red), the periodicity is half of p, where p is 1100 nm. For both gratings, the periodicity is 550 nm and the filling factor is 0.75.

observed dark modes. Moreover, the difference factor δ also controls the spectral linewidth of the dark plasmonic modes. By reducing the value of δ, the linewidth that depicts the loss of the dark mode further decreases. For example, the linewidth of the dark plasmonic mode at $\delta = 0.01$ is ~1 nm, which demonstrates the sharpest plasmonic resonance, to the best of our knowledge, in all plasmonic systems [86, 99]. Figure 2.16b shows transmission spectra for diatomic gratings with a set of filling factors. The linewidth of the dark mode decreases as the filling factor *ff* increases.

2.8.3. Electromagnetic Energy and Induced Voltage

To further elucidate the physical mechanism of the induced voltage signal, we numerically extract the electromagnetic energy of plasmonic modes in the metal strips of plasmonic gratings. For the asymmetric (diatomic) grating that supports a dark mode, the electromagnetic energy in the metal strips at various wavelengths features with two resonant peaks, as shown in Figure 2.17 (blue). This two peak feature is also shown in the spectral behavior of the induced voltage signal (red). For the symmetric grating, the electromagnetic energy in the metal strips is much lower than that in the diatomic grating with the same filling factor. For both gratings, the refractive index of the cover layer (PMMA) and the glass substrate are fixed at 1.5 in the simulation, and the electromagnetic energy is normalized to that of the input light.

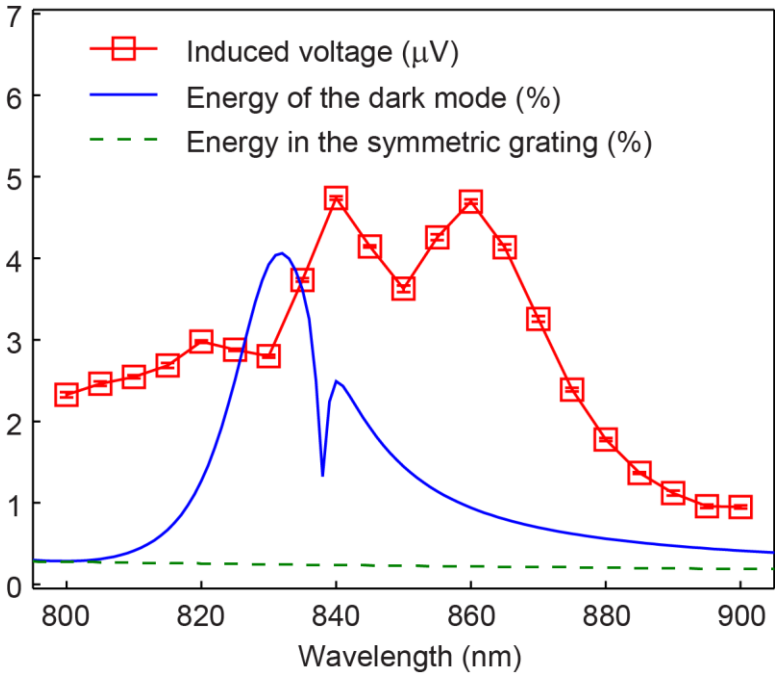

Figure 2.17. The electromagnetic energy of plasmonic modes in metallic gratings. The spectral behavior of the voltage signal (red) follows that of the electromagnetic energy of the dark mode (blue) in the diatomic grating. The electromagnetic energy in the symmetric grating (green) remains low.

CHAPTER 3

ELECTRIFYING PHOTONIC METAMATERIALS FOR TUNABLE NONLINEAR OPTICS

3.1. Overview

Optical metamaterials afford exotic light manipulation through artificial structuring and arranging of nanosized metal-dielectric subunits [45, 56, 67, 100, 101]. As the study of metamaterials evolves beyond the conventional, linear regime, an ever-growing emphasis is being placed upon functionalizing these novel optical media into meta-devices for signal processing, light switching, and sensing applications [71, 102-104]. While the linear responses of optical metamaterials have been extensively studied, the nonlinear phenomena in metamaterials, which usually form the basis for the dynamic response and active control of these novel media [40, 50, 55, 105, 106], are comparably underdeveloped. The capability to design custom nonlinear materials, which is made possible through metamaterials, is bound to open entirely new vistas for nonlinear light-matter interactions.

In optical metamaterials, nanostructured metals are cherished because of their unique plasmonic responses. Often neglected in this context is that metals are electrically and thermally conductive, therefore enabling a range of secondary functions including voltage offset, carrier injection, and heat sinking. Consequently, optical metamaterials can be viewed as a self-contained electrooptic system with intrinsically embedded electrical functions. Taking full advantage of the dual-functionality supported by the same nanostructure, we apply a voltage bias to tune the second-order nonlinear effects in

an optical metamaterial. The nonlinear processes being investigated herein include second-harmonic generation (SHG, $\omega + \omega \rightarrow 2\omega$), where two photons at the fundamental frequency ω are combined to create a frequency-doubled photon at 2ω, and optical rectification (OR, $\omega - \omega \rightarrow 0$), which can be viewed as a special case of difference frequency generation that induces a quasi-DC polarization in the nonlinear medium. In sharp contrast to conventional SHG and OR processes, which rely on the second-order nonlinear susceptibility, in this work we explore the electric-field-induced second-harmonic (EFISH) generation and optical rectification (EFIOR), which are third-order nonlinear effects enabled by an externally applied static or low frequency field ($\omega + \omega + 0 \rightarrow 2\omega$ for EFISH, and $\omega - \omega + 0 \rightarrow 0$ for EFIOR). As a result, these two electrically-induced nonlinear phenomena are not limited to noncentrosymmetric materials with a non-zero $\chi^{(2)}$. Instead, the generation of EFISH and EFIOR signals is possible in all materials, including amorphous dielectric layers in optical metamaterials, because of the ubiquity of the third-order nonlinear susceptibility $\chi^{(3)}$.

The EFISH effect was discovered in 1962, just one year after the first demonstration of second harmonic generation [1, 19] and has been utilized in electrooptic applications such as the characterization of organic nonlinear materials and the ultrafast detection of electrical signals in semiconductors. Very recently, EFISH was brought to nanophotonic systems for the first time and was generated inside a polymer-filled plasmonic nanoslit [20]. While both SHG and OR were discovered during the early days of nonlinear optics in the 1960s [21], optical rectification received very limited attention for decades until being revived as a major scheme for generating terahertz radiation [25, 26, 107]. The electric-field-induced optical rectification was first demonstrated in 1977

where kilovolts of potential difference (corresponding to an electric field magnitude of ~1V μm^{-1}) were applied across a centrosymmetric nonlinear medium sandwiched between two electrodes [22]. Similar to EFISH generation, an effective second-order response is produced by the interplay between the third-order nonlinear susceptibility and the applied control field ($\chi^{(3)}E_c \rightarrow \chi^{(2)}_{eff}$) to generate EFIOR. In this work, we leverage the resonance-enhanced light concentration in a metamaterial absorber and the electrical functions supported in the same nanostructured metals to experimentally demonstrate voltage-controlled nonlinear processes from an optical metamaterial. The second-harmonic and optical rectification signals from the device, enhanced by the resonance behavior in the metamaterial, is modulated by applied voltage signals in a linear fashion. This work represents an entirely new category of active metamaterials where nonlinear optical interactions can be purposely controlled by electrical signals.

3.2. A metamaterial absorber for electrically-controlled nonlinear effect

In this work, a dual layered nanometallic absorber is employed to demonstrate voltage-controlled nonlinear optical processes. This type of metamaterial-based perfect absorber can be designed to capture all the energy of the incident light within a prescribed frequency range [108-111]. The schematic of the meta-device for EFISH and EFIOR is illustrated in Figure 3.1. The metamaterial absorber consists of a periodic hole-array in a gold film, separated from a planar silver film by an alumina based dielectric spacer. Each metallic layer is wired to an external circuit for voltage biasing (see Methods). Such device architecture immediately offers several features that are beneficial to the generation of EFISH and EFIOR signals. First, the nanometallic films forming the

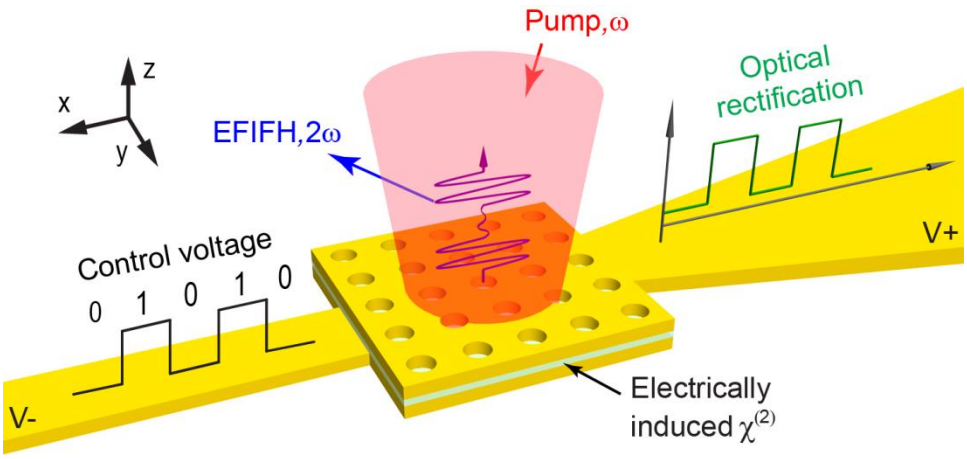

Figure 3.1. Schematic of the metamaterial device consisting of a 50 nm thick perforated gold film, separated from an unpatterned silver layer by a 100 nm thick alumina (Al_2O_3) spacer. Diameter and square lattice periodicity of the hole-array are 186 nm and 370 nm, respectively. With connections to external circuit, the metallic layers also serve as electrodes for the voltage control.

metamaterial naturally serve as electrodes for electrical input. Second, the thin dielectric gap of ~100 nm enables the generation of a giant static field within the insulating layer with modest, chip-level voltage signals. Finally, optical energy within the operational band is effectively trapped within the metamaterial absorber, thus enhancing the light concentration inside the cavity-like spacer by a factor of ~50. Like all nonlinear frequency-mixing processes, the efficiencies of the EFISH and EFIOR effects are positively correlated to the local intensity within the nonlinear medium, in our case, the dielectric gap.

The alumina dielectric spacer and its metallic interfaces within the metamaterial perfect absorber provide the necessary characteristics to demonstrate the EFISH and EFIOR generation. Due to the limited magnitude of $\chi^{(3)}$ in most materials, the realization of the EFISH or EFIOR generation typically requires a high intensitty light source and/or

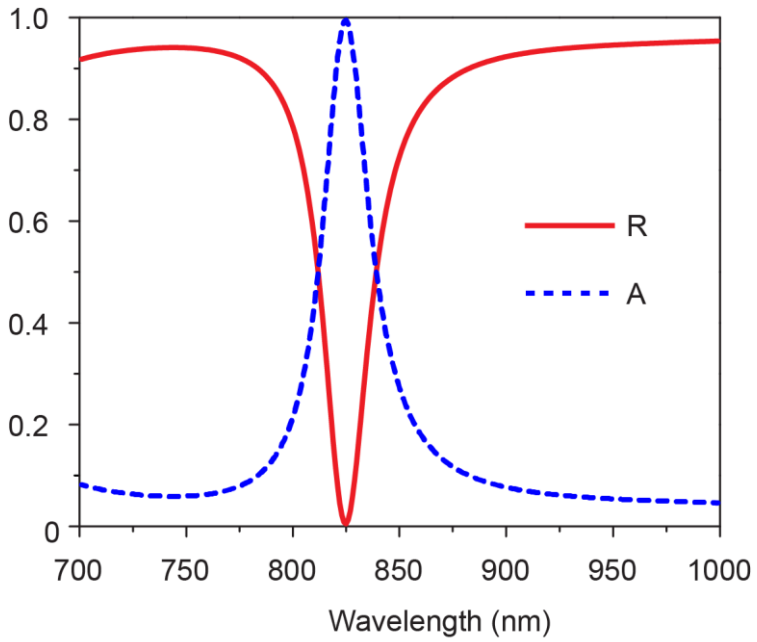

Figure 3.2. Simulated reflection (R) and absorption (A) spectra indicate the perfect absorption response around the wavelength of 820 nm, where $A(\omega) = 1 - R(\omega) - T(\omega)$ and the transmission $T(\omega) = 0$ due to the optically thick silver layer.

a gigantic control voltage across a bulk nonlinear medium with macroscopic dimensions. These stringent requirements are substantially mitigated in the metamaterial-based platform, thanks to the deeply-subwavelength thickness of the dielectric spacer and the light concentrating ability of the metamaterial absorber. More importantly, within the absorption range of around 820 nm (Figure 3.2), the electric field component of the incident light is enhanced by nearly one order of magnitude, predominately perpendicular to the metal-dielectric layers and collinear with the control field. Consequently, the applied control field $E_{c,z}$ couples with the strongest elements in the third-order nonlinear

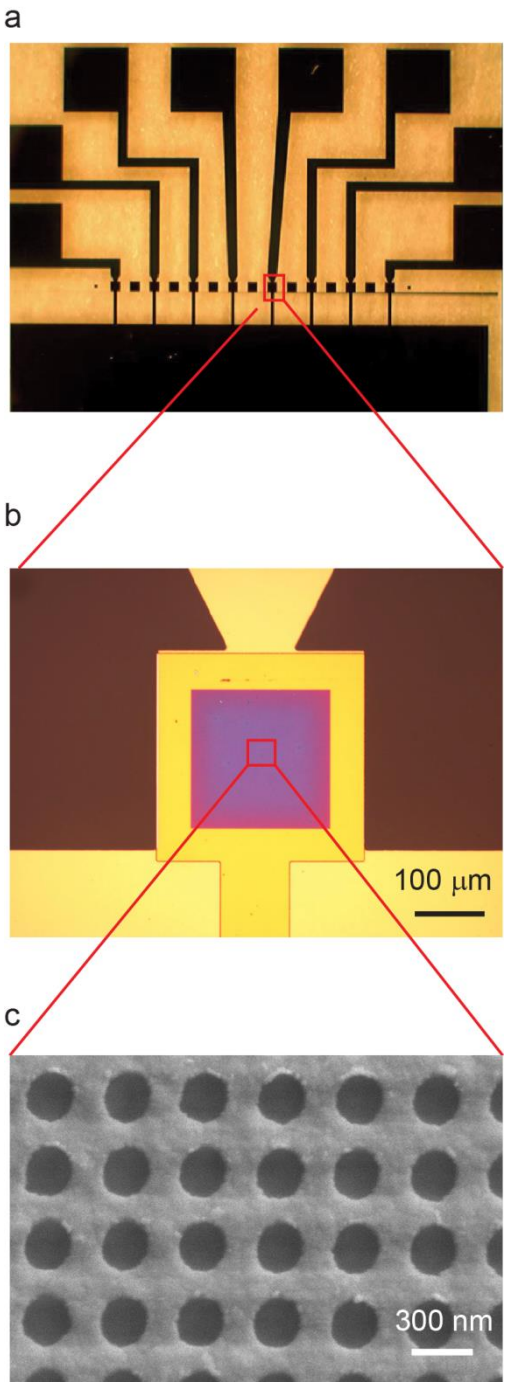

Figure 3.3. Microscopic images of the entire chip with multiple EFISH devices and a close view of an individual device with electrical contacts. The scale bar represents 100 μm. (c) Scanning electron microscopy image of the patterned top film of the metamaterial absorber. The scale bar represents 300 nm.

tensor, $\chi^{(3)}_{ZZZZ}$, to create an effective second-order susceptibility $\chi^{(2)}_{eff,ZZZ} = \chi^{(3)}_{ZZZZ} E_{C,Z}$ in the spacer, which works together with an enhanced optical field $E_z(\omega)$ to produce the nonlinear dipole sources for the EFISH and EFIOR fields.

3.3. Linear and nonlinear spectral characteristics

In this experiment, the electrically-active metamaterial device is wired to an external circuit via on-chip connections, as illustrated in Figure 3.3. We first performed a comprehensive measurement of the nonlinear optical signals from the meta-device when excited with a tunable ultrafast laser, without an applied control voltage. Although the alumina spacer and metals used in the metamaterial are amorphous with inversion

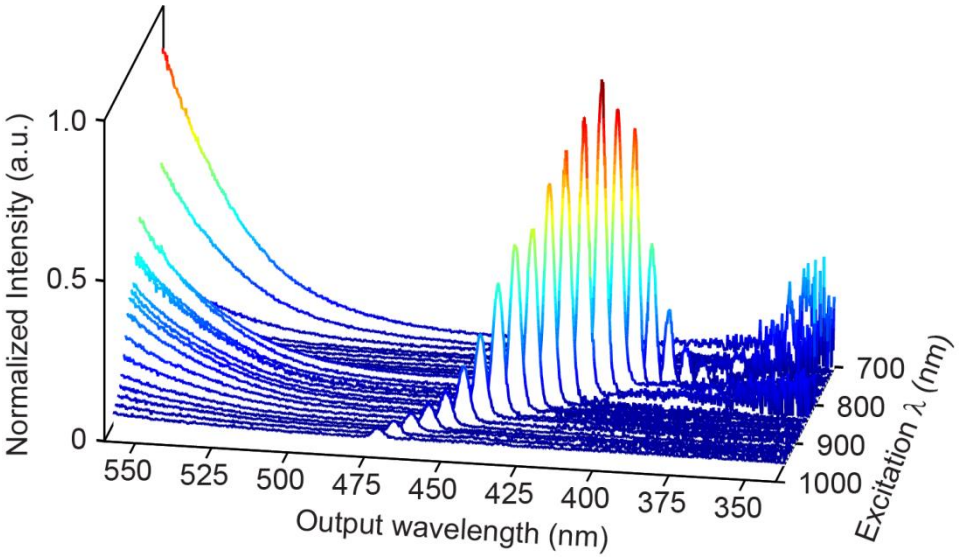

Figure 3.4. Observed spectra of the generated nonlinear output when the metamaterial is pumped at a series of excitation wavelengths of a constant intensity. Each curve corresponds to the generated spectrum at one excitation wavelength, and features a second harmonic peak at $\lambda_\omega/2$ situated on a broadband-background of TPPL.

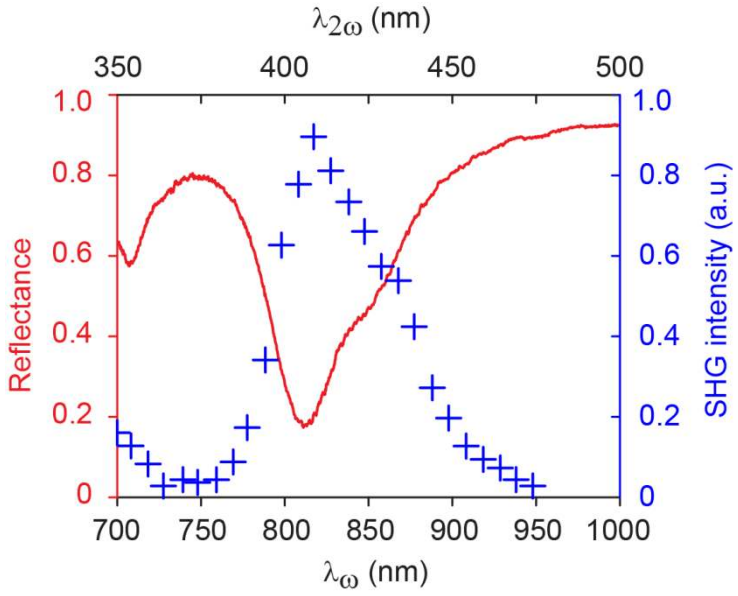

Figure 3.5. Measured wavelength dependence of the linear reflectance (red solid curve) and the SHG excitation spectrum (blue cross symbols), which corresponds to the peaks of the frequency-doubled output obtained in Figure 3.4.

symmetry, second-order nonlinear responses are still possible, due to the symmetry breaking at the metal-dielectric interfaces [112, 113]. Figure 3.4 shows the spectra of the produced nonlinear optical signals when the metamaterial absorber is excited at a constant intensity and the fundamental wavelength varies between 0.7 – 1 μm. For each pump wavelength, the output spectrum features a frequency doubled peak at $\lambda_{2\omega} = \lambda_{\omega}/2$, which is accompanied by a broadband background of two-photon photoluminescence (TPPL) skewed towards longer wavelengths [114]. While TPPL is known to be more efficient when pumped at a relatively short wavelength, the spectral data in Figure 3.4 indicates that it is enhanced, to a certain extent, by the resonance effect at the excitation wavelength of ~810 nm.

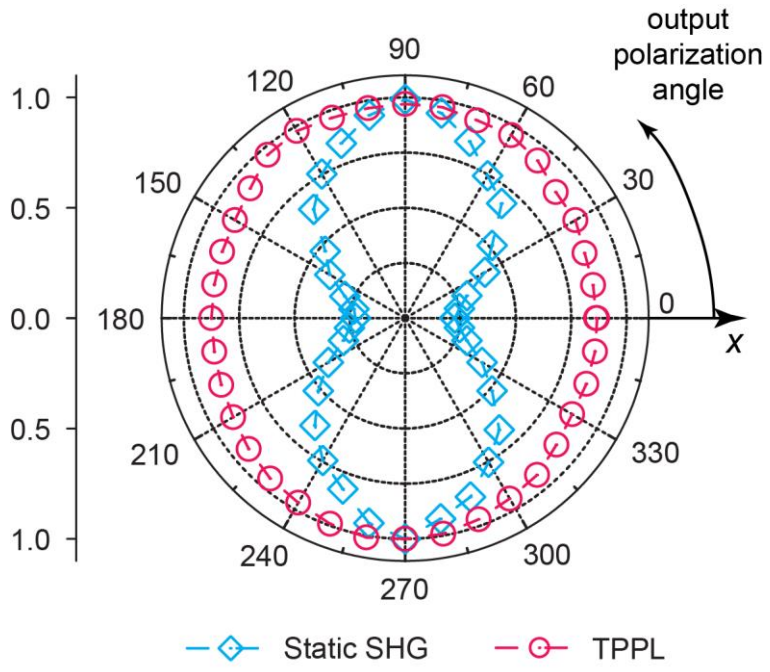

Figure 3.6. Polarization properties of SHG (cyan squares) and TPPL (pink circles) in absence of applied voltage. Data are normalized to their respective maximum values. The pump light is linearly polarized along the 0° direction in the polar diagram (i.e., the *x*-axis in Figure 3.1).

To elucidate the resonance behavior of the SHG efficiency in the narrow-band metamaterial absorber, we collected the information in the frequency-doubled peaks in Figure 3.4 and integrated to produce the SHG excitation spectrum shown in Figure 3.5. Also included in Figure 3.5 is the measured linear reflection spectrum. As expected, the SHG reaches its peak value when pumped near the linear reflection dip because of the device's absorption maximum at 810nm. Similar correlations between nonlinear optical generation and linear resonance behavior have been observed in other plasmonic systems including textured nano-apertures and arrayed nano-antennas [115, 116]. The two components of the generated nonlinear signal are not only distinguished by the spectral

features associated with SHG and TPPL but also by the distinct polarization behaviors of these two frequency up-conversion processes. As shown in Figure 3.6, the polarization of SHG emission is predominantly directed normal to that of the fundamental wave, as governed by the second-order nonlinear tensor, while the TPPL emission stems from incoherent dipoles and is therefore randomly polarized.

3.4. Tuning harmonic generation with voltage signals

The voltage-controlled frequency doubling in the meta-device is directly linked to the resonance-enhanced light concentration at the fundamental wavelength, with its electrical field component predominately aligned collinearly with the externally applied control field. This is made evident from the simulated electric field distribution in the dielectric spacer at both the fundamental and second-harmonic wavelengths, as shown in Figure 3.7. The SHG excitation spectrum in Figure 3.5 indicates the direct correlation between the SHG efficiency and the linear resonance behavior. For this reason, all measurements of the voltage controlled harmonic generation were fixed at a fundamental wavelength of 810 nm, which maximized the SHG output. Figure 3.8a shows the change in the second harmonic output $\Delta I_{2\omega}(V)$, normalized to the static $I_{2\omega}(V = 0)$ as a function of the control field. The result reveals a linear dependence of the frequency-doubled output on the externally applied voltage, with an electric-field induced nonlinear modulation of ~ 9% observed at $V_{DC} = 10\ V$. A similar effect is obtained when the device is driven by an AC voltage signal, as shown in Figure 3.8b. The linear dependence of $I_{2\omega}$ on the magnitude of electrical control is beneficial for EFISH-based signal processing because electrical signals can be encoded into the frequency-doubled light generation with minimal distortion. For both the conventional SHG and the EFISH generation, the

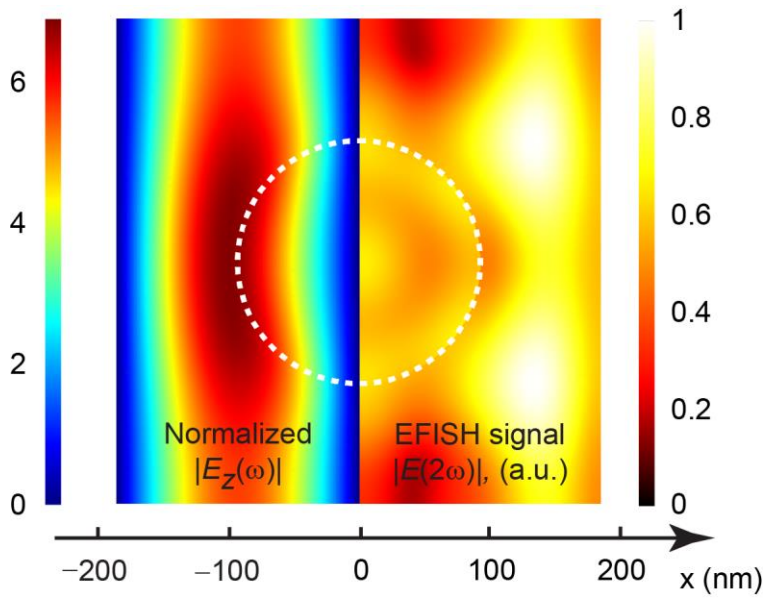

Figure 3.7. Electric field distributions within the dielectric spacer for both the fundamental wave at ω (left half, normalized to the electric field magnitude of the incident wave) and the frequency doubled signal at 2ω (right half). The fundamental wavelength corresponds to the resonance peak where perfect absorption occurs. Only half of the unit cell is shown for each frequency because of the geometrical symmetry with respect to $x = 0$. The white dashed circle indicates the location of the hole.

quadratic relation between SHG output and the fundamental intensity I_ω is a signature characteristic. This feature is confirmed in Figure 3.9, where a slope $K = 1.9$ of least-squares fit is identified in the double logarithmic plot.

3.5. Electrically-induced and voltage-controlled optical rectification

In the next part of the experimental study, we characterize the optical rectification and its electrical modulation in the metamaterial device. Under excitation of the fundamental wave, the dielectric spacer undergoes a low-frequency nonlinear

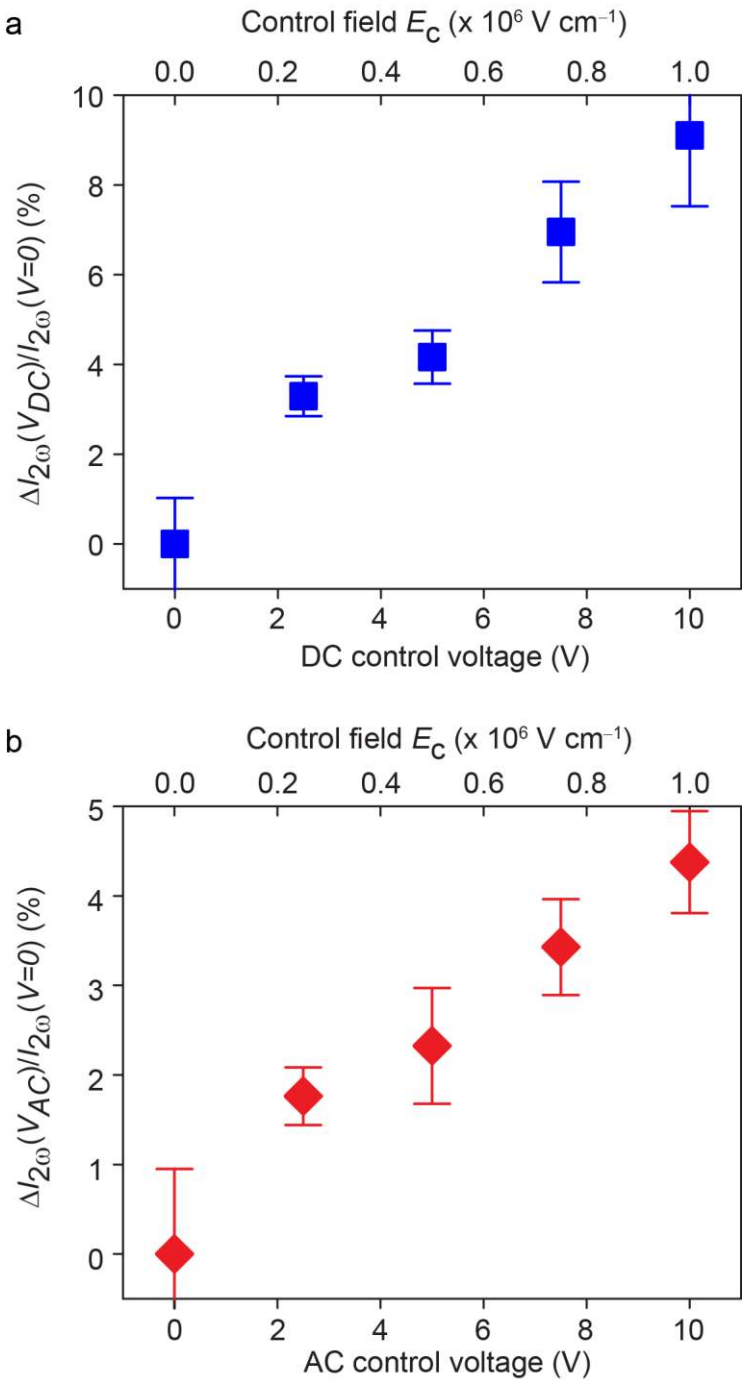

Figure 3.8. The dependence of normalized change in the frequency doubled output $\Delta I_{2\omega}$ on the externally applied (a) DC or (b) AC voltage signals. The corresponding magnitude of the control field E_c is labeled on the upper axis. Linearly polarized pump light at the absorption peak of λ_ω = 800 nm was used at a fixed intensity.

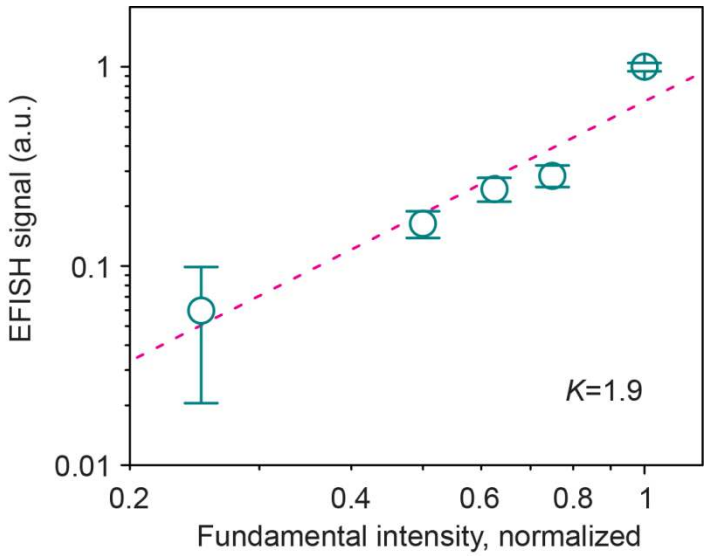

Figure 3.9. The EFISH output $\Delta I_{2\omega}$ as a function of the intensity of the fundamental wave at λ_ω = 810 nm. The control voltage is fixed at V_{AC} = 10 V. A least-squares fit using the function $\Delta I_{2\omega}(I_\omega) \propto I_\omega^K$ is plotted as the dashed line, in which the fit exponent K was found to be 1.9. All error bars represent standard deviations from five measurements.

polarization, causing an induced potential difference across the two metallic parts of the meta-device. The magnitude of this OR signal is critically sensitive to the level of the applied control voltage. Figure 3.10 illustrates the excitation spectra of the OR signal from the metamaterial under a series of DC control voltages, from 0 to 5 V, while the excitation intensity is fixed at a constant level. All data are normalized to the peak OR signal at the bias voltage of 5V. The experimental results reveal that the optical rectification is strongly interrelated to the linear resonance behavior of the metamaterial absorber. Under each control voltage, the detected rectification signal is maximized when the device is pumped at around 800 nm. This resonance characteristic near 800 nm in Figure 3.10 closely follows the device's linear absorption behavior shown in Figure 3.5.

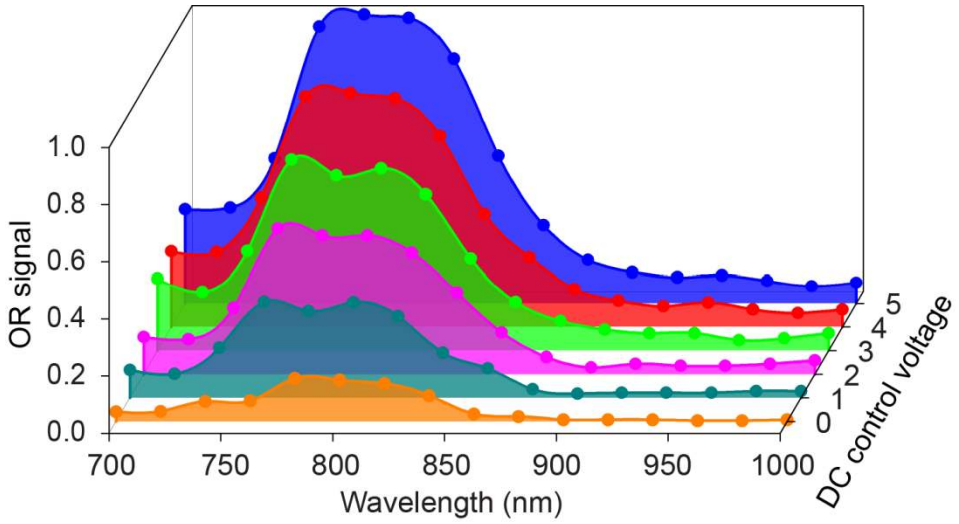

Figure 3.10. Measured excitation spectra of the optical rectification signals under different levels of externally applied DC voltage, where the metamaterial device is excited at a series of wavelengths of constant intensity. The experimentally collected data are represented by the solid dots, and the boundaries of the colored regions are to guide the eye.

The optical rectification signal, which emerges as an additional, light-induced open voltage across the capacitor-like metamaterial absorber, is proportional to the corresponding quasi-DC polarization $P^{OR} \propto I_\omega \cdot \chi^{OR}$, where I_ω is the excitation intensity and χ^{OR} represents the effective second-order nonlinear susceptibility between the two metallic parts. The metamaterial is designed to support enhanced light intensity in the dielectric spacer within the resonance band of its linear absorption. This explains the similar resonance feature in the excitation OR spectra in Figure 3.10.

More importantly, the generation of OR in the metamaterial device is predominantly enabled, and therefore can be purposely tuned, by the applied control voltage. The amorphous dielectric spacer is in lack of a $\chi^{(2)}$ response (except for the symmetry-breaking boundary), as indicated by the very limited magnitude of the OR

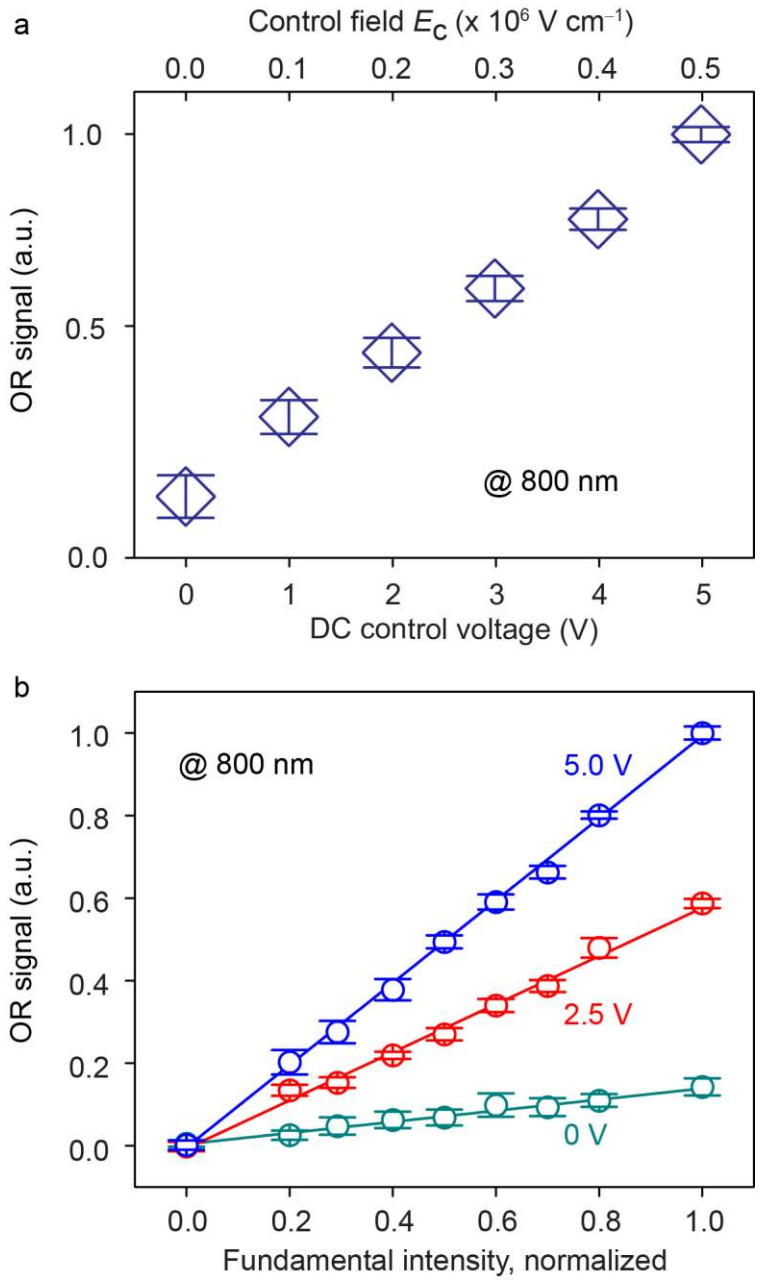

Figure 3.11. (a) The dependence of the optical rectification output on the applied voltage when the metamaterial is pumped with fixed intensity at the wavelength of 800 nm. The corresponding magnitude of the control field E_c is labeled on the upper axis. (b) The OR signal as a function of the intensity of the excitation light at 800 nm, when the control voltage is set to 0, 2.5 and 5V, respectively. The solid lines are the least-squares fits to the experimental data. All error bars represent standard deviations from five measurements.

signal in the absence of the bias voltage. The nonlinear susceptibility χ^{OR} contributing to the OR generation is mostly electrically induced, following $\chi^{OR} = \chi^{(3)} E_c$ where $E_C = V_C / d$ is the applied control field. Consequently, the EFIOR signal is proportional to the bias voltage, as depicted in Figure 3.11a where the magnitude of the optically rectified signal is plotted against the externally applied voltage for an excitation wavelength within the resonance band. The result indicates electrical tunability of the OR signal with a modulation depth of approximately 130 % per volt relative to the OR level in the static (V_C = 0) case. Another signature characteristic of the OR effect is the linear relation between the rectification signal and the intensity of the pump light. This is confirmed in Figure 3.11b, where the OR generation is plotted as a function of the excitation intensity at the wavelength of 800 nm. At each control voltage, the slope of the least-square fit line is directly related to the electric-field-induced χ^{OR}. To evaluate the voltage-enabled portion of rectification signal, or EFIOR, we subtract the baseline (V_C = 0) from the OR data in Figure 3.11b and obtain a ratio of 1.93 between the two slopes of OR curves at the control voltage of 5 and 2.5 V, respectively, which confirms the relation $\chi^{OR} = \chi^{(3)} E_c$ that governs the EFIOR generation in the metamaterial absorber.

3.6. Discussion

We conducted a range of control measurements to confirm that no detectable SHG emission or optical rectification beyond the noise level from the bare substrate or unpatterned metallic devices exists. This confirms that the observed nonlinear signals originate from a light concentration effect in the metamaterial absorber. As for the up-conversion efficiency of the EFISH process, we take into account all the experimental

factors and conservatively estimate the efficiency to be 2×10^{-11}. This magnitude of efficiency is comparable with the reported value for the plasmonic EFISH device [20] and that of conventional nonlinear crystals under a similar experimental condition. When both the second and the third order nonlinear susceptibilities are present, the total SHG intensity $I_{2\omega}$ from the nonlinear medium becomes $I_{2\omega} \propto I_{\omega}^{2}\left|\chi^{(2)} + \chi^{(3)}E_c\right|^{2}$, where I_{ω} represents the intensity of the fundamental beam and E_c is the static or low frequency electric field resulting from the control voltage. Therefore in the EFISH generation, the voltage-induced component of SHG can be expressed as $\Delta I_{2\omega}(E_c) \propto I_{\omega}^{2}\left(\left[\chi^{(3)}E_c\right]^{2} + 2\chi^{(2)}\chi^{(3)}E_c\right)$. Consequently, the comparative magnitudes of $\chi^{(2)}$ and $\chi^{(3)}E_c$ determine whether the relation $\Delta I_{2\omega}(V_C)$ is quasi-linear or quasi-quadratic. The linear modulation for both DC and AC control voltage indicates that the $2\chi^{(2)}\chi^{(3)}E_c$ term, which depends on both $\chi^{(2)}$ and $\chi^{(3)}$, dominates over the $[\chi^{(3)}E_c]^2$ term in our experiment. The electrical tunability of the OR signal is much larger than that of the EFISH process, primarily because of the low level of the baseline OR in absence of an applied voltage. Without a control field, the OR-induced potential difference across the meta-device stems only from the residual $\chi^{(2)}$ response in the gap, while in SHG the entire metallic pattern can contribute to the overall frequency-doubled output.

In conclusion, we have demonstrated an electrically active nonlinear metamaterial device, in which second harmonic generation and optical rectification can be purposely controlled by applied voltage signals. Our result leverages some of the most fascinating characteristics of optical metamaterials, namely the dual electrical and optical functionality supported by nanostructured metals, the resonance-enhanced light-matter interactions, and the micrometer scale device footprint with engineered nanoscale

features. This work substantially broadens the scope of metamaterial research in the nonlinear regime and represents a key step towards utilizing optical metamaterials as a self-sufficient platform for electrooptic information processing.

3.7. Methods

3.7.1. Device fabrication

The fabrication of the meta-device including the external electrical wiring involves the following procedures (Figure 3.12, with numbers indicating the sequential steps taken). The device was fabricated on a 1×1 $inch^2$ glass substrate (1). Photolithography was used to define the pattern for the bottom electrical pads along with alignment marks. Photoresist Microposit SC1813 was spin coated on the substrate to form a 1.5 μm thick resist layer (2) and the film was subsequently baked at 115 °C for 60 seconds. After UV exposure (365 nm), the resist was developed in a Microposit MF-319 developer for 60 seconds (3). Using the patterned SC1813 resist as an etching mask, the glass substrate was then dry etched for 40 minutes in a gas mixture of CHF3 (90 %) and O2 (10 %) at a gas pressure of 60 mT and a power of 250 watts (4). With this process, the glass substrate and the photoresist were etched by 100 nm and 700 nm, respectively. The remaining SC1813 resist on the glass substrate was 800 nm in thickness. Next, a 100 nm thick silver layer was electron beam deposited (5), followed by a lift-off process that left the silver layer flush with the glass substrate (6). This trench-filling scheme helps to mitigate the risk of electrical shorting of the top and the bottom electrodes in the complete device. Afterwards, an aluminum oxide layer was deposited over the entire substrate to form the dielectric spacer of the metamaterial (7). An additional role of this

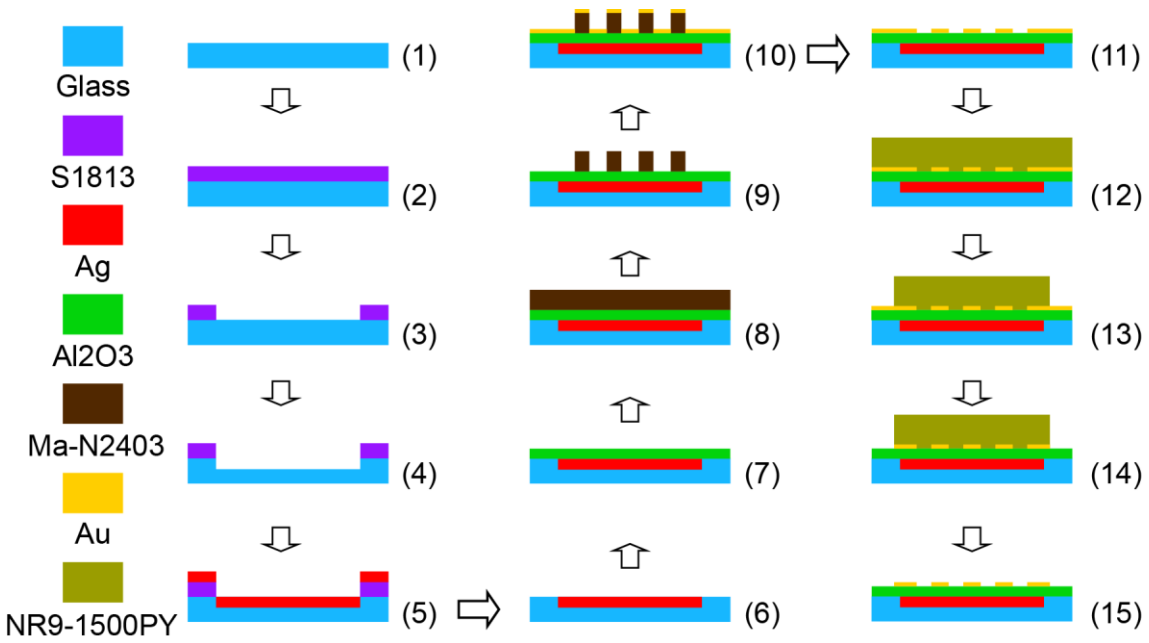

Figure 3.12. Fabrication flowchart of the metamaterial absorber with electric contacts.

alumina film is to insulate the bottom silver pattern from the upper, metallic, patterned electrode. The aluminum oxide film consists of a 50 nm electron-beam evaporated aluminum oxide layer and another 50 nm alumina film deposited by atomic layer deposition (ALD). This is to ensure that the spacer is perfectly insulated so as to withstand a strong electric field induced by the externally applied voltage signal.

The metamaterial pattern with subwavelength features was defined using electron beam lithography (JEOL JBX-9300FS EBL) on a negative electron beam resist, Ma-N2403. A resist layer of 180 nm in thickness was spin-coated on top of the aluminum oxide and then baked at 90 °C for 60 seconds (8). In order to prevent charging effect on the dielectric substrate during the electron beam lithography, a layer of water-soluble conductive polymer Espacer 300z was spin coated on top of Ma-N2403. Aligned electron beam lithography was carried out to form the periodic metamaterial pattern, which was

carefully aligned to a predesigned region of the substrate. The electron beam dose used in this process was set to 760 μC cm^{-2}. After rinsing off the Espacer 300z in DI water for 60 seconds, the exposed electron beam resist was then developed in MF-319 for 70 seconds to form the resist pillars, which correspond to the voids in the metallic pattern (9). Subsequently, a 50 nm thick gold layer was evaporated in an electron beam evaporator (10), followed by a lift-off process using the Microposit 1165a remover at 80 °C for one hour in order to finish the metamaterial pattern in the top metallic layer (11).

On the top of the deposited gold layer, the final set of aligned photolithography steps were performed to define the top electrical pads, the metamaterial area limit, and the on-chip electrical interconnects. A negative photoresist NR9-1500PY was spin coated with a thickness of 1.5 μm and then pre-baked at 150 °C for 60 seconds (12). After the UV-exposure, the resist was post-baked at 100 °C for 60 seconds and developed in Rd6 resist developer for 12 seconds (13). Using the patterned NR9-1500RY resist as the etch stop mask, the entire sample was immersed in the gold etchant GE-8148 for 15 seconds to remove the exposed gold layer (14). When the gold pads and electrical wires were formed, the NR9-1500PY etching mask was removed using acetone, and the complete metamaterial device with electrical functionality was finally accomplished (15).

3.7.2. Optical characterization

The linear spectrum of the micrometer-scale device was measured using a homemade confocal system based on a tungsten-halogen lamp, a monochromator, and an InGaAs detector. In the nonlinear experiments (Figure 3.13), the excitation source for the experimental study was a Ti:Sapphire ultrafast oscillator (Spectra-Physics, Mai Tai HP) with a pulse duration of 100 fs, a repetition rate of 80 MHz, and a tuning range of 690 -

1040 nm. A set of Glan polarizers and half waveplates were employed to control the power level and polarization state of excitation pulses. The fundamental beam was delivered to the metamaterial device mounted on an inverted optical microscope (Zeiss, Axio Observer D1m) with a 10× objective, which resulted in a spot size of approximately 70 μm on the sample. The time-averaged power impinging upon the sample was 60 mW, which translates to a peak intensity of 2×10^{8} W cm^{-2}. Using a switchable beam-splitter, the generated nonlinear signals from the sample were alternatively delivered into either a photomultiplier (PMT: Hamamatsu, H10721-210) or a spectrograph system (Princeton Instruments IsoPlane and Pixis CCD camera) for intensity and spectral analysis. A dispersive prism cascaded with short-pass and band-pass filters were used to prevent the fundamental wave and the broad two-photon photoluminescence (TPPL) background from entering the PMT.

To test the electrical modulations of SHG with DC and AC voltage signals, lock-in measurements were performed with the input of the detector locked to either an optical chopper or a signal generator. In order to obtain a full spectral analysis of the nonlinear signals the fundamental wave was filtered by a long pass filter. This way, the broad spectrum, including both the SHG and the TPPL, was recorded using the spectrograph system. For the detection of optical rectification (OR), a similar lock-in setup was employed with the generated electrical signal locked to the optical chopper, in which OR signals were evaluated as a time-averaged discharging current from the capacitor-like meta-device. This current signal is proportional to the light-induced, the additional voltage generated across the two metallic layers, which stems from the line integral of the OR electric field across the dielectric spacer of the metamaterial. We note that the

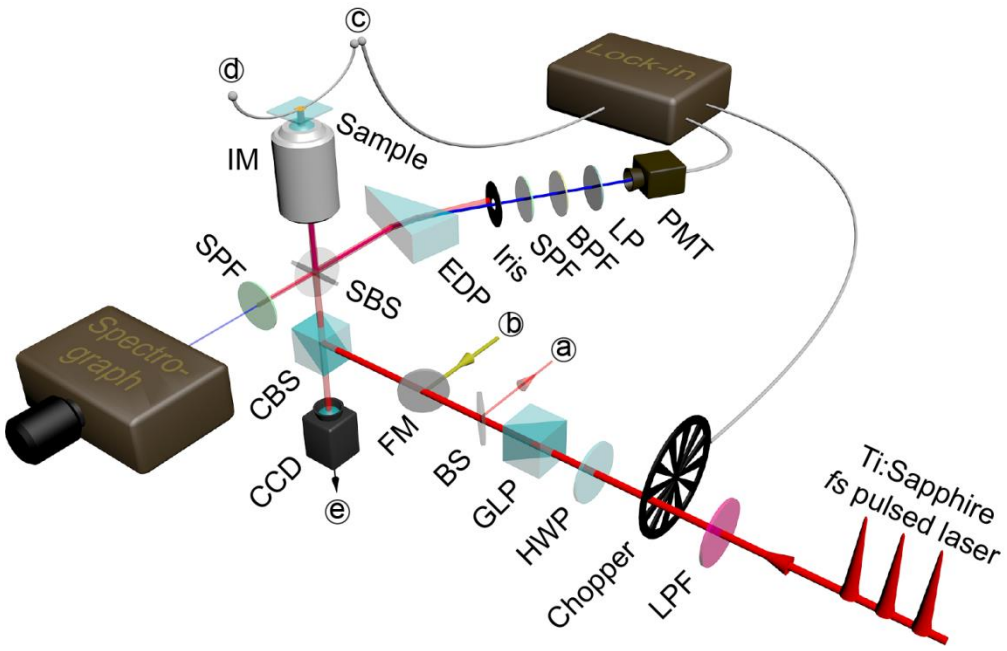

Figure 3.13. Experimental setup for characterizing nonlinear effects in a metamaterial device. Abbreviations for optical components: LPF – long-pass filter; HWP – half waveplate; GLP – Glan laser polarizer; BS – beam sampler; FP – flip mirror; CBS – cube beamsplitter; SBS – switchable beamsplitter; IM – inverted microscope; EDP – equilateral dispersive prism; SPF – short-pass filter; BPF – band-pass filter; LP – linear polarizer; PMT – photo multiplier tube. Index of labeled ports: a) spectrometer; b) illuminating light source; c) AC or DC voltage supply; d) ground; e) video monitor.

detected current signal is a direct consequence of optical rectification, and the control voltage of a constant level does not produce this current in the absence of excitation with ultrashort laser pulses. In addition, a spectrometer at port a) and a video camera on microscope at port e) were used to monitor the pulse status of the Ti:Sapphire oscillator and the beam alignment at the sample respectively. All measurements were conducted under ambient temperature.

3.7.3. Numerical simulations

Full-wave numerical models of both the linear and the nonlinear properties of the metamaterial devices were performed by modifying the equation system of a commercial finite-element package (COMSOL). For the linear optical behavior, the light absorption was computed as a function of the wavelength and the angle of incidence (Figure 3.14). Two coupled electromagnetic models, one for the fundamental and the other for the SHG, were used in the nonlinear modeling and were solved interactively to generate

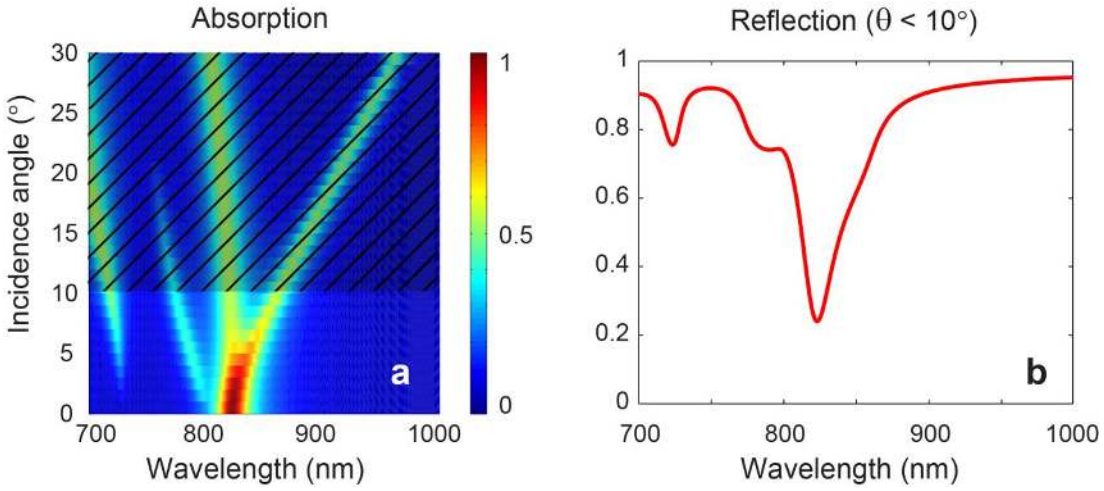

Figure 3.14. Simulation results for the linear spectrum of the metamaterial absorber. a, Absorption of the metamaterial as a function of wavelength and angular incidence. The absorption is evaluated as the average absorption level under both the TE and the TM illuminations, $A^{\theta} = \left(A_{TE}^{\theta} + A_{TM}^{\theta}\right)/2$. The half-angle of the illumination cone in the experiment is approximately 10°, as represented by the unshaded region. b, The angle-averaged reflection spectrum of the metamaterial absorber. Taking into account the angular extent of the illumination cone, the reflection curve is obtained by averaging the spectra for all angles of incidence below 10°.

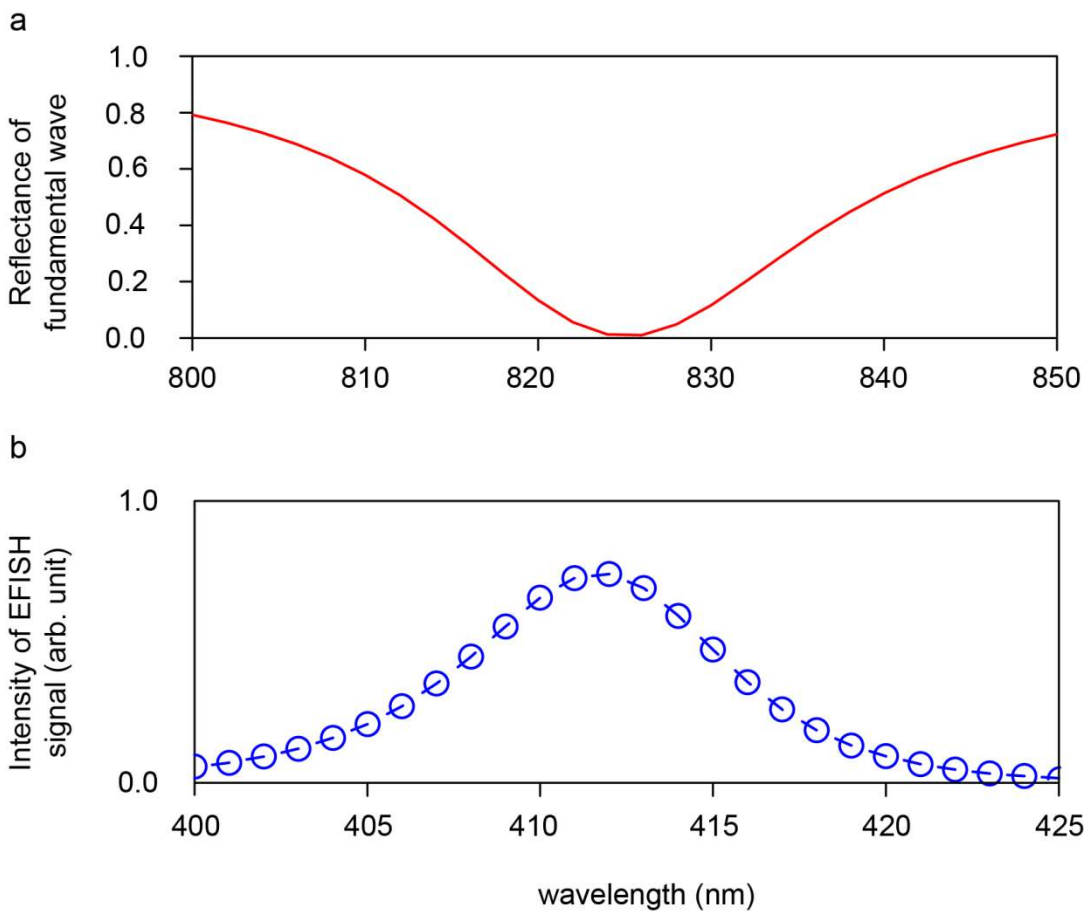

Figure 3.15. Correlation between the linear resonance behavior and the EFISH generation efficiency of the metamaterial absorber. a, The wavelength-dependent reflectance of the fundamental wave, which is a zoomed view of the reflection spectrum shown in Figure 3.2 in the main text. b, The excitation spectrum of the EFISH signal, which is numerically obtained when the structure is excited at a constant intensity of varying fundamental wavelengths.

the field distributions of both waves. The simulated results reveal the correlation between EFISH generation from the metamaterial absorber and the absorption behavior of the metamaterial for the fundamental wave (Figure 3.15). The intensity of the EFISH output peaks at the excitation wavelength where the linear reflectance reaches the

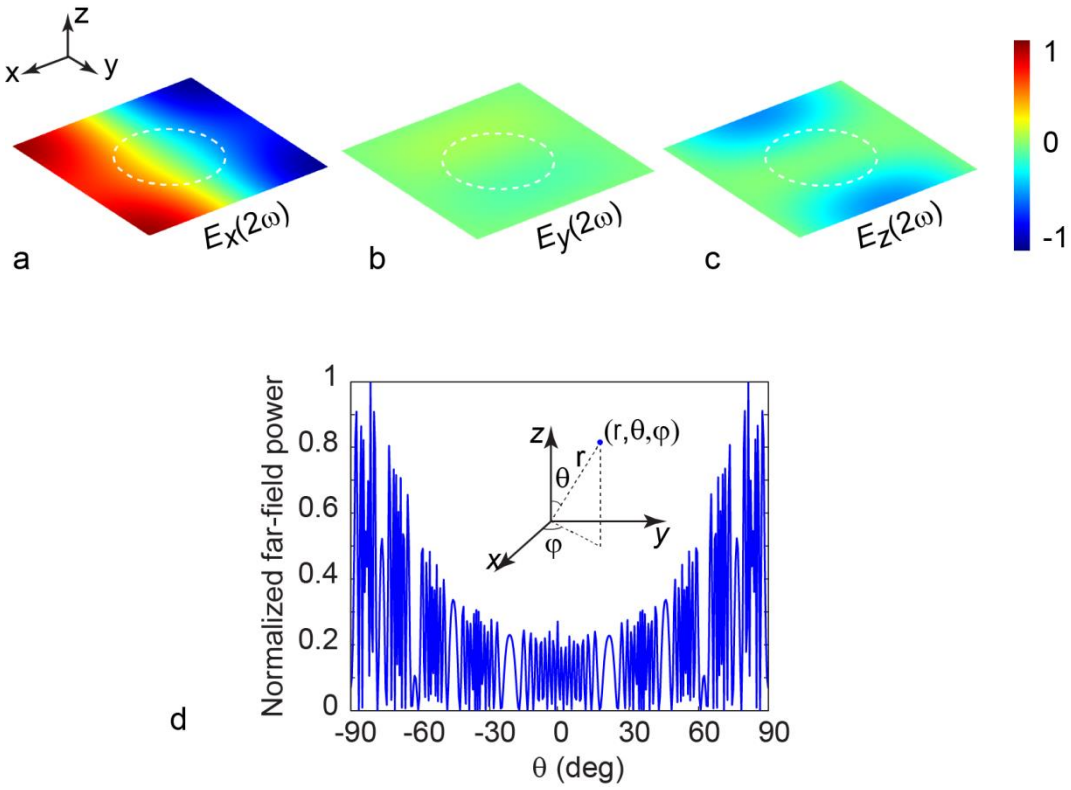

Figure 3.16. Simulation results for the distribution of the EFISH signals in both the near- and far-fields. a-c, Unit-cell simulations of the electric field map of the EFISH signal in the plane 500 nm above the top surface of metamaterial absorber. The dashed circles indicate the projection of the hole in this plane. d, Normalized far-field distribution of EFISH power at the φ=0 plane. Inset shows the spherical coordinate system used in the NTFF transformation.

minimum, a rather intuitive conclusion given the quadratic dependence of EFISH generation on the local intensity of the fundamental light.

The nonlinear signals from the device were further evaluated using a near-to-far-field (NTFF) transformation technique, where the distribution and intensity of the frequency-doubled output in the far zone were calculated based on the simulated data of SHG in the close proximity of the device [41, 117]. Specifically, all vector components of the electromagnetic fields at the harmonic frequency were obtained using unit-cell based simulations. A virtual surface, 500 nm above the top surface of the metamaterial, was selected as the source of the far-field radiation, on which the surface electric and magnetic currents were computed from the simulated field distributions. As described by the surface equivalence theorem, the radiated fields above this virtual surface are uniquely determined by the equivalent currents on the surface. The currents' information was further translated to vector potentials, based on which angular distribution of light in the far field can be obtained by evaluating the time-averaged Poynting vector per unit solid angle (Figure 3.16). The normalized angular distribution of the EFISH power in the far-field indicates relatively weak radiation near the surface normal of the metamaterial absorber. Given the 10× objective used in our experiment with an NA of 0.25, approximately 8% of the entire generated EFISH signal enters the objective for further optical detection. The collection efficiency could be potentially improved by better design of the top metallic patterns such that the 2ω signal from the metamaterial radiates with a better, controlled directionality in the EFISH process.

CHAPTER 4

ELECTRICALLY TUNABLE HARMONIC GENERATION OF LIGHT FROM PLASMONIC STRUCTURES IN ELECTROLYTES

4.1. Overview

Plasmonics has provided us with a unique opportunity to control the flow of light at the nanoscale. As a technology driving optical applications, plasmonics has enabled routing, light concentration, and active control of optical waves with subwavelength device footprints [40, 45, 55, 70, 83, 118, 119]. Collectively, ordered arrangements of plasmonic building blocks constitute photonic metamaterials with optical properties not observed in materials available in nature or synthesizable by conventional means [56, 67, 69, 71, 100, 102, 120]. Moreover, metallic nanostructures serve not only the role of plasmonic media for designated optical functions, but also conventional purposes of metals for voltage bias, carrier injection, and current extraction. This compelling feature renders plasmonic structures a versatile platform for optoelectronic signal generation and processing. Although still relatively sparse in the literature, plasmonic devices with built-in electrical functions have revealed the potential of nanometallic structures for dual electrical and optical functionality. Examples in this context include plasmonic modulators with electrooptic media placed inside plasmonic cavities or waveguides [39, 121, 122], and spectral tuning in metamaterials when electrically switchable materials such as a liquid crystals are adjoined to the metallic structures [123, 124]. Patterned metallic films are also exploited for ultra-thin photovoltaic cells, where subwavelength hole- or slit-arrays were adopted to enhance the light trapping capability and

simultaneously serve as electrodes for the collection of photocarriers [125, 126]. Plasmonic structures also enable the direct transduction of optical information to electrical signals in metals, by means of diverse processes including plasmoelectric potential generation and the photon drag effect [95, 96, 127, 128].

The simultaneously supported electrical and optical functions in nanostructured metals also facilitate electrically controlled nonlinear optical processes, such as electric-field-induced second-harmonic (EFISH) generation. In contrast to conventional second harmonic generation (SHG, $\omega + \omega \rightarrow 2\omega$), EFISH originates from the coupling of applied control fields (E_c) to the third-order nonlinear susceptibilities ($\chi^{(3)}E_c \rightarrow \chi_{eff}^{(2)}$, or, $\omega + \omega + 0 \rightarrow 2\omega$). EFISH generation has been demonstrated in a variety of material platforms, including voltage-biased bulk crystals and within depletion regions of semiconductor junctions [19, 129-132]. It has also been exploited as a powerful tool for the characterization of organic nonlinear chromophores [133, 134]. Very recently, we have demonstrated that various nonlinear wave-mixing processes, including harmonic generation and optical rectification, can be electrically manipulated in plasmonic resonators and metamaterials [20, 93]. The frequency-doubled output from the feed gap of a plasmonic antenna or the dielectric spacer of a photonic metamaterial is shown to be externally controlled by applied voltage signals. Using similar but different mechanisms, voltage-tunable harmonic generation of light has also been reported from bipolar parallel-plate capacitors with titania inclusion and field-effect transistors based on transition metal dichalcogenides [135, 136]. In a recent demonstration, EFISH generation has been used for the realization of unconventional phase-matching schemes such as backward phase-matching in negative index materials [94].

4.2. Tunable nonlinear generation from a plasmonic crystal in electrolytes

In this work, we push electrically-controlled nonlinear plasmonics beyond the scope of solid state structures and experimentally demonstrate tunable nonlinear generation of light enabled by an electrically active plasmonic crystal in aqueous electrolytic solutions. The ion-attracting plasmonic crystal consists of an array of nanoholes perforated in a metallic film. This structure is reminiscent of a geometry prominently featured in the early days of plasmonics, developed for extraordinary optical transmittance [31]. Today it still serves as a powerful testbed for various applications including biochemical sensing based on index-induced spectral shifts [137-139]. When the plasmonic crystal is electrically biased against a reference electrode, the electric field from the bound layer of ions amassed on the metal surface modifies the effective nonlinear susceptibility at the interface, and thus actively modulates the harmonic signal generated from the hybrid plasmonic-electrolyte system. Thanks to the electrically active control of the plasmonic crystal situated in a K_2SO_4 solution, the localized enhancement of the optical field from the hole array is met with a highly concentrated layer of ions at the metal-solution interface when a voltage bias is applied, leading to a gigantic modulation depth of approximately 150%/V of the harmonically generated signal. This work offers the exciting new potential to use plasmonic nanostructures for voltage-controlled nonlinear signal generation and in-situ biochemical sensing in an aqueous environment.

Surface second harmonic generation emanates from the broken symmetry induced by either structural discontinuity or field discontinuity at an interface. The former arises

from the disparity between the two media composing the boundary, which results in symmetry breaking even if the bulk materials are centrosymmetric. The latter comes from the rapid variation of the electric field normal to the surface, and typically dominates second-order nonlinear optical processes at liquid interfaces [57]. While SHG is forbidden under the electric dipole approximation in bulk materials that have inversion symmetry, it is naturally endorsed at the interface where the symmetry is necessarily broken. Consequently, SHG is widely exploited as a non-invasive optical means for the study of surfaces and interfacial states of various materials [7, 140-143]. As for metal-dielectric interfaces, the broken symmetry therein is closely related to the density profile of electric charges at the metal surface [14, 112]. In a hybrid system consisting of both metals and ionic solutions, the surface charge density of the metal is critically influenced by the electric potential of the metal, which facilitates electrical tuning of SHG from such ion-rich metallic surfaces. Earlier experiments have demonstrated the feasibility of voltage-tuned SHG from planar metallic surfaces in electrolytic solutions [144-150], but the intrinsically weak nonlinear responses and the electric field node at the planar metallic surface mitigates the full potential of this technology for sensing and other applications. In the present work, we aim to explore resonance enhanced, electrically tunable harmonic generation of light from plasmonic nanostructures with a pronounced nonlinear modulation depth.

4.3. Design of the plasmonic structure

The configuration of the electrically controlled plasmonic crystal in an electrolytic solution is illustrated in Figure 4.1, where two electrodes are placed into an aqueous solution of ionically charged molecular structures. The lower electrode consists of a

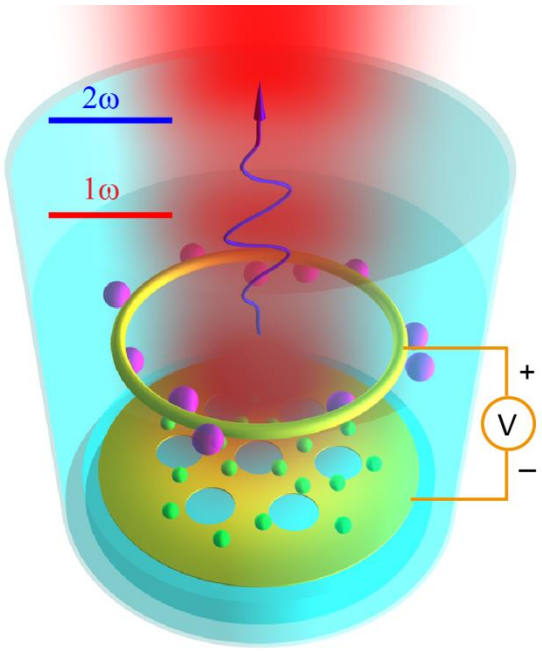

Figure 4.1. Schematic for electrically active harmonic generation of light from a plasmonic crystal in an aqueous solution. When a voltage is applied, a thin layer of ions is accumulated over the surface of the nanostructured metal, and therefore induces an effective nonlinear susceptibility that enables frequency doubling of light.

plasmonic crystal specially designed to engender electrolyte characterization, maximal electric field enhancement at an excitation wavelength of ~840 nm, and optimal voltage induced capabilities with a relatively large coverage of metal. The upper electrode is the reference electrode in a ring shape, which facilitates both the excitation for the fundamental light (red) at normal incidence and the signal collection of the harmonic wave (blue) generated from the device. The plasmonic crystal is designed with the honeycomb structure array so that the material has a high transmittance at the operating wavelength, but is primarily useful to maximize surface to electrolyte interaction. The honeycomb structure allows for the electrolyte species to enter into the cavities of the

array thereby enhancing the likelihood of broken symmetry necessary for creating second harmonic generation. Presented in Figure 4.2a is a scanning electron microscopy (SEM) image of the fabricated sample. The 150 nm thick gold plasmonic crystal on the glass substrate has a pitch of 500 nm and a radius of 150 nm for the hole. The gold film is deposited onto the glass substrate with e-beam evaporation (CHA e-beam evaporator). Gold is chosen for reducing the reactivity with the electrolytic solution. The honeycomb structured array is patterned with a standard electron-beam lithography process (JEOL JBX-9300FS EBL).

An EFISH signal can be produced when a pulsed laser is incident on a charge separated dielectric medium, where an external D.C. voltage induces the charge

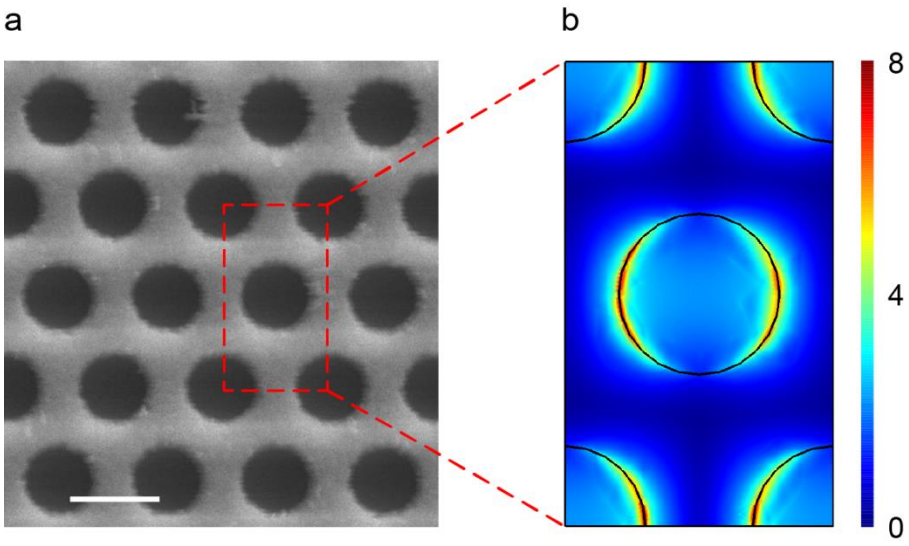

Figure 4.2. (a) SEM image of the fabricated plasmonic crystal, which consists of a hexagonal array of nanoholes in a gold film. The scale bar at the bottom represents 400 nm. (b) Enhancement of the electric field magnitude at the surface of the metallic structure under normal incidence at the excitation wavelength of 840 nm. The electric field magnitude is normalized to that of the input light.

separation. Typically, the charge separation in the medium induces the broken symmetry necessary to instigate the third order susceptibility tensor. The ionic units influence the charge density of the metal electrodes, thereby providing a larger form of symmetry breaking when aggregated at the surface of the plasmonic crystal. In the presented set-up of Figure 4.1, the voltage bias is produced with the help of the two electrodes. Interaction of laser pulses with the charge-accumulated surface, in conjunction with only minor voltage levels, provides the necessary inputs to create distinguishable nonlinear output signals.

The intensity of the second harmonic signal is positively related to both the nonlinear susceptibility and the square of the fundamental electric field. In order to maximize the SHG, the plasmonic crystal is designed to have an optimum field enhancement at a specified fundamental wavelength. The field enhancement at the metal surface is mapped in Figure 4.2b using a full wave simulation package when a light wave at a wavelength of 840 nm impinges upon the gold plasmonic crystal normally through the surrounding water. The field enhancement is defined as the electric field magnitude on the metal surface normalized to that of the incident field. A field enhancement of ~8 times is observed, implying an enhancement of 64 times in the local light intensity as presented in Figure 4.2b.

4.4. Linear optical responses

Linear optical responses of the plasmonic crystal in air and water environments are characterized both numerically and experimentally. Using the tabulated optical parameters of gold [151], we simulate the transmission spectra through the plasmonic device at normal incidence (Figure 4.3a). The plasmonic resonance in the air is expected

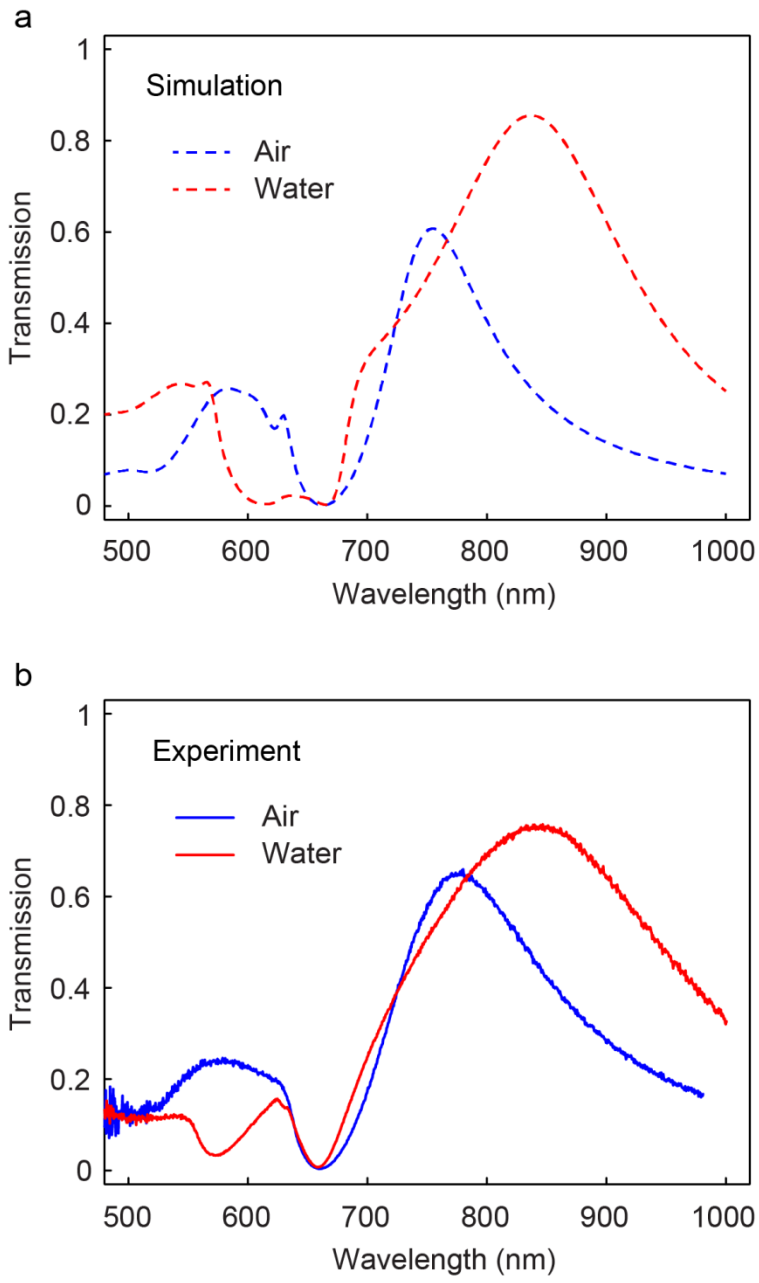

Figure 4.3. Linear optical responses from the plasmonic crystal. (a) Numerically simulated transmission spectrum of the plasmonic crystal in air (blue) and in water (red), respectively. (b) Experimentally measured transmission spectrum of the sample in both ambient and aqueous environments, which nicely replicates the simulated results shown in part (a). The transmitted light from the sample is normalized to that of the transparent substrate under the same illumination conditions.

to occur at a wavelength of ~760 nm (dashed blue) and would red-shift to ~840 nm when the plasmonic crystal is immersed in water (dashed red). The resonant wavelength of the plasmonic crystal, ~840 nm, is designed such that it is around the center of the tuning range of our ultrafast laser. Moreover, the corresponding wavelength of the second harmonic wave is far from the interband transition wavelength of gold. Transmission spectra are experimentally measured under the illumination of a broadband light source (Figure 4.3b), where the transmitted light through the sample is normalized to that of the transparent substrate under the same illumination condition. The resonant peaks at ~760 nm in air (solid blue) and ~840 nm in water (solid red) match very well with the full-wave simulated results shown in Figure 4.3a.

4.5. Second-harmonic generation in electrolytes

Depicted in Figure 4.4 is the harmonic generation of light from the plasmonic crystal in the electrolytic solution without an externally applied voltage. A typical image from the spectroscopic camera is provided in the upper part of Figure 4.4, in which photons of different frequencies are horizontally spread by the grating inside the monochromator and detected by the pixels of the camera. The bright spot in the image indicates an accumulation of photons at a wavelength of 420 nm denoting a strong second order nonlinear conversion from the input fundamental light at 840 nm. The light tail trailing to the right of the SHG spot represents the two-photon luminescence (TPL) in the sequence of two-photon absorption process, which is another nonlinear optical process related to the imaginary part of the third-order nonlinear susceptibility. Ultrafast pulses at a fundamental wavelength of 840 nm, with a time-averaged power of 250 mW and a beam diameter of ~50 μm impinges on the plasmonic crystal area, yielding a frequency

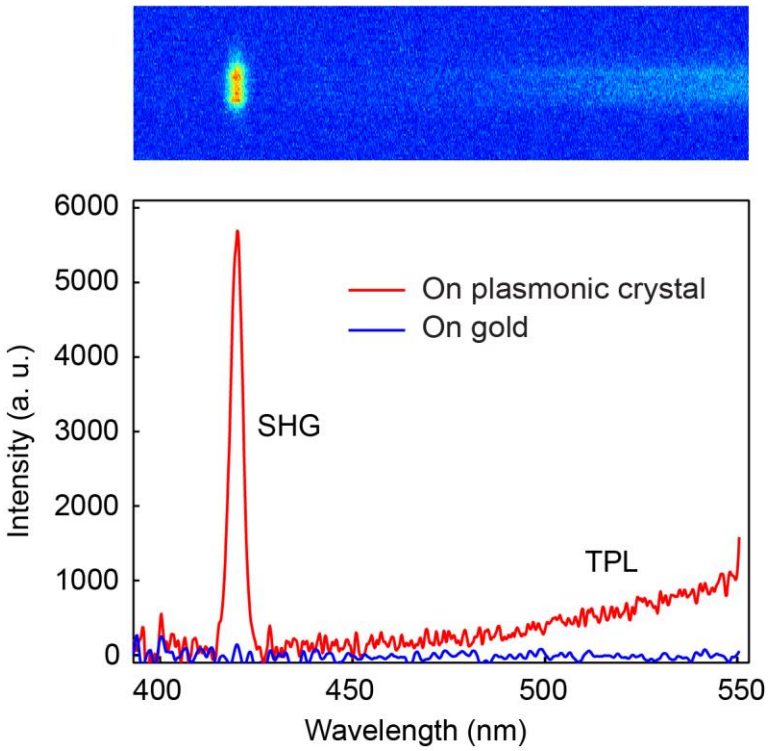

Figure 4.4. Typical nonlinear optical spectra from the system without an externally applied voltage. A spectral image of the generated nonlinear signal is depicted in the top panel. Strong nonlinear optical generation emerges from the plasmonic structure (bottom, red) when excited near the resonance of λ_ω = 840 nm), while no nonlinear signal beyond the noise level can be detected from an unpatterned metal film (bottom, blue)

doubled peak (420 nm) in the spectrum shown in the lower part of Figure 4.4 (red). Under the same illumination conditions, no observable SHG or TPL signals beyond the noise level can be detected when the light impinges on the smooth gold area. This data shows that the efficiency of nonlinear optical generation is boosted by several orders of magnitude, which stems from both the broken symmetry of the engineered metallic surface and the field enhancement offered by the plasmonic resonance.

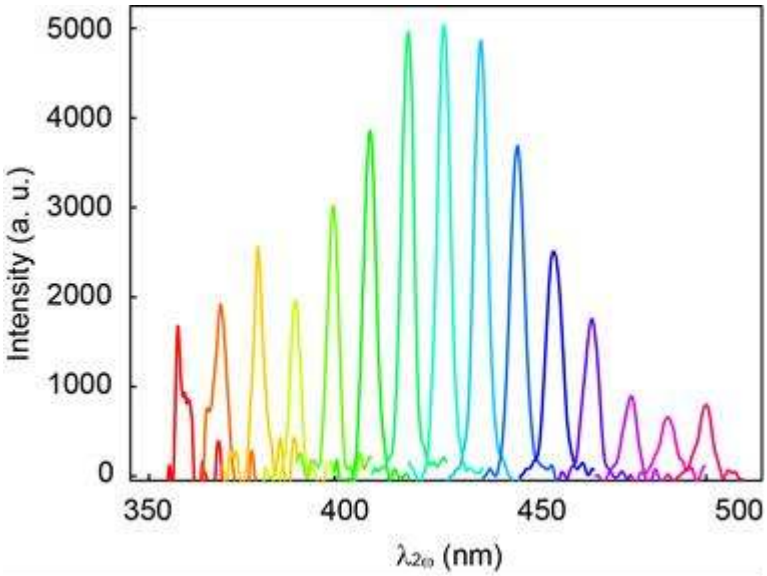

Figure 4.5. Second harmonic generation at a series of excitation wavelengths, while the intensity of the fundamental light is maintained at a constant level. The resonance behavior follows well with that of the linear response.

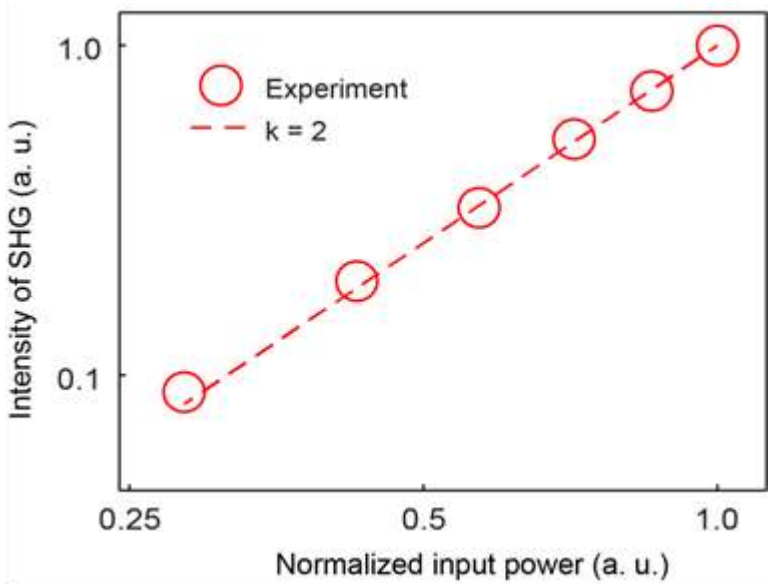

Figure 4.6. Dependence of the SHG on the power of the fundamental light at the excitation wavelength of λ_ω = 840 nm. The dashed line represents a function $I_{2\omega} \propto I_\omega^k$ with a quadratic slope of $k = 2$ in the logarithmic graph.

The second harmonic process generated within the plasmonic crystal was performed at a series of excitation wavelengths under a constant pump power. The intensity profile of the emission spectra illustrated in Figure 4.5 follows the tendency of the linear response, where the intensity of the SHG signal is corrected by the camera response, grating efficiency and all other dispersion factors introduced in the system. The strongest resonant peak of maximum SHG efficiency is observed at an excitation wavelength of ~840 nm, which clearly demonstrates the correlation between the surface plasmon resonance and the nonlinear optical generation. We also measured the excitation power dependence of the SHG under the fundamental wavelength of 840 nm (Figure 4.6). The dashed line represents the characteristic quadratic dependence of $I_{2\omega} \propto I_{\omega}^{k}$ in the logarithmic graph, where k = 2. The measured intensities (circles) at different excitation powers are normalized to that of the maximum pump power, and the curve reveals a perfect quadratic dependence of the harmonic signal on the intensity of the fundamental light.

4.6. Electrically tunable nonlinear optical signal

The central part of this research is the electrical tunability of the nonlinear optical signal, which stems from the voltage-controlled charge accumulation effect when the metallic structure interfaces an electrolytic solution. Figure 4.7 illustrates a schematic of the experimental setup, where ultrafast laser pulses are focused on the plasmonic crystal placed in an electrolyte solution. A voltage bias is applied between the ring electrode and the plasmonic crystal to actively tune the SHG from the plasmonic-electrolyte hybrid system. The objective used for focusing the fundamental wave also serves to collect the

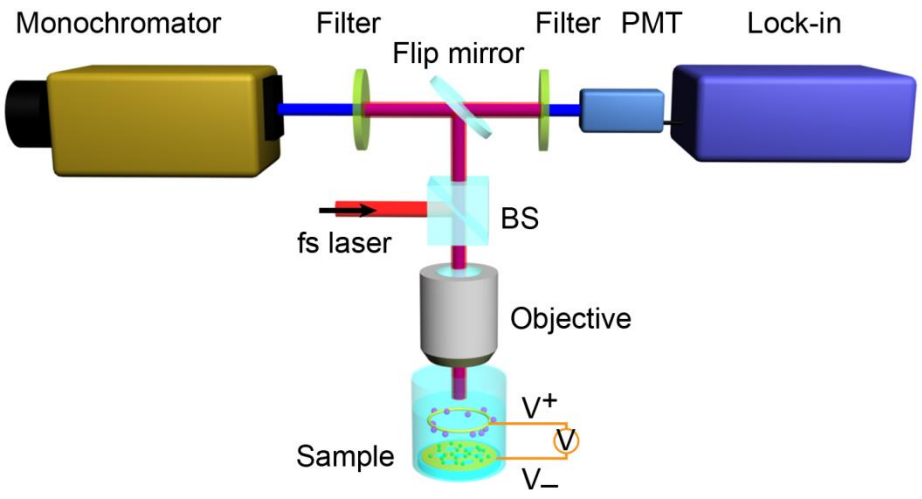

Figure 4.7. Schematic of the experimental setup. The system is pumped with an ultrafast laser, and the generated harmonic signal is detected by either a spectroscopy system or a PMT with a lock-in amplifier. BS, beam splitter; PMT, photomultiplier tube.

generated SH signal through the gold ring. After filtering out the photons at the fundamental frequency, the generated harmonic signal is directed to different detection ports, including a photomultiplier and spectroscopic camera.

In the absence of an applied voltage, SHG at the interface stems from the bulk and surface components $\chi_B^{(2)}$ and $\chi_S^{(2)}$ of the effective second-order nonlinear susceptibility tensor. By applying a voltage across the electrolyte, an extra effective quadratic susceptibility is introduced. This electrically-induced, second-order susceptibility can be approximated as $\chi_{eff}^{(3)}\sigma/2\varepsilon$, where $\chi_{eff}^{(3)}$ denotes the effective cubic susceptibility of the metal, and σ/ε represents the electric field on the interface due to a surface charge density σ, which is proportional to both the ion concentration and the potential drop $\Delta\phi$ across the interface. The potential drop in this expression can be written as $\Delta\phi = \phi - \phi_{PZC}$, where ϕ is

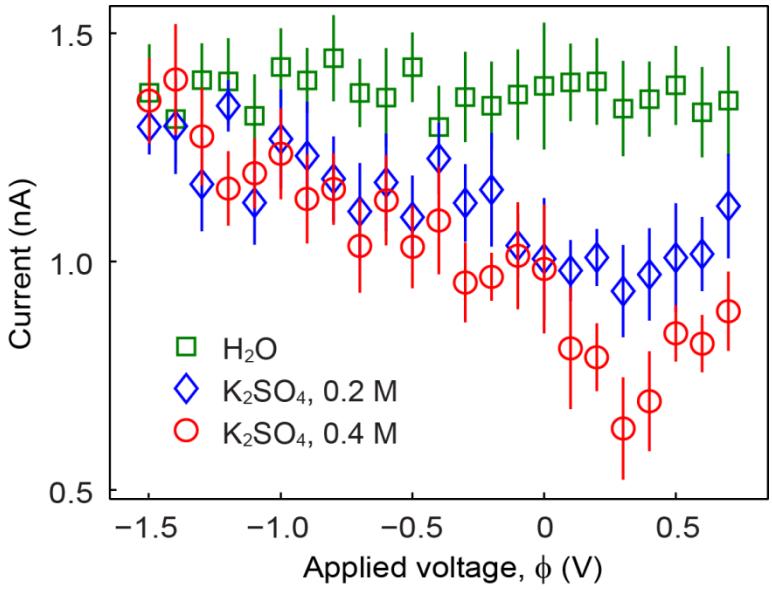

Figure 4.8. Levels of the outgoing harmonic signal at various bias voltages in both deionized water and two different concentrations of K_2SO_4 solution. While negligible voltage dependence of SHG is observed from the plasmonic structure in water (green), the SHG demonstrates a parabolic dependence as the applied voltage (ϕ) is tuned from -1.5 to 0.7 V. At the potential of zero charge (~0.3 V), a minimum in the frequency doubled signal is detected for both 0.2 M (blue) and 0.4 M (red) K_2SO_4 solutions. Error bars represent standard deviation from ten consecutive measurements.

the applied voltage and ϕ_{PZC} is the potential of zero charge.[57] The total intensity of the harmonic signal sums from all these contributions as $I_{2\omega} \propto \left|\chi_B^{(2)} + \chi_S^{(2)} + \chi_{eff}^{(3)}\,\sigma/2\varepsilon\right|^2$.

Now with the electrode system under a voltage bias, we first measured the second harmonic signal from the plasmonic crystal in deionized water at the resonant excitation wavelength of 840 nm, without introducing an ion-rich electrolyte. As shown in Figure 4.8 (green), the frequency-doubled signal remains at a constant level, with negligible dependence on the voltage applied across the electrodes. This is because the applied

electric field across the macroscopic distance between the electrode pair exerts little influence on the effective nonlinear susceptibility at the surface of the metallic structure. With the introduction of a potassium sulfate (K_2SO_4) electrolyte, cations (K^+) and anions (SO_4^{2-}) in the solution are driven towards opposite electrodes when a voltage is applied. With ions accumulated at the metallic surface, especially the cavity region that has enhanced light intensity, the second-order nonlinear susceptibility at the metal-electrolyte interface is effectively modified, which in turn impacts the efficiency of the SHG process. When the plasmonic crystal acts as the positive electrode ($\phi > 0$) and anions (SO_4^{2-}) thusly accumulate on the metallic surface, the SHG signal varies parabolically to the applied voltage, with a minimum occurring at the potential of zero charge, ~0.3 V (Figure 4.8, blue). The potential of zero charge of gold electrodes can be affected by pH of the solution, surface condition and other electrochemical effects. The observed ϕ_{PZC} in K_2SO_4 solution matches well with the value in the references where standard calomel electrode (SCE) was used.[52,57] With a negative voltage applied, the electric field drives K^+ cations to the plasmonic surface, and the SHG keeps increasing as the applied voltage apart from the potential of zero charge ϕ_{PZC}. For comparison, we also performed a similar measurement with a K_2SO_4 solution at an elevated concentration of 0.4 M. As shown in Figure 4.8 (red), the voltage-induced modulation depth becomes larger when the ion concentration of the electrolyte is increased, but the overall trend as well as the characteristic potential of zero charge (the SHG minimum at ~0.3 V) remains unaltered. Using the SHG at $\phi = 0$ as the reference, the electrical tunability of the frequency-doubling process reaches 150 %/V with 0.4 M K_2SO_4 of the solution. This voltage-induced SHG tunability in the plasmonic-electrolyte hybrid system is remarkable, two

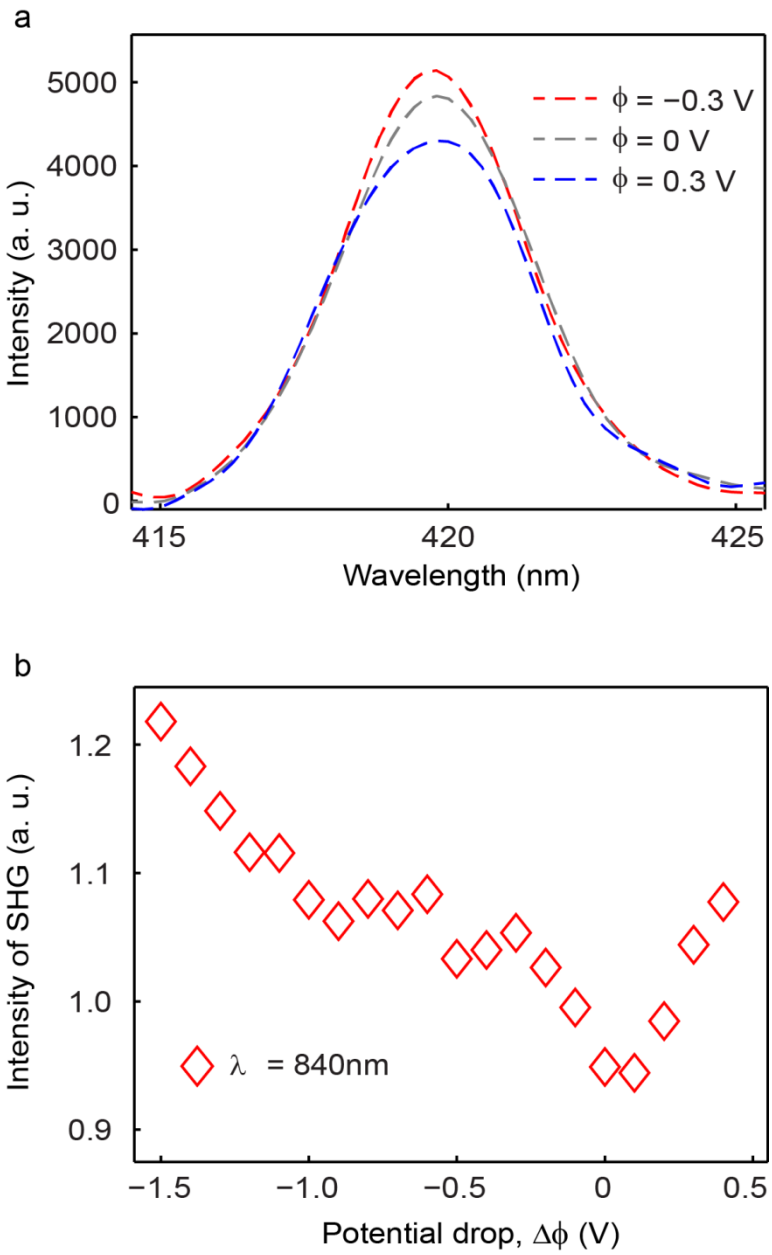

Figure 4.9. (a) SHG spectra at different bias voltages when pumped near the resonance of $\lambda_\omega = 840$ nm. The red, grey and blue curves differentiate between 3 applied voltage biases, –0.3V, 0 V and 0.3 V respectively. (b) Intensity of the SHG as a function of potential drop ($\Delta\phi$). This data was obtained by integration of spectrometer traces, which resembles prior measurements using PMT as shown in Fig 4(b) with $\Delta\phi = \phi - \phi_{PZC}$.

orders of magnitude stronger than that of previous plasmonic and metamaterial-based systems.[33, 34, 38]

The voltage-dependent SHG signals in Figure 4.8 were measured using a lock-in system in conjunction with a photomultiplier. To reconfirm the observed electrical tunability of the nonlinear optical generation of light, we reexamined the SHG signal from the system based on spectral traces and their integration from a cooled spectral imaging setup. Figure 4.9a shows the SHG spectra from the plasmonic crystal in 0.2 M K_2SO_4 solution at three representative voltage levels (unbiased and ±V biased). The impact of ion accumulation on the nonlinear susceptibility at the metal-electrolyte interface depends on not only the concentration but also the species of the ions. Cations (K^+) and anions (SO_4^{2-}) contribute differently to the electrically-induced nonlinear process, as indicated by the non-identical spectral traces for ±0.3 V biases shown in Figure 4.9a. By integration of photon counts of the frequency-doubled signal over a range of voltage biases, we plot in Figure 4.9b the voltage-controlled SHG output at the fundamental wavelength of 840 nm. This graph replicates all the major features we have observed in the previous lock-in measurement (Figure 4.8), including the general trend, the asymmetric $I_{2\omega}(V)$ parabolic behavior, and the SHG minimum occurring at $\phi_{PZC} = 0.3$ V ($\Delta\phi = 0$ V).

4.7. Summary

In summary, we demonstrate the electrically controlled harmonic generation of light from a plasmonic crystal in electrolytic solutions. A nonlinear modulation depth of ~150 %/V is observed, thanks to the light concentrating ability of the resonant plasmonic

structure as well as the voltage-assisted charge accumulation on the metallic surfaces. The electrical tunability of the frequency doubled signal is sensitive to both the concentration of the ions and the electrolyte species, as indicated by the parabolic behavior of the tuning curve around the zero charge potential of the system. With the ever increasing demand for nanostructured devices, the need for nanoscopic sensing continues to increase and becomes a more pressing issue. Plasmonic interactions provide subtle changes when exposed to variable environments. Demonstrations of sensing under linear excitation conditions have proved fruitful with the use of plasmonics, and this work further illustrates the potential to combine electrical signals with nonlinear optical interactions for the sensing and characterization of charged species in any water based solution. Future investigation on the topic will be focused on incorporating this technique to demanding sensing applications for the detection of a comprehensive set of chemical information including concentration, chirality, pH value, and more.

CHAPTER 5

BACKWARD PHASE MATCHING FOR SECOND HARMONIC GENERATION IN NEGATIVE INDEX MATERIALS

5.1. Overview

The phase-matching condition, resulting from the conservation of photon momentum, is among the most vital aspects to consider when multiple frequencies are mixed in bulk nonlinear media. Strictly speaking, all materials are dispersive and the conversion efficiency of a nonlinear process is critically dependent on the relationship among the wave vectors involved. Taking second harmonic generation (SHG) as an example, phase-matching implies a wave-vector relation of $k_{2\omega} = 2k_{\omega}$ or a refractive index relation of $n_{2\omega} = n_{\omega}$. To achieve these parameters the orientation or temperature of a nonlinear crystal must be fine-tuned, or an approximation can be reached by flipping the crystal axis in a periodic manner. The specific scheme to fulfill the phase-matching requirement is critically dependent on the optical properties of the nonlinear medium, such as the material's chromatic dispersion, crystal anisotropy, waveguiding characteristics, and thermal coefficient of the refractive index [14, 15].

The exotic electromagnetic parameters made possible by metamaterials provoke us to reevaluate the established rules of phase-matching for nonlinear optical interactions. As one of the most exciting frontiers in optics and materials science, metamaterials have enabled unprecedented flexibility in producing unconventional optical properties that are not observed in the past [45, 56, 67, 71, 100, 102, 152, 153]. The linear responses of metamaterials have substantially augmented the linear properties available from

naturally-occurring materials. Similarly, the studies of nonlinear metamaterials may have a revolutionary impact on the entire field of nonlinear optics [40, 50, 55, 105, 106, 154-156][11-19]. A particularly fundamental topic to reconsider is the set of novel relations necessary to achieve constructive nonlinear frequency conversion when one of the mixed waves has a negative index of refraction. For example, when a metamaterial possesses opposite signs in its indices of refraction at the fundamental and the second harmonic frequencies, phase-matched frequency doubling requires that the indices for the fundamental and harmonic waves have the same magnitude but opposite signs. Since the Poynting vector and the wave vector in a negative-index medium are antiparallel to each other, the harmonic output will travel towards the source of the fundamental wave[20-23]. This new type of phase-matching condition, known as "backward phase-matching" or "nonlinear mirror" in negative index media, has been predicted for years, but an experimental verification at optical frequencies is still lacking. The difficulty in experimentally validating this condition arises in the production of a bulk optical negative index medium of many wavelengths in length and additionally the perfect, simultaneous tailoring of the refractive indices at both ω and 2ω frequencies to meet the aforementioned conditions.

In this work, we report the experimental demonstration of backward phase matching for nonlinear generation of light in a negative index material (NIM). Since in NIMs a negative index can occur only within a rather limited frequency range, here we position the refractive index for the fundamental wave (ω) to be positive and for the harmonic frequency (2ω) to fall within the negative-index band. In Figure 5.1, we illustrate the scenarios of frequency doubling in different nonlinear media. A phase

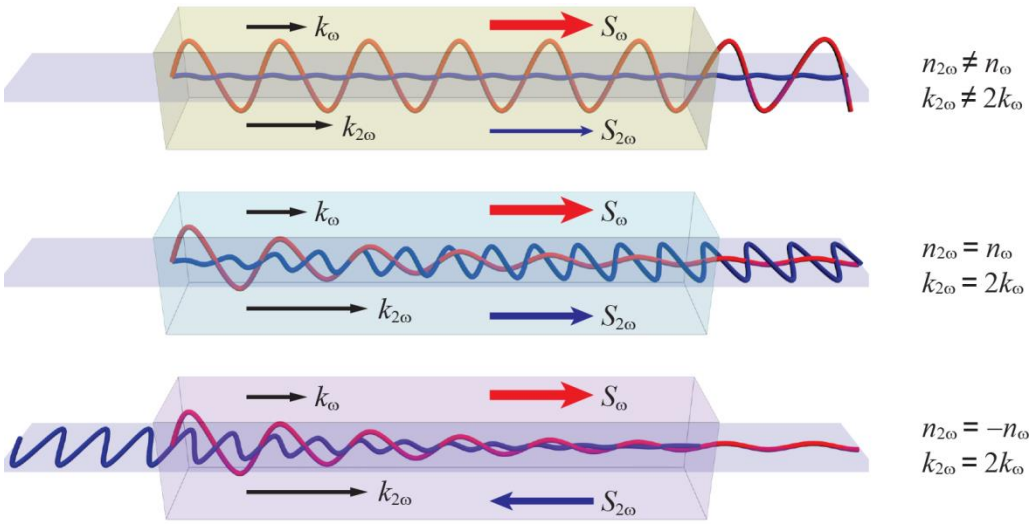

Figure 5.1. Phase matching in a negative-index nonlinear medium. a, Phase matching conditions for second-harmonic generation. The red- and blue-colored lines represent the fundamental and second harmonic waves, respectively. (Top) Low-efficiency frequency doubling of light in a positive-index medium without phase matching ($k_{2\omega} \neq 2k_\omega$, $n_{2\omega} \neq n_\omega$). (Middle) Conventional phase-matching for SHG ($k_{2\omega} = 2k_\omega$), where the fundamental and harmonic waves possess the same index of refraction and co-propagate along the same direction. (Bottom) Backward phase-matching ($k_{2\omega} = 2k_\omega$, $n_{2\omega} = -n_\omega$) in a negative-index material, where the frequency-doubled signal is directed toward the source of the fundamental wave.

mismatch generally leads to a poor conversion efficiency, because constructive SHG occurs only within the coherence length of $l_c = \pi/|k_{2\omega}-2k_\omega|$. The general condition for phase-matching in SHG is $k_{2\omega} = 2k_\omega$, as governed by the law of momentum conservation [14, 15]. Phase-matching implies an infinite coherence length, such that as the fundamental wave is gradually depleted and converted to its second harmonic signal, the source polarization and the generated harmonic field remain in-phase across the length of the nonlinear medium. In a negative index medium with $n_\omega > 0$ and $n_{2\omega} < 0$, however, the

phase matching relation implies that $n_{2\omega} = -n_{\omega}$. Thus, as governed by the Poynting vector, the energy flow in a negative index medium is directed against the phase propagation direction described by the wave vector k. Consequently, when the backward phase matching occurs, the harmonic output grows towards the source of the fundamental light, as depicted in the bottom of Figure 5.1. As a side note, the counter-propagation of the fundamental and harmonic waves can be realized based on an entirely different scheme[24], using quasi-phase-matching instead of a negative index of refraction.

5.2. Negative-index mode in a plasmonic waveguide

To circumvent the difficulty in engineering the effective parameters in a bulk photonic metamaterial across multiple wavelength bands, we realize the index-matching relation of $n_{2\omega} = -n_{\omega}$ by utilizing two distinct modes supported in a plasmonic waveguide. When nonlinear wave-mixing occurs in a waveguide instead of bulk medium, the phase-matching condition for SHG requires the propagation constants of the fundamental and harmonic waves to be identical, which can be satisfied by exploiting the dispersion characteristics of different modes in the waveguide [157, 158]. A metal-insulator-metal (MIM) plasmonic waveguide is typically operated below the surface plasmon frequency ($\omega < \omega_{sp}$), where the dispersion curve $\omega(k)$ has a positive slope below the light line of the dielectric medium in the gap. This regular plasmon mode exhibits a symmetric profile in its magnetic field ("H-symmetric") along with a relatively low loss factor. It has been demonstrated that if the working frequency falls between the surface and bulk plasmon frequencies ($\omega_{sp} < \omega < \omega_p$), the magnetic field component of the dominant propagating mode possesses an asymmetric distribution ("H-asymmetric"). More intriguingly, the

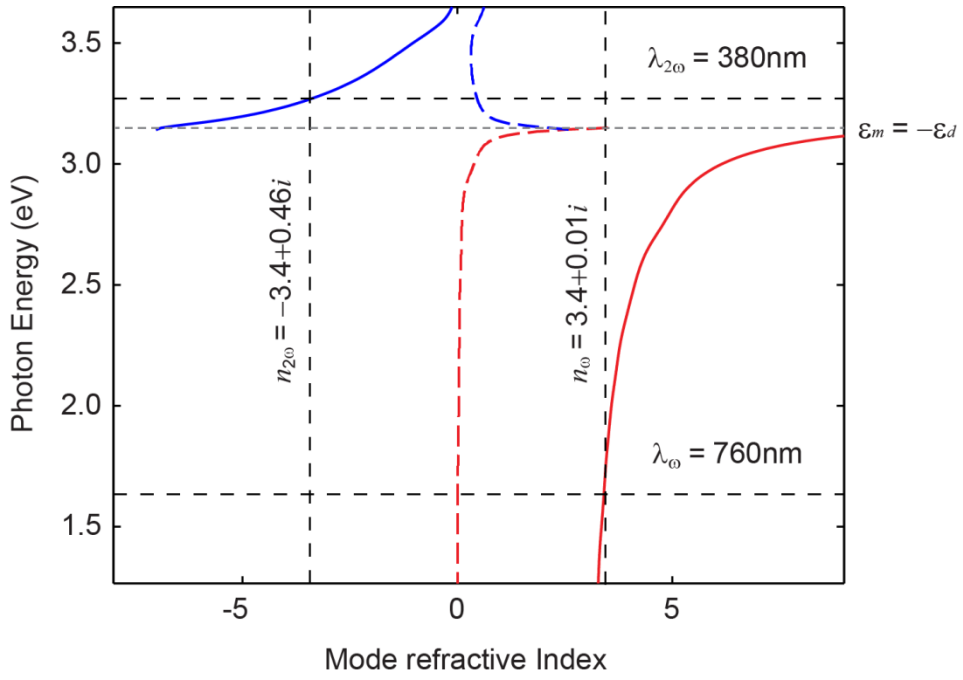

Figure 5.2. Dispersion relations in a silver-dielectric-silver waveguide ($n_d = 2$, $t_d = 30$ nm). The H-symmetric and H-asymmetric modes are represented by the red and blue curves, respectively. Both the real (solid) and imaginary (dashed) parts of the mode refractive index are plotted. The condition for backward phase matching is represented by the marker lines, where $n_\omega = 3.4 + 0.01i$ at $\lambda_\omega = 760$ nm and $n_{2\omega} = -3.4 + 0.46i$ at $\lambda_{2\omega} = 380$ nm.

dispersion relation for this mode is characterized by a negative slope, which leads to an antiparallel relation between the phase velocity ω/k and the group velocity $d\omega/dk$, and consequently, a negative index for the H-asymmetric mode [65, 159-164]. For all propagating waveguide modes, the imaginary parts of the wave vector k and the mode index n must be non-negative, as required by the basic laws of causality and energy conservation. The H-asymmetric mode extends well into the metal and therefore is relatively lossy compared to the regular, H-symmetric mode in an MIM waveguide. The dispersion curves for the plasmonic waveguide used in our experiment are shown in

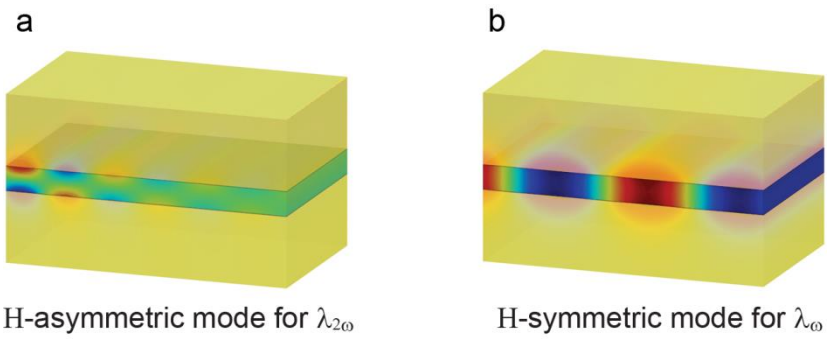

Figure 5.3. Field-mapping for the H-asymmetric mode for $\lambda_{2\omega}$ (a) and the H-symmetric mode for λ_{ω} (b).

Figure 5.2, where a sufficiently thin dielectric spacer of relatively high refractive index (n_d = 2, t_d = 30 nm) is sandwiched between two flat silver films. A large dielectric constant in the gap enables a pronounced separation between the surface plasmon ($\varepsilon_m = -\varepsilon_d$) and the bulk plasmon ($\varepsilon_m = 0$) frequencies, while a narrow gap pushes the operating point away from surface plasmon frequency ω_p and helps to balance the magnitudes of the refractive indices of the two modes. A similar analysis for matching the indices of two distinct modes in a plasmonic waveguide has been numerically proposed before[34]. By optimizing the material and geometry parameters of the plasmonic waveguide, we have located an operational point at which the H-symmetric fundamental wave ($n_\omega = 3.4 + 0.01i$) at $\lambda_\omega = 760$ nm is phase-matched to the generated H-asymmetric harmonic signal ($n_{2\omega} = -3.4 + 0.46i$) at $\lambda_{2\omega} = 380$ nm.

5.3. Challenges for realizing phase-matching

Two immediate challenges stand in the way of realizing phase-matched SHG using the plasmonic waveguide. First, the thin dielectric layer made by typical deposition methods has an amorphous nature and a vanishing $\chi^{(2)}$ response. Second, the two modes

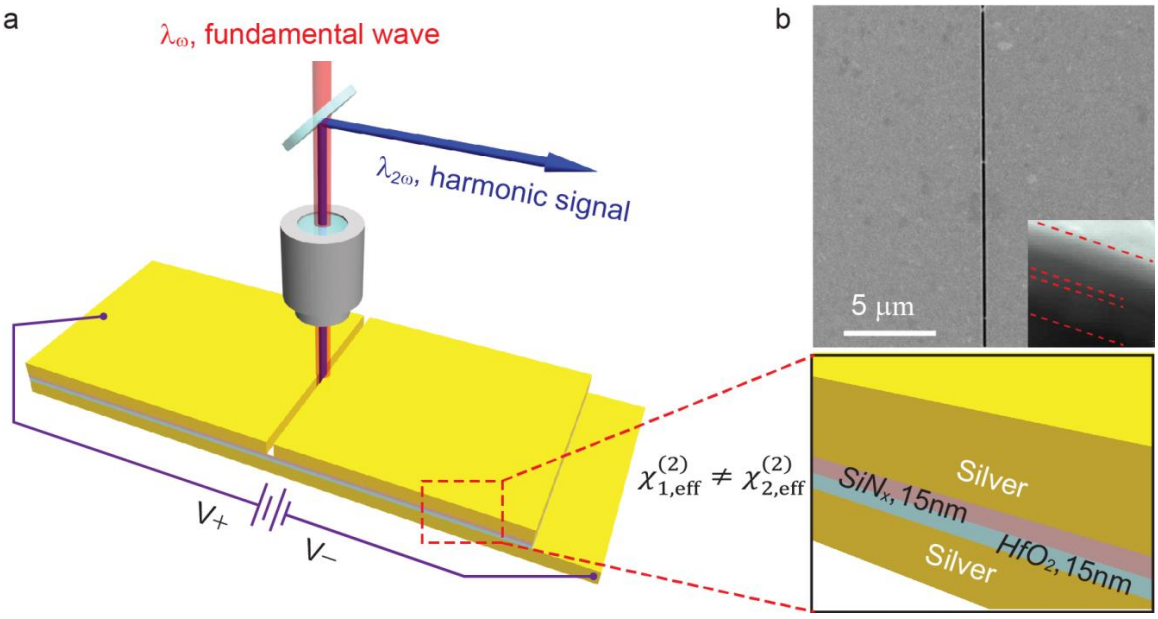

Figure 5.4. Experimental design for backward phase-matching in a plasmonic waveguide. a, Schematic of experimental setup and structure of sample. Nonlinear signals arising from both intrinsic and voltage-induced $\chi^{(2)}$ responses are measured. A nanoslit cut through the top silver layer is used for both excitation and collection. The dielectric spacer of the waveguide consists of two ultra-smooth, 15 nm layers of Si_3N_4 and HfO_2. These layers have similar linear, but distinct nonlinear behaviors to enable strong harmonic generation. b, Scanning electron microscope image of the fabricated structure. Inset is a cross-sectional view illustrating the metallic and dielectric layers.

involved in the proposed SHG process have opposing symmetry, as indicated by the magnetic-field mapping of the fundamental and harmonic modes at the operational point illustrated in Figure 5.3. This mode asymmetry along the transverse direction prevents the nonlinear coupling between the two modes from happening because the nonlinear overlapping factor $S_{i,j} \propto \int_S \chi^{(2)}_{jii} E^{2\omega}_j E^{\omega}_i E^{\omega}_i dS$, which is defined as an integral of the product of the susceptibility $\chi^{(2)}$, the SHG mode, and the square of fundamental mode

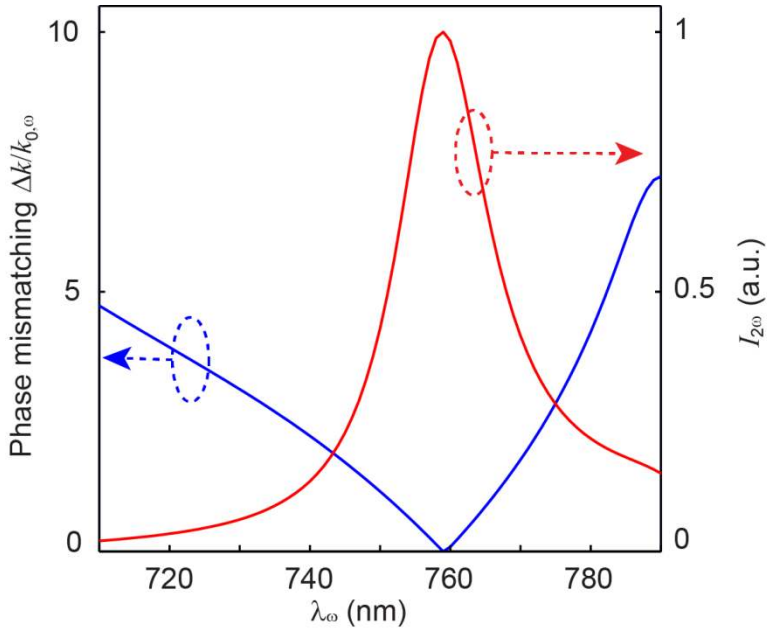

Figure 5.5. Simulated intensity of the backward second harmonic signal (red) and the degree of phase mismatch ($\Delta k/k_{0,\omega}$, blue) at different wavelengths, where $\Delta k = |k_{2\omega} - 2k_{\omega}|$ and $k_{0,\omega}$ represents the wave vector at the fundamental wavelength in the air. The conversion efficiency for SHG peaks at $\lambda_{\omega} = 760$ nm where backward phase-matching occurs ($n_{2\omega} = -n_{\omega}$).

over the entire cross section [165], is precisely zero. These obstacles are overcome in our experiment by exploiting the electrically induced $\chi^{(2)}$ effect in the dual-layered dielectric spacer in a planar plasmonic waveguide, as illustrated in Figure 5.4a. Instead of the regular $\chi^{(2)}$ response intrinsic to noncentrosymmetric crystals and interfaces, here the effective second-order nonlinear effect is produced by the interplay between the ubiquitous third-order nonlinear susceptibility $\chi^{(3)}$ and the applied control field ($\chi^{(3)}E_C \rightarrow \chi^{(2)}_{eff}$) [19, 20, 93]. Moreover, the 30 nm thick dielectric spacer is split into two halves, 15 nm each, made of Si_3N_4 and HfO_2 (Figure 5.4b). These two materials have similar linear ($n_d \approx 2$), but distinct nonlinear behavior and electrical conductivity [166].

As a result, the electrically-induced $\chi^{(2)}$ effect is effectively disabled in one half of the

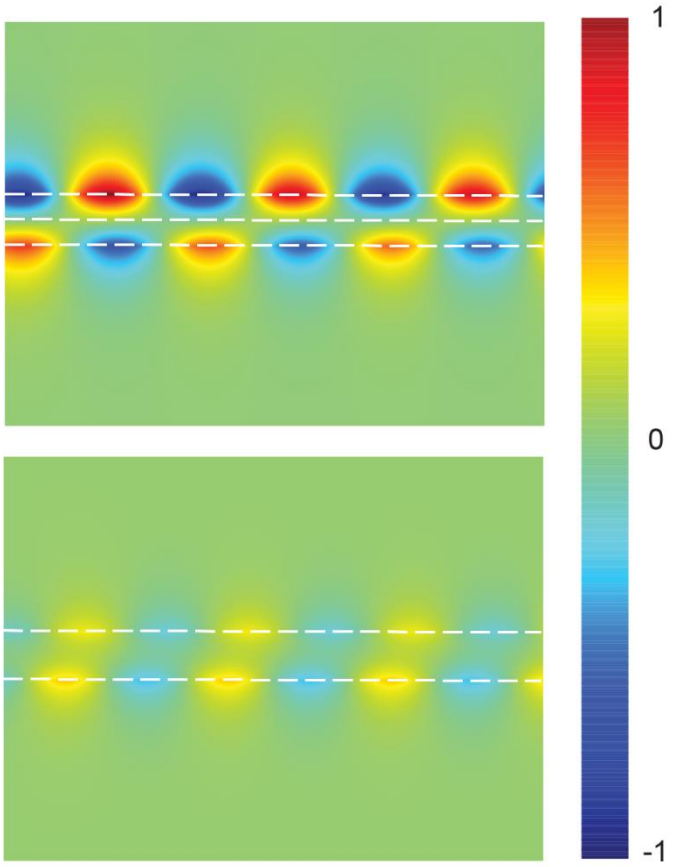

Figure 5.6. Magnetic field mapping for the second-harmonic wave in the plasmonic waveguide with (top) and without (bottom) intentionally induced symmetry breaking. The implementation of symmetric breaking in the nonlinear property is essential for the efficient generation of H-asymmetric SHG mode.

dielectric channel. This induced symmetry breaking gives rise to a non-zero nonlinear overlap factor between the H-symmetric fundamental wave and the H-asymmetric SHG signal, and therefore enables a strong nonlinear conversion between the two modes. In the experiment a nanoslit cut through the top metallic layer serves as the in-coupling entrance for the fundamental light as well as the out-coupling port for the generated SHG

signal. Figure 5.5 shows the full-wave simulation result for the conversion efficiency for the electrically-induced SHG as a function of the fundamental wavelength. The frequency-doubled output peaks at λ_ω = 760 nm, precisely where the backward phase-matching condition of $\Delta k = |k_{2\omega} - 2k_\omega| = 0$ or $n_{2\omega} = -n_\omega$ is satisfied, as determined in Figure 5.2. The importance of the induced symmetry-breaking by using a dual-layered spacer is further illustrated in Figure 5.6, which shows that the amount of generated second harmonic signal will be reduced by nearly two orders of magnitude if a uniform dielectric channel was employed.

5.4. Backward phase-matching

A comprehensive set of measurements has been carried out to experimentally confirm the phenomenon of backward phase-matching in the proposed plasmonic waveguide. Figure 5.7 shows the collected nonlinear spectra under a constant pump intensity at a series of excitation wavelengths λ_ω without an externally applied voltage. The sharp and frequency-doubled peak at each excitation wavelength designates the second harmonic signal, meanwhile broadband background due to multi-photon

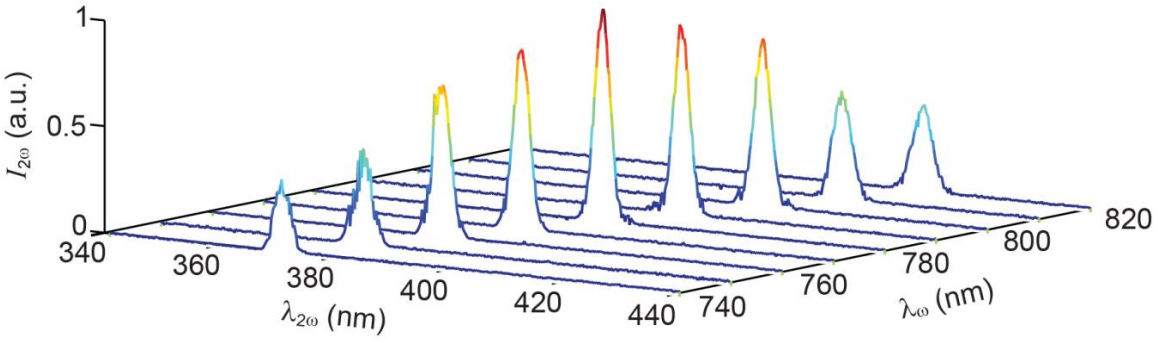

Figure 5.7. Nonlinear spectra from the waveguide at a series of excitation wavelengths λ_ω without an externally applied voltage.

luminescence is negligibly low within the wavelength range of interest. We note that the

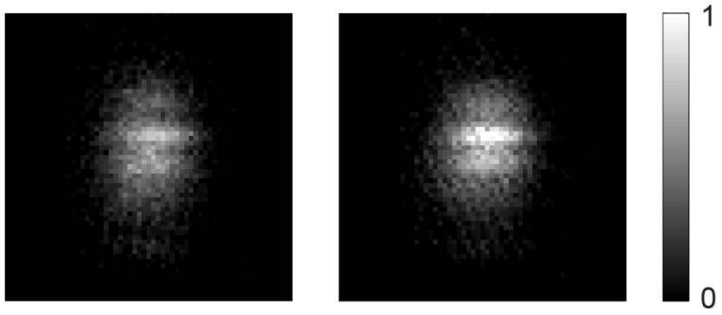

Figure 5.8. Images of second harmonic light spots with (bottom) and without (top) applied voltage at λ_ω = 780 nm.

observed harmonic signal in Figure 5.7 may arise from multiple sources, including the exposed front metallic surface, the focused ion beam milled nanoslit, and the internal metal-dielectric interfaces inside the waveguide. Only the latter can be ascribed to the nonlinear conversion between the aforementioned plasmonic modes. We are able, however, to produce and analyze harmonic signals exclusively stemming from the waveguide core by applying a voltage across the dielectric spacer. This electrically-induced frequency doubling, superimposed onto the regular, static SHG signal (Figure 5.8), is expected to follow the mode index and phase-matching analysis laid out in Figures 5.2 and 5.5. The dependences of the static and electrically-induced SHG levels on the excitation wavelength λ_ω are illustrated in Figures 5.9 and 5.11, respectively. Provided a constant fundamental intensity, a maximum SHG conversion efficiency can be identified at the fundamental wavelength of λ_ω = 780 nm, indicating the existence of backward phase-matching in the plasmonic waveguide. In particular, the measured efficiency curve for the purely voltage-induced SHG signal (Figure 5.11) agrees very well with the theoretical prediction in Figure 5.5, where the peak SHG conversion

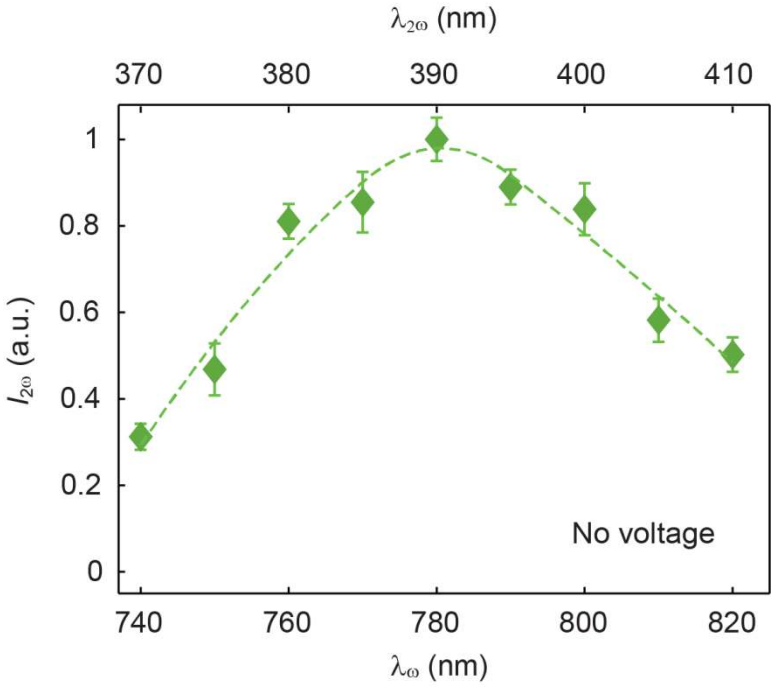

Figure 5.9. The intensity of the static SHG at different excitation wavelengths.

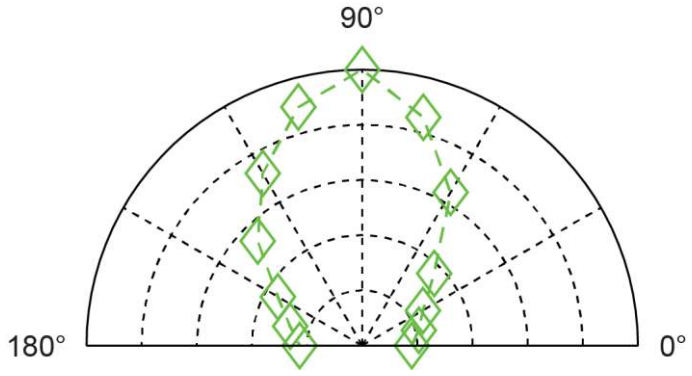

Figure 5.10. The output SHG intensity as a function of the polarization angle of the fundamental light, which is defined as 0° along t*h*e nanoslit and 90° when the input polarization is perpendicular to the slit.

efficiency corresponds to the backward phase-matching condition of $k_{2\omega} = 2k_{\omega}$ and $n_{2\omega} = -n_{\omega}$. The incident pump light can be efficiently coupled into the waveguide only when its polarization is perpendicular to the nanoslit, as evidenced by the polar diagrams in Figures 5.10 and 5.12. In fact, the dependence of the static SHG intensity on the polarization of the fundamental light (Figure 5.10) exhibits an extinction ratio around 5:1, indicating that a small portion of SHG stems from the metallic surface outside of the slit. In contrast, the level of electrically induced SHG is reduced to zero when the fundamental wave is polarized along the nanoslit (Figure 5.12), which serves as an additional validity check that the voltage-enabled SHG is generated inside the designed waveguide because light can only couple when polarized perpendicularly. Thus the signal is generated from an intentionally induced symmetric break with an applied voltage bias and demonstrates a second harmonic conversion efficiency peaking at $\lambda_{\omega} = 780$ where the backward phase matching occurs.

The voltage induced frequency doubling from the plasmonic waveguide features a few characteristics typical to the electrically induced SHG process, such as a linear dependence of the observed SHG on the level of applied bias voltage (Figure 5.13) and a relation between the fundamental and second harmonic intensities given as $I_{2\omega} \propto (I_{\omega})^2$ (Figure 5.14). We note that a number of assumptions have been made in the preceding discussions to simplify our analysis. In the actual sample, the dielectric spacer, consisting of Si_3N_4 and HfO_2 sub-layers, may have thickness fluctuation along the waveguide, which would result in undesired non-uniformity along the propagation direction in both the mode refractive index and the effective second order nonlinear susceptibility induced by the applied voltage. In addition, any difference in the linear refractive indices of the

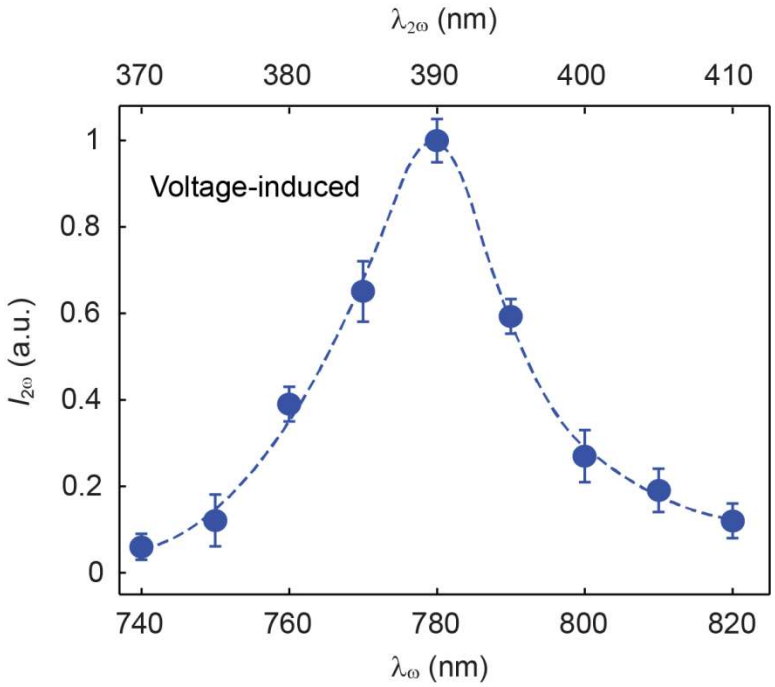

Figure 5.11. The intensity of the electrically-induced SHG at a series of excitation wavelengths. The realization of backward phase-matching is evidenced by the sharp peak in the conversion efficiency at $\lambda_\omega = 780$ nm.

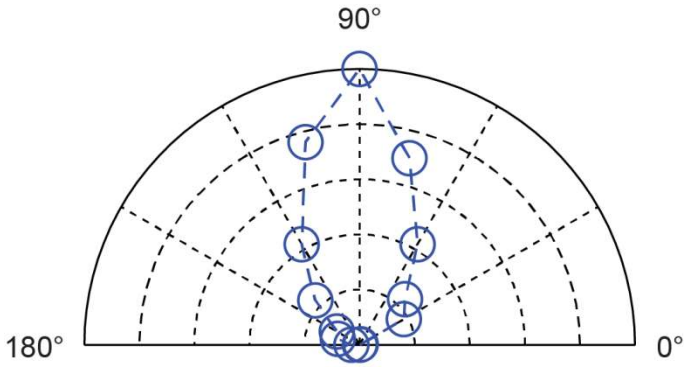

Figure 5.12. The polar diagram illustrates polarization dependence of the voltage-induced SHG at $\lambda_\omega = 780$ nm.

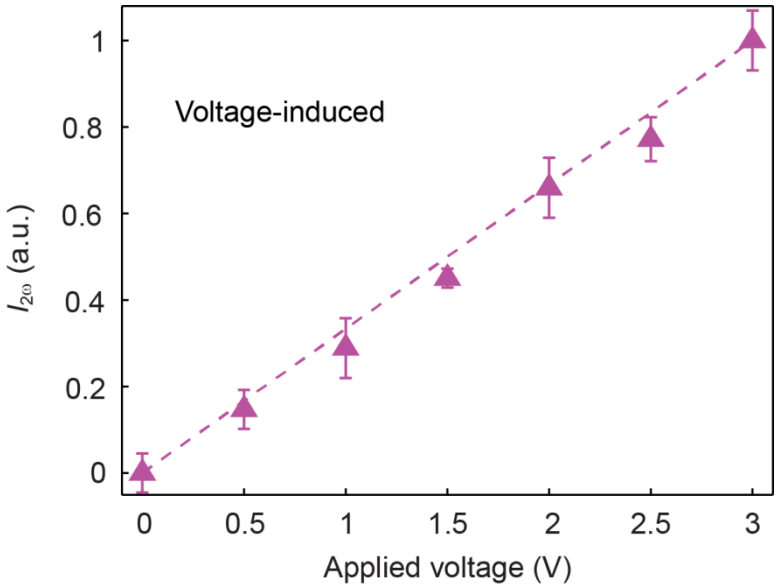

Figure 5.13. Electrically-induced SHG as a function of an externally applied voltage. Data are collected at the fundamental wavelength of $\lambda_\omega = 780$ nm.

two distinct dielectric media may further complicate the situation. Moreover, an extra loss factor included in the permittivity of nanostructured metals compared to that of bulk metals will cause a shorter propagation distance for the surface plasmon waves, especially the H-asymmetric mode at the second harmonic frequency. Nevertheless, the ultra-smooth dielectric films used in the experiment, fabricated by low pressure chemical vapor deposition and atomic layer deposition, respectively, ensure a device performance that agrees remarkably well with the prediction from the theoretical analysis and numerical simulations. The measured values of the spectral location ($\lambda_\omega = 780$ nm) and bandwidth ($\Delta\lambda_\omega \approx 30$ nm) for the backward phase matching in the plasmonic waveguide fits nicely with the theoretical quantities of $\lambda_\omega = 760$ nm and $\Delta\lambda_\omega \approx 25$ nm as illustrated

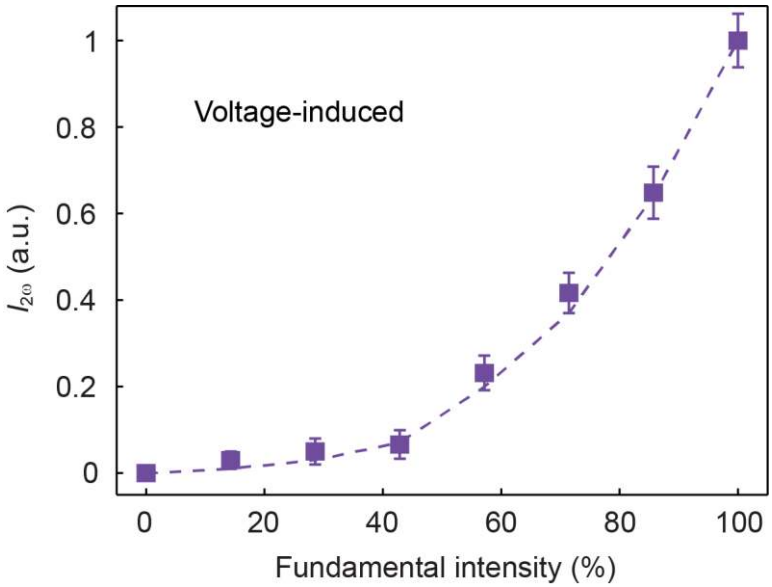

Figure 5.14. The dependence of the electrically-induced SHG intensity on the intensity of the fundamental light. The dashed curve depicts a quadratic function $I_{2\omega} \propto (I_{\omega})^2$. Error bars in all figures indicate the system uncertainty in the respective measurement.

in Figure 5.5. Just as momentum conservation leads to the requirement of phase matching for efficient nonlinear wave mixing, the law of energy conservation necessitates the Manley-Rowe relation, a fundamental rule in nonlinear optics that governs the rates of creation and annihilation of photons. For this reason, we anticipate that the total energy flux in a Manley-Rowe relation takes the unusual form of $|A_{\omega}|^2 - |A_{2\omega}|^2$ in our negative-index medium, where A_{ω} and $A_{2\omega}$ represent the electric field of the fundamental and harmonic waves, respectively [167]. This would be very different from the scenario in a conventional SHG process, where the Manley-Rowe relation describes the evolution of the sum, rather than the difference, of the squared amplitudes along the propagation direction of the fundamental wave [15].

5.5. Summary

In conclusion, we have experimentally verified the backward phase-matching condition for frequency doubling of light in optical negative index materials. This work represents a key case study of an entirely new regime for nonlinear optical processes in electromagnetic metamaterials, where many established rules have to be fundamentally modified to accommodate the unconventional material parameters not previously seen before. Results like this will drastically expand the scope of nonlinear light-matter interactions in artificially structured media with engineered, unconventional linear and higher-order material properties.

5.6. Methods

5.6.1 Sample preparation.

The fabrication of the device starts with an atomic layer deposition of HfO_2 onto an ultra-smooth Si_3N_4 membrane, followed by a metallization process to generate the silver layers, a focused ion beam (FIB) nanopatterning step to create the inlet/outlet-coupling nanoslit, and additional steps for electrical connections. The frame-supported nitride membrane, grown on a silicon wafer by low-pressure chemical vapor deposition and followed by etching away a window in the silicon substrate, has a thickness of 15 nm and a surface roughness of 0.65 nm. A HfO_2 layer 15 nm thick was coated onto the nitride membrane by an atomic layer deposition system (Cambridge NanoTech) to form the second sublayer and complete the core of the waveguide. Subsequently, a 140 nm thick silver layer was evaporated on the other side of the membrane using e-beam evaporation (CVC). Focus ion beam (FEI Nova Nanolab 200) was used to define a

nanoslit of 20 μm long through the silver layer of the Si_3N_4 side with a width of approximately 100 nm. The dielectric layers were not cut through during FIB milling so the two sides of the dielectric spacer remain electrically insulated. When the nanoslit was ready, a second silver film of 140 nm thick was evaporated on top of the HfO_2 layer using e-beam evaporation to complete the metal-dielectric-metal waveguide. Additional steps were carried out to connect the two metallic layers to opposite electrodes for electrical connection.

5.7. Supporting information

5.7.1. Locating the Operating Point

To set up a perfect phase matching condition in a plasmonic waveguide, with the mode refractive index of the second harmonic wave being negative, the relationship of $-n_{2\omega} = n_{\omega}$ has to be fulfilled. The dispersive mode refractive index in a metal-dielectric-metal (MIM) waveguide can be calculated by solving Maxwell's equations [66]. For an Ag-Si_3N_4-Ag waveguide with the thickness of Si_3N_4 being 40 nm, the mode refractive index is shown in Figure 5.15. The permittivity of silver is adopted from the tabulated data [151], and the refractive index of $n_d = 2$ is used for the dielectric layer. The maximum operational frequency (3.6 eV) is limited by the tunable range of the ultrafast laser (Ti:Sapphire) in the lab. Compared with the dispersion curves in Figure 5.2 in the manuscript where $t_{Si3N4} = 30$ nm, the operating point ($2\omega = 3.16$ eV) is much closer to the surface plasmon frequency ($\omega_p = 3.17$ eV). The $n_{2\omega}$ near ω_p changes rapidly with frequency while n_{ω} being relatively stable making them hard to balance with. Furthermore, the lost factor of the H-asymmetric mode increases sharply when operating

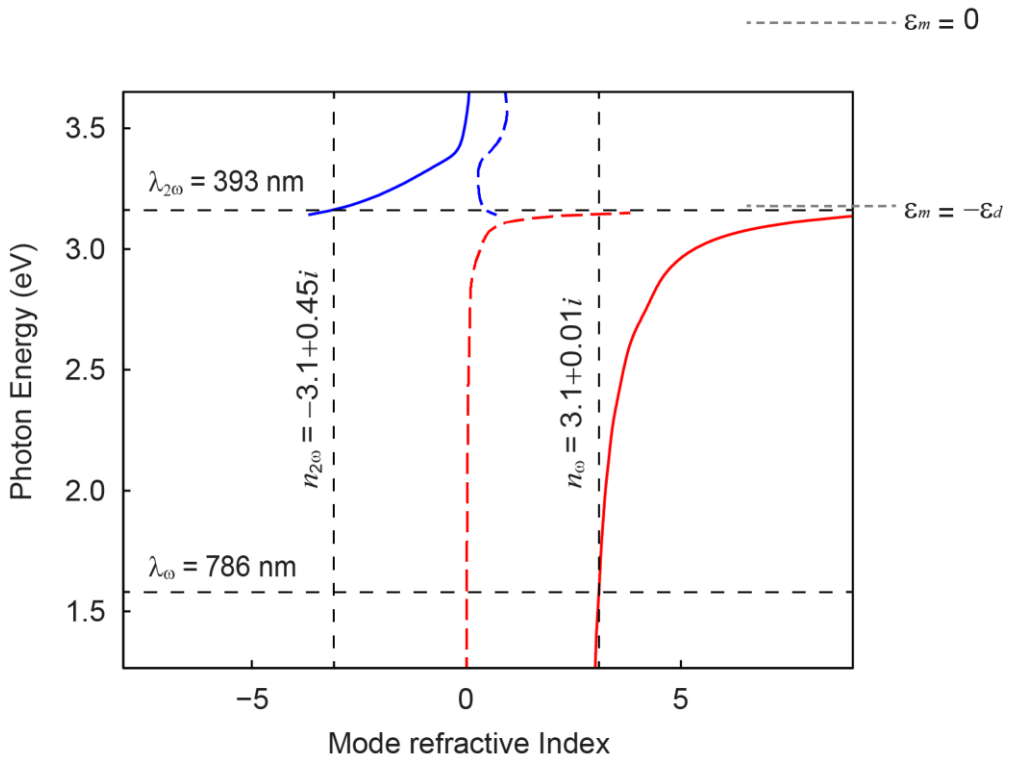

Figure 5.15. Dispersion of the mode refractive index in plasmonic waveguide. The thickness of the dielectric layer (Si_3N_4) is 40 nm. Both the real (solid) and imaginary (dashed) parts of the mode refractive index are plotted. The surface plasmon frequency ($\varepsilon_m = -\varepsilon_d$) is at 3.17 eV. The operating point indicated by the crossed dash lines is located at $2\omega = 3.16$ eV ($\lambda_{2\omega} = 393$ nm).

near the surface plasmon frequency. Thus, a thinner layer of dielectric (t_d = 30 nm) is designed for the experiments in the manuscript to have a perfectly phase matched operating point ($2\omega = 3.27$ eV) further away from ω_p.

5.7.2. Symmetric Breaking in Waveguide

The second harmonic intensity created in a nonlinear waveguide of length L due to wave-mixing from mode i at the fundamental wavelength λ_ω to mode j at the harmonic wavelength $\lambda_{2\omega}$ can be expressed as

$$I^{2\omega} \propto \left|P^{2\omega}\right|^2 \propto (S_{i,j})^2 L^2 \left(\frac{\sin(\Delta kL/2)}{\Delta kL/2}\right)^2 \left(\chi_{eff}^{(2)}\right)^2 I^{\omega}$$

Here superscripts ω and 2ω correspond to the fundamental and harmonic waves, respectively, I is the intensity, P is the nonlinear polarization, $\Delta k = k^{2\omega} - 2k^{\omega}$ represents the phase mismatch, $\chi_{eff}^{(2)}$ denotes the effective second-order susceptibility, and the nonlinear overlap factor $S_{i,j}$ describes the normalized spatial coupling coefficient defined as [165]:

$$S_{i,j} = \frac{\int_S \chi_{jii}^{(2)} E_j^{2\omega} E_i^{\omega} E_i^{\omega} dS}{\int_{\infty} E_i^{\omega} E_i^{\omega} dS \sqrt{\int_{\infty} \left(E_j^{2\omega}\right)^2 dS}}$$

The phase matching condition ($\Delta k = 0$) in this work is fulfilled by matching the mode refractive indices for λ_{ω} and $\lambda_{2\omega}$ in the plasmonic waveguide. The lacking of an efficient second-order susceptibility in centro-symmetric materials can be overcome by introducing a voltage-induced $\chi_{eff}^{(2)}$ as described in the main text.

Since the nonlinear generation efficiency is critically dependent on the nonlinear overlap factor, $I^{2\omega} \propto (S_{i,j})^2$, in the following section we describe our approach to optimize $S_{i,j}$ in this work. Assuming a uniform susceptibility $\chi^{(2)}$ exists in the core of the plasmonic waveguide, the nonlinear overlap factor $S_{i,j}$ is determined by the field integral $\int_S E_j^{2\omega} E_i^{\omega} E_i^{\omega} dS$ within the cross-section of the waveguide. In the proposed phase-matching scheme, which involves two modes of opposite symmetry, this integral is reduced to zero and no SHG should be expected. The scenario is better visualized in Figure 5.16, which shows the profiles of all field components of the H-symmetric mode

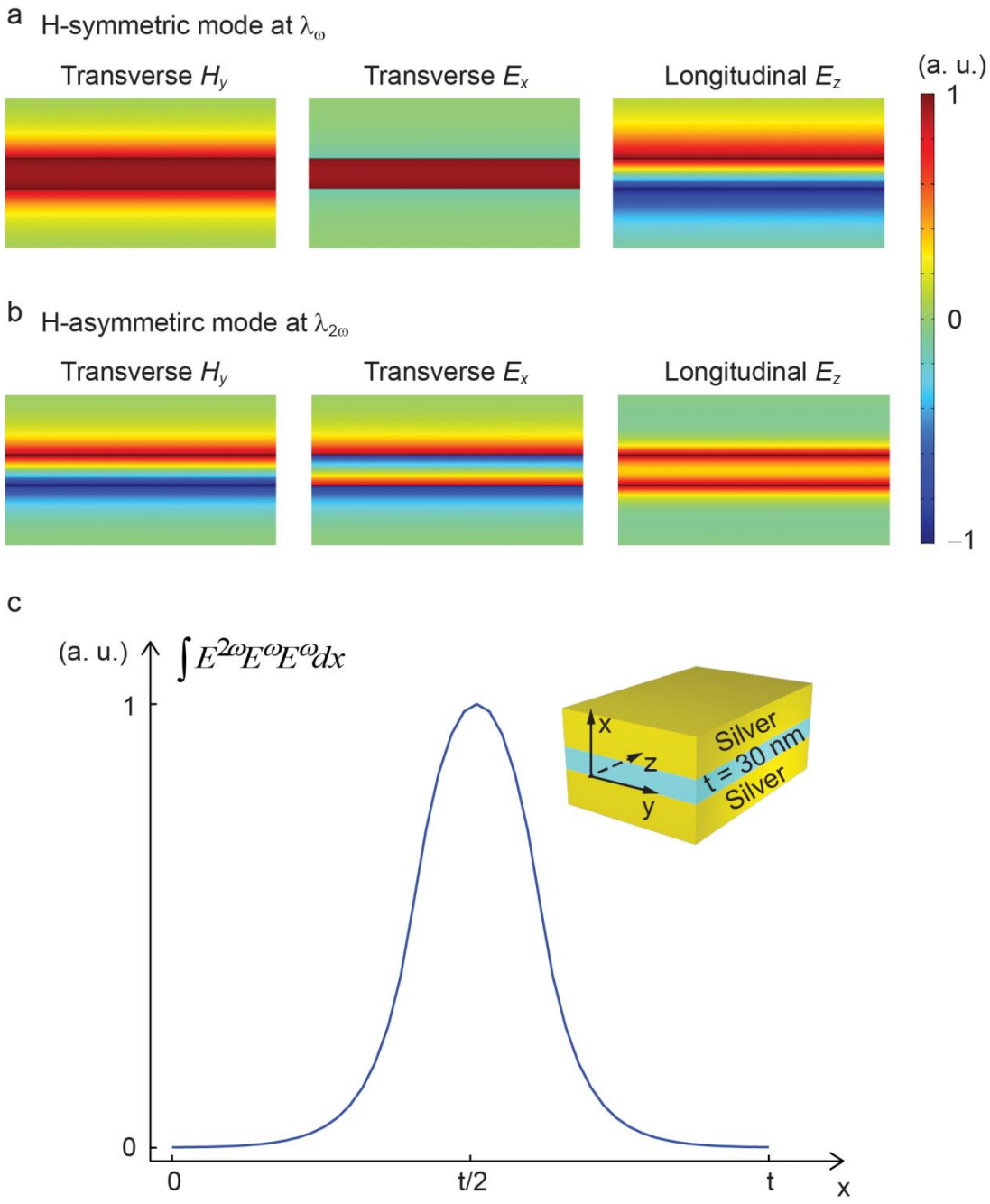

Figure 5.16. Nonlinear overlap factor and symmetric breaking in the plasmonic waveguide. The profiles of different field components are shown for (a) the fundamental wave at λ_ω = 760 nm and (b) the second harmonic wave at $\lambda_{2\omega}$ = 380 nm. (c) The field integral $\int E^{2\omega}E^{\omega}E^{\omega}dx$ within the cross-section.

at λ_ω and the H-asymmetric mode at $\lambda_{2\omega}$. Figure 5.16c illustrates how the integral $\int E^{2\omega} E^{\omega} E^{\omega} dx$ evolves along a direction perpendicular to the metal-dielectric layers. Due to the opposing symmetry between the two modes involved, the integral and consequently the nonlinear overlap factor $S_{i,j}$, reach the maximum value half-way into the waveguide core and then are reduced to zero when the entire waveguide cross-section is accounted. In order to circumvent this cancellation effect and enable efficient SHG in the waveguide, we purposely introduce a symmetric breaking mechanism by splitting the middle dielectric layer into two sub-layers with identical linear but distinct nonlinear properties. This way the effective susceptibility $\chi_{eff}^{(2)}$ of one of the sub-layer dominates over that of the other, and efficient wave-mixing is facilitated between the two modes of opposite symmetry.

In this work, Si_3N_4 and HfO_2 layers with the same thickness of 15 nm were used in our sample. Both Si_3N_4 and HfO_2 have a similar linear refractive index of approximately 2. Specifically, the values of the refractive index are $n_{\omega,Si3N4} = 2.0$; $n_{\omega,HfO2} = 2.09$; $n_{2\omega,Si3N4} = 2.07$, and $n_{2\omega,HfO2} = 2.16$ at the operating points (λ_ω = 780 nm and $\lambda_{2\omega}$ = 390 nm) [168, 169]. The $\chi^{(3)}$ nonlinear coefficient is approximately 3×10^{-21} m^2/V^2 for Si_3N_4 from the reference of [170]. The $\chi^{(3)}$ of HfO_2 is not readily available in the literature, and can be deduced from the magnitude and dispersion of the linear refractive index [171]. The value of $\chi^{(3)}$ for HfO_2 is hence estimated to be 8×10^{-22} m^2/V^2. The resistivity for the two dielectrics are $\rho_{Si3N4} \sim 10^{16}$ Ω·cm and $\rho_{HfO2} \sim 10^{12}$ Ω·cm [172, 173]. The value of $\chi^{(3)}\cdot\rho$ for Si_3N_4 is four orders larger than that for HfO_2. The voltage-induced $\chi_{eff}^{(2)}$ is mainly in the Si_3N_4 area dramatically breaking down the symmetry in the

waveguide. The exact value of the nonlinear susceptibility and electrical resistivity of thin films are very sensitive to the fabrication process. Therefore these values in the literature serve only as a reference. In our device, any nontrivial difference in $\chi^{(3)}\cdot\rho$ between the two dielectrics will lead to a notable difference in the voltage-induced $\chi_{eff}^{(2)}$, therefore result in distinct contributions to the frequency-double output ($I_{2\omega} \propto \left[\chi_{eff}^{(2)}\right]^2$).

5.7.3. Numerical Simulation

The modeling of the linear and nonlinear responses of the devices was developed in the frequency domain with a finite-element solver (COMSOL). The mode refractive index of the MIM waveguide is simulated in the mode analysis module of the solver. The exact same value was obtained with the simulation in the software and the calculation by solving Maxwell's equations. For example, at the wavelength of 760 nm in the Ag-Si_3N_4-Ag waveguide ($n_d = 2$, $\varepsilon_{Ag} = -27.34 - 0.314i$, $t_d = 30$ nm), the mode refractive index $n_{mode} = 3.4 - 0.01i$. The mode refractive index was used to deduce the degree of phase mismatching ($\Delta k/k_{0,\omega}$) in Figure 2c, where the perfectly phase matched point ($\Delta k/k_{0,\omega} = 0$) is addressed at $\lambda_\omega = 760$ nm.

To simulate the nonlinear response in plasmonic waveguide, two models (one at the frequency of ω and the other at 2ω) were established simultaneously with the mode coupling between the fundamental wave and the frequency-doubled signal through the nonlinear medium.[10] We assume that all the materials in the waveguide are homogeneous and exhibit bulk properties. As mentioned in the previous section, the voltage-induced SHG is mainly stems from the Si_3N_4 layer due to a much larger value of $\chi^{(3)}\cdot\rho$. The effective second order susceptibility $\chi_{eff}^{(2)} = 2 \times 10^{-12}$ m/V was assigned to the Si_3N_4 layer

with the externally applied voltage of 10 V in the model. The conversion efficiency, defined as the ratio of the generated harmonic power to the power of the fundamental plasmonic mode, is estimated to be 1×10^{-9}. However, for the investigation of the nonlinear response upon the phase matching condition specifically, the relative conversion efficiency of SHG when the phase matching condition holds (λ_ω = 760 nm and $\lambda_{2\omega}$ = 380 nm) compared to other wavelengths within the tuning range is more relevant and significant. The normalized relative conversion efficiency was shown in Figure 5.5, where the characteristic feature of phase matching with the maximum conversion efficiency at the perfectly backward-phase-matched point (λ_ω = 760 nm) is clearly indicated. In this case, a constant power at all the wavelengths of the fundamental wave was applied to the waveguide, and the forming of the H-symmetric mode, that is, the coupling of the wave from the free space to the waveguide core via the slit, was not accounted.

The far field coupling from air to the MIM waveguide for the fundamental wave was also simulated in the nonlinear device. The field profile of the H_z component (out of the plane) for the fundamental wave is shown in the Figure 5.17a. Besides, we simulated the symmetry breaking effect in the MIM waveguide (Figures 5.17b, right) with the scenario that fundamental wave was coupled into the system through the slit. With purposely introduced symmetry breaking (t_{Si3N4} = 15 nm, t_{HfO2} = 15 nm), the amplitude of the magnetic field is 10 times (10^2 times in terms of the power) larger than that with a single layer of Si_3N_4 (t_{Si3N4} = 30 nm). The similar result was obtained in the manuscript (Figure 5.6) without considering the far field coupling effect. The finite SHG from the symmetric dielectric core is the non-propagating modes locally generated in the

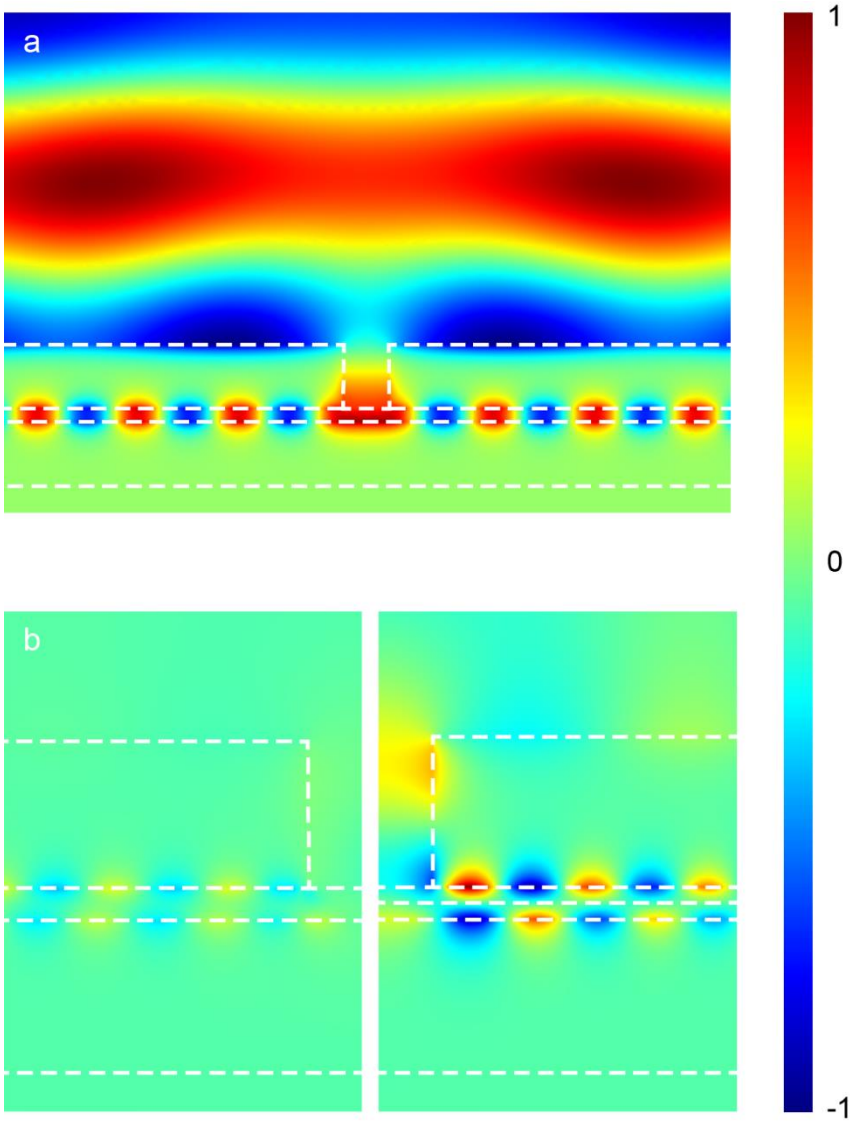

Figure 5.17. Far field coupling in the nonlinear optical device. H_z component (out of the plane) of the magnetic field is mapped (a) for the fundamental wave at λ_ω = 760 nm and (b) for the frequency-doubled light at $\lambda_{2\omega}$ = 380 nm. MIM waveguide with single uniform Si_3N_4 core (t_{Si3N4} = 30 nm) was used in the left panel. And the right panel is with two distinct dielectric layers (t_{Si3N4} = 15 nm, t_{HfO2} = 15 nm). White dashed lines are the geometric boundaries.

waveguide as clearly indicated in the left panel of Figure 5.17b. The nonlinear polarization at 2ω serves as local dipole source, which will couple to all modes supported in the waveguide. All but one (the H-asymmetric mode) of these modes at 2ω are not propagating, but they do exist locally and contribute to the non-zero field profile in Figure 5.6 (bottom).

5.7.4. Experimental Setup

The experimental setup for this study is illustrated in Figure 5.18. The fundamental light was from a Ti:Sapphire ultrafast oscillator (Spectra-Physics, Mai Tai HP) with a pulse duration of 100 fs, a repetition rate of 80 MHz, and a tuning range of 690 - 1040 nm. The output beam from the source first passes through a long-pass filter to

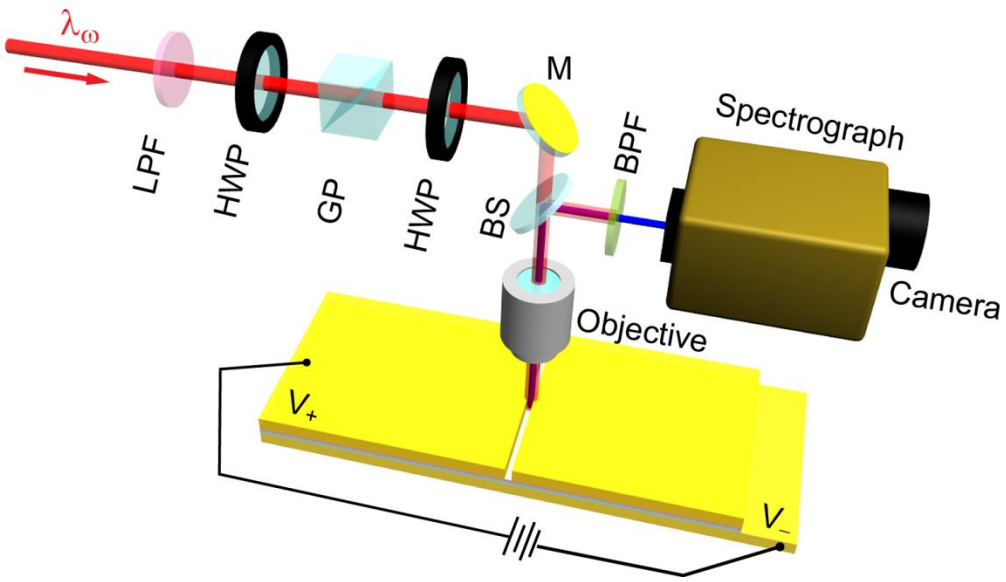

Figure 5.18. Experimental setup for the backward phase-matching measurements. Abbreviations for optical components: LPF – long-pass filter; HWP – half wave plate; GP – Glan polarizer; M – mirror; BS – beam splitter; BPF – band-pass filter.

prevent any high-frequency residue from entering later stages of the system. A set of Glan polarizers and half wave plates is employed to control the power level and polarization state of the excitation pulses. After passing through a beam splitter, the fundamental beam is delivered to the nonlinear plasmonic device mounted under an inverted optical microscope (Zeiss, Axio Observer D1m) with a 20× objective (NA = 0.5), which results in a spot size of approximately 50 μm on the sample. The generated signal from the sample is collected by the same objective and sent back to the beam splitter. A band-pass filter is placed in front of the spectrometer to eliminate the high-intensity fundamental waves. The detection system includes a monochromator (Princeton Instruments, IsoPlane) followed by a CCD camera (Princeton Instruments, Pixis). Nonlinear signals with and without an applied voltage were collected separately and the purely voltage-induced SHG component was extracted by further data processing.

5.7.5. Control Experiment

We performed a control experiment, where the core of the plasmonic waveguide is formed by a uniform layer of 30 nm Si_3N_4. Compared to the results using dual-layered waveguide core (t_{Si3N4} = 15 nm, t_{HfO2} = 15 nm), the SHG from the control experiment is only ~ 20% of the previous value at a fundamental wavelength of ~ 780 nm (Figure 5.19). This remaining SHG largely stems from the flat metal surface and the in-coupling slit, instead of the dielectric core of the MIM waveguide. More importantly, the resonance behavior in the SHG excitation spectrum, which serves as the fingerprint of the phase matching condition, disappeared in the null test (except a very small bump-like feature due to the residue symmetry-breaking in the 30 nm Si_3N_4 channel, because the two interfaces of the Si_3N_4 membrane have experienced different deposition and etching

conditions during the fabrication). The new control experiment evidences the need of purposely induced broken symmetry for the work.

5.7.6. Estimation of the Conversion Efficiency

Under the pump of an ultrafast laser at the wavelength of λ_ω = 780 nm, with the time averaged power of 168.5 mW, around 3000 photons per second of the frequency-doubled wave was detected with Si camera. Considering the laser spot size of 80 μm and the slit dimension being 100 nm × 20 μm, photons at the fundamental frequency on the level of 1×10^{14}/second were actually driving the nonlinear light-matter interaction. In

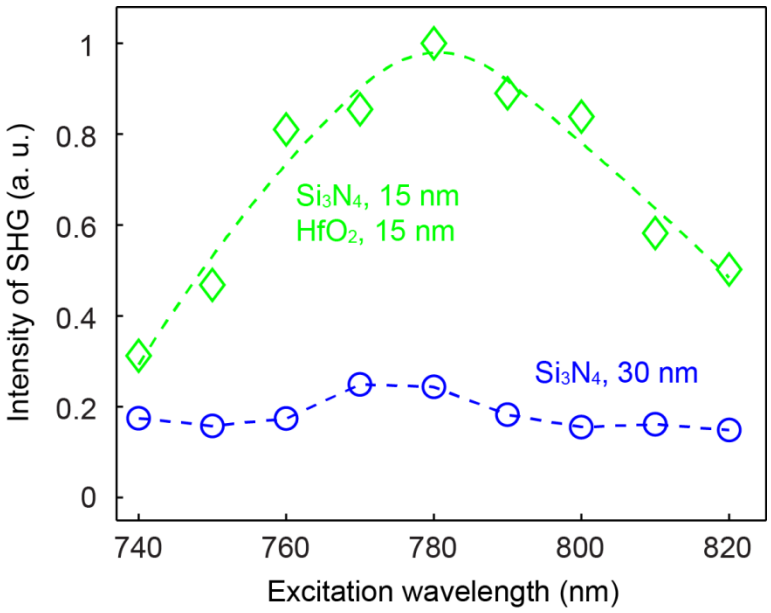

Figure 5.19. Control experiment without introduced symmetry breaking. Intensity of the SHG from uniform Si_3N_4 cored MIM waveguide (blue) is normalized to that with two dielectric layers (green) at λ_ω = 780 nm. The data (green and blue) are collected under the same experimental conditions. The dashed lines are the guide of an eye.

addition, the 20 × objective with N.A. = 0.5 can only collect a small portion of the light emitted from the nanoslit. Moreover, the photons collected by the objective experience optical loss before being detected by the camera. Thus the overall conversion efficiency for the static SHG was estimated to be 7.5×10^{-10}. The voltage-induced SHG is around 22% of the static SHG at the externally applied voltage of 3V. The conversion efficiency for voltage-induced SHG is 1.7×10^{-10}. Thanks to the phase matching condition, this conversion efficiency is around two orders larger than the previous work with similar scenarios [20, 50].

CHAPTER 6

CONCLUSION AND OUTLOOK

6.1. Conclusion

In this thesis, the ultimate goal is to have a single device that simultaneously sustains both electrical and optical functionalities. To achieve this goal, this research focuses on novel electrical and optical functionalities in plasmonic and metamaterial structures, in which nanostructured metals have used the strong spatial confinement of surface plasmon polaritons to harness enormous energy densities on their surfaces. In addition, plasmonic metamaterials are used as electrodes for the extraction of electrical energy and the manipulation of nonlinear optics in the metallic structures.

6.1.1. Electrical signal generation in plasmonic metamaterials

An optically driven change in carrier density in plasmonic nanostructures leads to the generation of electrostatic potential. This is demonstrated in Chapter 2 by designing a one-dimensional plasmonic diatomic grating with nonequivalent metallic stripes in each duty cycle. Under normal illumination, the asymmetric design expedited the excitation of a dark plasmonic mode that significantly suppresses radiation loss and features an ultra-sharp transmission peak not typically seen in plasmonic structures. In addition, because of the distinct thermodynamic behaviors of free carriers in adjacent metallic strips, the plasmonic grating yielded voltage drops across the gaps.

6.1.2. Electrically controlled nonlinear optics in plasmonic metamaterials

Recently, renewed interest has been directed towards two emerging trends in the research field of optical metamaterials, active control and nonlinear effects in these novel optical media. By exploring the interaction of these two directions, the electrical and optical functions supported in nanostructured metals are leveraged simultaneously in Chapter 3 demonstrating electrically-induced nonlinear optical processes from a metamaterial. Both second-harmonic generation and optical rectification, enhanced by the resonance behavior of the metamaterial absorber, are controlled by applied voltage signals. The results revealed the potential of metamaterials as a self-contained, dynamic electrooptic system with intrinsically embedded electrical functions and optical nonlinearities for signal processing, light switching, and sensing applications.

6.1.3. Tunable harmonic generation from plasmonic metamaterials in electrolytes

Electrically controlled nonlinear plasmonics is further pushed beyond the scope of solid-state structures in Chapter 4. This chapter describes how the tunable nonlinear generation of light is enabled by an electrically active plasmonic crystal in aqueous electrolytic solutions. A modulation depth of ~150 %/V in the second-harmonic signal is observed, thanks to the light concentrating ability of the resonant plasmonic structure as well as the voltage-assisted charge accumulation on the metallic surfaces. The hybrid plasmonic-electrolyte system demonstrated in this work offers an exciting new opportunity to use plasmonic nanostructures for voltage-controlled nonlinear signal generation and in-situ biochemical sensing in aqueous environments.

6.1.4. Backward phase-matching in negative-index materials

Metamaterials have enabled the realization of unconventional electromagnetic properties not found in nature, which has led us to rethink the established rules of optics in both linear and nonlinear regimes. One of the most intriguing phenomena in nonlinear metamaterials is "backward phase matching," also known as the "nonlinear mirror," which describes counter-propagating fundamental and harmonic waves in a negative-index medium. Predicted nearly a decade ago, this process was awaiting definitive experimental confirmation at optical frequencies. Backward phase matching is demonstrated in Chapter 5 by exploiting two distinct modes in an electrically controlled nonlinear plasmonic waveguide, in which the real parts of the mode refractive indices are 3.4 and −3.4 for fundamental and harmonic waves, respectively.

6.2. Outlook

Active nanophotonics enable diverse applications ranging from light generation to optical modulation, photon detection, or energy harvesting thanks to their light confinement at the nanoscale. The manipulation of optical, electrical, mechanical, and thermal energy in a unified manner will act as the toolset for multifunctional nanophotonic applications. Plasmonic and metamaterial devices can be used as an active platform to integrate nanophotonics with various functionalities by investigating photon-photon, photon-electron, and photon-phonon interactions.

6.2.1. Novel Optical and Electrical Functionalities

Plasmonic metamaterials possess exotic electrical and optical properties in both the linear and nonlinear regimes. In the linear regime, two intriguing research fields are the minimization of optical components and the active control of photonic devices. For the former, by applying phase-front engineering, the unique ability of metasurfaces, flat optical components can be developed for many applications such as the virtual and augmented reality. For the latter one, plasmonic metamaterials are perfect electrodes to simultaneously manipulate optical responses and collect electrical signals in a two-dimensional material systems. In the nonlinear regime, electrically induced even-order nonlinearities break the fundamental requirement of central symmetry in materials used in nonlinear optics. Unconventional nonlinear optical phenomena such as shaped harmonic generation and enhanced nonlinear spectroscopy can be developed by manipulating electric-field-induced nonlinearities.

6.2.2. Multifunctional Nanophotonics

Beyond optical and electrical energy, manipulating mechanical and thermal energy in a nanophotonic structure is promising for the application of sensing, imaging, and spectroscopy. Mechanical energy in an optical system arises from the radiation force of light, which leads to an optomechanical interaction length determined by the optical diffraction limit. Reintroducing plasmonics that breaks the diffraction limit in conjunction with electrical control facilitates the development of an unconventional plasmo-electro-mechanical system for precise measurements, mass sensing, and signal processing. Thermal energy transfer at the nanoscale is both challenging and intriguing.

Using evanescent optical fields, an asymmetric metamaterial device can replace the two materials in conventional systems to generate electrical energy with a relatively high efficiency.

REFERENCES

[1] P. A. Franken, A. E. Hill, C. W. Peters, G. Weinreich, Generation of optical harmonics. *Phys. Rev. Lett.* **7**, 118-119 (1961).

[2] T. H. Maiman, Stimulated optical radiation in ruby. *Nature* **187**, 493-494 (1960).

[3] W. Kaiser, C. G. B. Garrett, Two-photon excitation in CaF_2: Eu^{2+}. *Phys. Rev. Lett.* **7**, 229-231 (1961).

[4] J. A. Giordmaine, Mixing of light beams in crystals. *Phys. Rev. Lett.* **8**, 19-20 (1962).

[5] M. Bass, A. E. Hill, P. A. Franken, C. W. Peters, G. Weinreich, Optical mixing. *Phys. Rev. Lett.* **8**, 18 (1962).

[6] F. Zernike, P. R. Berman, Generation of far infrared as a difference frequency. *Phys. Rev. Lett.* **15**, 999-1001 (1965).

[7] N. Bloembergen, P. S. Pershan, Light waves at boundary of nonlinear media. *Phys. Rev.* **128**, 606-622 (1962).

[8] R. W. Terhune, P. D. Maker, C. M. Savage, Measurements of nonlinear light scattering. *Phys. Rev. Lett.* **14**, 681-684 (1965).

[9] C. C. Wang, G. W. Racette, Measurement of parametric gain accompanying optical difference frequency generation. *Appl. Phys. Lett.* **6**, 169-171 (1965).

[10] J. A. Giordmaine, R. C. Miller, Tunable coherent parametric oscillation in $LiNbO_3$ at optical frequencies. *Phys. Rev. Lett.* **14**, 973-976 (1965).

[11] N. M. Kroll, Parametric amplification in spatially extended media and application to design of tuneable oscillators at optical frequencies. *Phys. Rev.* **127**, 1207-1211 (1962).

[12] P. D. Maker, C. M. Savage, R. W. Terhune, M. Nisenoff, Effects of dispersion and focusing on production of optical harmonics. *Phys. Rev. Lett.* **8**, 21-22 (1962).

[13] J. A. Armstrong, N. Bloembergen, J. Ducuing, P. S. Pershan, Interactions between light waves in a nonlinear dielectric. *Phys. Rev.* **127**, 1918-1939 (1962).

[14] Y. R. Shen, *The Principles of Nonlinear Optics*. (John Wiley & Sons, New York, 1984).

[15] R. W. Boyd, *Nonlinear Optics, 3rd ed.*, (Academic Press, San Diego, 2008).

[16] P. A. Franken, J. F. Ward, Optical harmonics and nonlinear phenomena. *Rev. Mod. Phys.* **35**, 23-39 (1963).

[17] R. W. Minck, R. W. Terhune, C. C. Wang, Nonlinear optics. *Appl. Opt.* **5**, 1595-1612 (1966).

[18] G. D. Boyd, D. A. Kleinman, Parametric interaction of focused gaussian light beams. *J. Appl. Phys.* **39**, 3597-3639 (1968).

[19] R. W. Terhune, P. D. Maker, C. M. Savage, Optical harmonic generation in calcite. *Phys. Rev. Lett.* **8**, 404-406 (1962).

[20] W. Cai, A. P. Vasudev, M. L. Brongersma, Electrically controlled nonlinear generation of light with plasmonics. *Science* **333**, 1720-1723 (2011).

[21] M. Bass, J. F. Ward, G. Weinreich, P. A. Franken, Optical rectification. *Phys. Rev. Lett.* **9**, 446-448 (1962).

[22] J. F. Ward, J. K. Guha, Electric-field-induced optical rectification in nitrobenzene. *Appl. Phys. Lett.* **30**, 276-277 (1977).

[23] K. L. Sala, Nonlinear refractive-index phenomena in isotropic media subjected to a dc electric-field: exact solutions. *Phys. Rev. A* **29**, 1944-1956 (1984).

[24] D. H. Auston, K. P. Cheung, J. A. Valdmanis, D. A. Kleinman, Cherenkov radiation from femtosecond optical pulses in electro-optic media. *Phys. Rev. Lett.* **53**, 1555-1558 (1984).

[25] B. B. Hu, X. C. Zhang, D. H. Auston, P. R. Smith, Free-space radiation from electrooptic crystals. *Appl. Phys. Lett.* **56**, 506-508 (1990).

[26] A. Nahata, A. S. Weling, T. F. Heinz, A wideband coherent terahertz spectroscopy system using optical rectification and electro-optic sampling. *Appl. Phys. Lett.* **69**, 2321-2323 (1996).

[27] J. C. Maxwell Garnett, Colours in metal glasses and in metallic films. *Phil. Trans. R. Soc. Lond.* **203**, 385-420 (1904).

[28] Kretschm.E, H. Raether, Radiative decay of non radiative surface plasmons excited by light. *Z. Naturforsch. A.* **23**, 2135-2136 (1968).

[29] A. Otto, Excitation of nonradiative surface plasma waves in silver by method of frustrated total reflection. *Z. Phys.* **216**, 398-410 (1968).

[30] M. Fleischmann, P. J. Hendra, Mcquilla.Aj, Raman-spectra of pyridine adsorbed at a silver electrode. *Chem. Phys. Lett.* **26**, 163-166 (1974).

[31] T. W. Ebbesen, H. J. Lezec, H. F. Ghaemi, T. Thio, P. A. Wolff, Extraordinary optical transmission through sub-wavelength hole arrays. *Nature* **391**, 667-669 (1998).

[32] W. L. Barnes, A. Dereux, T. W. Ebbesen, Surface plasmon subwavelength optics. *Nature* **424**, 824-830 (2003).

[33] S. A. Maier, M. L. Brongersma, P. G. Kik, S. Meltzer, A. A. G. Requicha, H. A. Atwater, Plasmonics: A route to nanoscale optical devices. *Adv. Mat.* **13**, 1501-1505 (2001).

[34] H. J. Lezec, A. Degiron, E. Devaux, R. A. Linke, L. Martin-Moreno, F. J. Garcia-Vidal, T. W. Ebbesen, Beaming light from a subwavelength aperture. *Science* **297**, 820-822 (2002).

[35] D. A. Genov, A. K. Sarychev, V. M. Shalaev, Plasmon localization and local field distribution in metal-dielectric films. *Phys. Rev. E* **67**, 056611 (2003).

[36] E. Prodan, C. Radloff, N. J. Halas, P. Nordlander, A hybridization model for the plasmon response of complex nanostructures. *Science* **302**, 419-422 (2003).

[37] D. M. Wu, N. Fang, C. Sun, X. Zhang, W. J. Padilla, D. N. Basov, D. R. Smith, S. Schultz, Terahertz plasmonic high pass filter. *Appl. Phys. Lett.* **83**, 201-203 (2003).

[38] H. Shin, M. F. Yanik, S. H. Fan, R. Zia, M. L. Brongersma, Omnidirectional resonance in a metal-dielectric-metal geometry. *Appl. Phys. Lett.* **84**, 4421-4423 (2004).

[39] J. A. Dionne, K. Diest, L. A. Sweatlock, H. A. Atwater, Plasmostor: A metal-oxide-Si field effect plasmonic modulator. *Nano Lett.* **9**, 897-902 (2009).

[40] J. A. Schuller, E. S. Barnard, W. S. Cai, Y. C. Jun, J. S. White, M. L. Brongersma, Plasmonics for extreme light concentration and manipulation. *Nat. Mater.* **9**, 193-204 (2010).

[41] Y. C. Jun, K. C. Y. Huang, M. L. Brongersma, Plasmonic beaming and active control over fluorescent emission. *Nat. Commun.* **2**, 283 (2011).

[42] J. S. Q. Liu, R. A. Pala, F. Afshinmanesh, W. S. Cai, M. L. Brongersma, A submicron plasmonic dichroic splitter. *Nat. Commun.* **2**, 525 (2011).

[43] X. J. Ni, N. K. Emani, A. V. Kildishev, A. Boltasseva, V. M. Shalaev, Broadband light bending with plasmonic nanoantennas. *Science* **335**, 427-427 (2012).

[44] A. Melikyan, L. Alloatti, A. Muslija, D. Hillerkuss, P. C. Schindler, J. Li, R. Palmer, D. Korn, S. Muehlbrandt, D. Van Thourhout, B. Chen, R. Dinu, M. Sommer, C. Koos, M. Kohl, W. Freude, J. Leuthold, High-speed plasmonic phase modulators. *Nat. Photonics* **8**, 229-233 (2014).

[45] N. Engheta, Circuits with light at nanoscales: Optical nanocircuits inspired by metamaterials. *Science* **317**, 1698-1702 (2007).

[46] P. Berini, I. De Leon, Surface plasmon-polariton amplifiers and lasers. *Nat. Photonics* **6**, 16-24 (2012).

[47] D. K. Gramotnev, S. I. Bozhevolnyi, Plasmonics beyond the diffraction limit. *Nat. Photonics* **4**, 83-91 (2010).

[48] R. F. Oulton, V. J. Sorger, T. Zentgraf, R. M. Ma, C. Gladden, L. Dai, G. Bartal, X. Zhang, Plasmon lasers at deep subwavelength scale. *Nature* **461**, 629-632 (2009).

[49] M. A. Noginov, G. Zhu, A. M. Belgrave, R. Bakker, V. M. Shalaev, E. E. Narimanov, S. Stout, E. Herz, T. Suteewong, U. Wiesner, Demonstration of a spaser-based nanolaser. *Nature* **460**, 1110-1168 (2009).

[50] M. W. Klein, C. Enkrich, M. Wegener, S. Linden, Second-harmonic generation from magnetic metamaterials. *Science* **313**, 502-504 (2006).

[51] S. Kim, J. H. Jin, Y. J. Kim, I. Y. Park, Y. Kim, S. W. Kim, High-harmonic generation by resonant plasmon field enhancement. *Nature* **453**, 757-760 (2008).

[52] M. A. Foster, A. C. Turner, J. E. Sharping, B. S. Schmidt, M. Lipson, A. L. Gaeta, Broad-band optical parametric gain on a silicon photonic chip. *Nature* **441**, 960-963 (2006).

[53] J. Leuthold, C. Koos, W. Freude, Nonlinear silicon photonics. *Nat. Photonics* **4**, 535-544 (2010).

[54] J. Renger, R. Quidant, N. van Hulst, L. Novotny, Surface-enhanced nonlinear four-wave mixing. *Phys. Rev. Lett.* **104**, 046803 (2010).

[55] M. Kauranen, A. V. Zayats, Nonlinear plasmonics. *Nat. Photonics* **6**, 737-748 (2012).

[56] C. M. Soukoulis, M. Wegener, Past achievements and future challenges in the development of three-dimensional photonic metamaterials. *Nat. Photonics* **5**, 523-530 (2011).

[57] Y. R. Shen, Surface-properties probed by second-harmonic and sum-frequency generation. *Nature* **337**, 519-525 (1989).

[58] H. Suchowski, K. O'Brien, Z. J. Wong, A. Salandrino, X. B. Yin, X. Zhang, Phase mismatch-free nonlinear propagation in optical zero-index materials. *Science* **342**, 1223-1226 (2013).

[59] V. G. Veselago, Electrodynamics of substances with simultaneously negative values of ε and μ. *Sov. Phys. Usp.* **10**, 509-514 (1968).

[60] J. B. Pendry, Negative refraction makes a perfect lens. *Phys. Rev. Lett.* **85**, 3966-3969 (2000).

[61] R. A. Shelby, D. R. Smith, S. Schultz, Experimental verification of a negative index of refraction. *Science* **292**, 77-79 (2001).

[62] D. R. Smith, N. Kroll, Negative refractive index in left-handed materials. *Phys. Rev. Lett.* **85**, 2933-2936 (2000).

[63] V. M. Shalaev, W. S. Cai, U. K. Chettiar, H. K. Yuan, A. K. Sarychev, V. P. Drachev, A. V. Kildishev, Negative index of refraction in optical metamaterials. *Opt. Lett.* **30**, 3356-3358 (2005).

[64] S. Zhang, W. J. Fan, N. C. Panoiu, K. J. Malloy, R. M. Osgood, S. R. J. Brueck, Experimental demonstration of near-infrared negative-index metamaterials. *Phys. Rev. Lett.* **95**, 137404 (2005).

[65] H. J. Lezec, J. A. Dionne, H. A. Atwater, Negative refraction at visible frequencies. *Science* **316**, 430-432 (2007).

[66] S. A. Maier, *Plasmonics: Fundamentals and Applications*. (Springer, New York, 2007).

[67] W. Cai, V. M. Shalaev, *Optical Metamaterials: Fundamentals and Applications*. (Springer, New York, 2010).

[68] F. N. Xia, H. Wang, D. Xiao, M. Dubey, A. Ramasubramaniam, Two-dimensional material nanophotonics. *Nat. Photonics* **8**, 899-907 (2014).

[69] N. F. Yu, F. Capasso, Flat optics with designer metasurfaces. *Nat. Mater.* **13**, 139-150 (2014).

[70] H. A. Atwater, The promise of plasmonics. *Sci. Am.* **296**, 56-63 (2007).

[71] O. Hess, J. B. Pendry, S. A. Maier, R. F. Oulton, J. M. Hamm, K. L. Tsakmakidis, Active nanoplasmonic metamaterials. *Nat. Mater.* **11**, 573-584 (2012).

[72] J. N. Anker, W. P. Hall, O. Lyandres, N. C. Shah, J. Zhao, R. P. Van Duyne, Biosensing with plasmonic nanosensors. *Nat. Mater.* **7**, 442-453 (2008).

[73] T. Xu, Y. K. Wu, X. G. Luo, L. J. Guo, Plasmonic nanoresonators for high-resolution colour filtering and spectral imaging. *Nat. Commun.* **1**, 59 (2010).

[74] N. J. Halas, S. Lal, W. S. Chang, S. Link, P. Nordlander, Plasmons in strongly coupled metallic nanostructures. *Chem. Rev.* **111**, 3913-3961 (2011).

[75] M. V. Kovalenko, L. Manna, A. Cabot, Z. Hens, D. V. Talapin, C. R. Kagan, V. I. Klimov, A. L. Rogach, P. Reiss, D. J. Milliron, P. Guyot-Sionnnest, G. Konstantatos, W. J. Parak, T. Hyeon, B. A. Korgel, C. B. Murray, W. Heiss, Prospects of nanoscience with nanocrystals. *ACS Nano* **9**, 1012-1057 (2015).

[76] J. T. Li, S. K. Cushing, F. K. Meng, T. R. Senty, A. D. Bristow, N. Q. Wu, Plasmon-induced resonance energy transfer for solar energy conversion. *Nat. Photonics* **9**, 601-608 (2015).

[77] J. S. Miao, W. D. Hu, Y. L. Jing, W. J. Luo, L. Liao, A. L. Pan, S. W. Wu, J. X. Cheng, X. S. Chen, W. Lu, Surface plasmon-enhanced photodetection in few layer MoS_2 phototransistors with au nanostructure arrays. *Small* **11**, 2392-2398 (2015).

[78] C. P. Byers, B. S. Hoener, W. S. Chang, S. Link, C. F. Landes, Single-particle plasmon voltammetry (spPV) for detecting anion adsorption. *Nano Lett.* **16**, 2314-2321 (2016).

[79] B. L. Darby, B. Auguie, M. Meyer, A. E. Pantoja, E. C. Le Ru, Modified optical absorption of molecules on metallic nanoparticles at sub-monolayer coverage. *Nat. Photonics* **10**, 40-46 (2016).

[80] S. A. Maier, The benefits of darkness. *Nat. Mater.* **8**, 699-700 (2009).

[81] M. I. Stockman, Nanoscience: Dark-hot resonances. *Nature* **467**, 799-799 (2010).

[82] N. Liu, L. Langguth, T. Weiss, J. Kastel, M. Fleischhauer, T. Pfau, H. Giessen, Plasmonic analogue of electromagnetically induced transparency at the drude damping limit. *Nat. Mater.* **8**, 758-762 (2009).

[83] B. Luk'yanchuk, N. I. Zheludev, S. A. Maier, N. J. Halas, P. Nordlander, H. Giessen, C. T. Chong, The Fano resonance in plasmonic nanostructures and metamaterials. *Nat. Mater.* **9**, 707-715 (2010).

[84] S. Dobmann, A. Kriesch, D. Ploss, U. Peschel, Near-field analysis of bright and dark modes on plasmonic metasurfaces showing extraordinary suppressed transmission. *Adv. Opt. Mater.* **2**, 990-999 (2014).

[85] M. W. Chu, V. Myroshnychenko, C. H. Chen, J. P. Deng, C. Y. Mou, F. J. G. de Abajo, Probing bright and dark surface-plasmon modes in individual and coupled noble metal nanoparticles using an electron beam. *Nano Lett.* **9**, 399-404 (2009).

[86] W. Zhou, T. W. Odom, Tunable subradiant lattice plasmons by out-of-plane dipolar interactions. *Nat. Nanotechnol.* **6**, 423-427 (2011).

[87] S. C. Yang, H. Kobori, C. L. He, M. H. Lin, H. Y. Chen, C. C. Li, M. Kanehara, T. Teranishi, S. Gwo, Plasmon hybridization in individual gold nanocrystal dimers: Direct observation of bright and dark modes. *Nano Lett.* **10**, 632-637 (2010).

[88] G. Volpe, S. Cherukulappurath, R. J. Parramon, G. Molina-Terriza, R. Quidant, Controlling the optical near field of nanoantennas with spatial phase-shaped beams. *Nano Lett.* **9**, 3608-3611 (2009).

[89] D. E. Gomez, Z. Q. Teo, M. Altissimo, T. J. Davis, S. Earl, A. Roberts, The dark side of plasmonics. *Nano Lett.* **13**, 3722-3728 (2013).

[90] F. Hao, P. Nordlander, Y. Sonnefraud, P. Van Dorpe, S. A. Maier, Tunability of subradiant dipolar and Fano-type plasmon resonances in metallic ring/disk cavities: Implications for nanoscale optical sensing. *ACS Nano* **3**, 643-652 (2009).

[91] V. A. Fedotov, M. Rose, S. L. Prosvirnin, N. Papasimakis, N. I. Zheludev, Sharp trapped-mode resonances in planar metamaterials with a broken structural symmetry. *Phys. Rev. Lett.* **99**, 147401 (2007).

[92] S. Zhang, D. A. Genov, Y. Wang, M. Liu, X. Zhang, Plasmon-induced transparency in metamaterials. *Phys. Rev. Lett.* **101**, 047401 (2008).

[93] L. Kang, Y. Cui, S. Lan, S. P. Rodrigues, M. L. Brongersma, W. Cai, Electrifying photonic metamaterials for tunable nonlinear optics. *Nat. Commun.* **5**, 4680 (2014).

[94] S. Lan, L. Kang, D. T. Schoen, S. P. Rodrigues, Y. Cui, M. L. Brongersma, W. Cai, Backward phase-matching for nonlinear optical generation in negative-index materials. *Nat. Mater.* **14**, 807-811 (2015).

[95] L. Kang, S. Lan, Y. Cui, S. P. Rodrigues, Y. Liu, D. H. Werner, W. Cai, An active metamaterial platform for chiral responsive optoelectronics. *Adv. Mat.* **27**, 4377-4383 (2015).

[96] M. T. Sheldon, J. van de Groep, A. M. Brown, A. Polman, H. A. Atwater, Plasmoelectric potentials in metal nanostructures. *Science* **346**, 828-831 (2014).

[97] J. G. Webster, *The Measurement, Instrumentation, and Sensors Handbook*. The electrical engineering handbook series (CRC Press published in cooperation with IEEE Press, Boca Raton, 1999).

[98] F. J. Blatt, *Thermoelectric Power of Metals*. (Plenum Press, New York, 1976).

[99] J. Zhang, W. L. Bai, L. K. Cai, Y. Xu, G. F. Song, Q. Q. Gan, Observation of ultra-narrow band plasmon induced transparency based on large-area hybrid plasmon-waveguide systems. *Appl. Phys. Lett.* **99**, 181120 (2011).

[100] Y. M. Liu, X. Zhang, Metamaterials: A new frontier of science and technology. *Chem. Soc. Rev.* **40**, 2494-2507 (2011).

[101] D. R. Smith, J. B. Pendry, M. C. K. Wiltshire, Metamaterials and negative refractive index. *Science* **305**, 788-792 (2004).

[102] N. I. Zheludev, Y. S. Kivshar, From metamaterials to metadevices. *Nat. Mater.* **11**, 917-924 (2012).

[103] A. D. Boardman, V. V. Grimalsky, Y. S. Kivshar, S. V. Koshevaya, M. Lapine, N. M. Litchinitser, V. N. Malnev, M. Noginov, Y. G. Rapoport, V. M. Shalaev, Active and tunable metamaterials. *Laser Photonics Rev.* **5**, 287-307 (2011).

[104] H. T. Chen, W. J. Padilla, J. M. O. Zide, A. C. Gossard, A. J. Taylor, R. D. Averitt, Active terahertz metamaterial devices. *Nature* **444**, 597-600 (2006).

[105] G. A. Wurtz, R. Pollard, W. Hendren, G. P. Wiederrecht, D. J. Gosztola, V. A. Podolskiy, A. V. Zayats, Designed ultrafast optical nonlinearity in a plasmonic nanorod metamaterial enhanced by nonlocality. *Nat. Nanotechnol.* **6**, 106-110 (2011).

[106] E. Kim, F. Wang, W. Wu, Z. N. Yu, Y. R. Shen, Nonlinear optical spectroscopy of photonic metamaterials. *Phys. Rev. B* **78**, 113102 (2008).

[107] L. Luo, I. Chatzakis, J. G. Wang, F. B. P. Niesler, M. Wegener, T. Koschny, C. M. Soukoulis, Broadband terahertz generation from metamaterials. *Nat. Commun.* **5**, 3055 (2014).

[108] X. L. Liu, T. Starr, A. F. Starr, W. J. Padilla, Infrared spatial and frequency selective metamaterial with near-unity absorbance. *Phys. Rev. Lett.* **104**, 207403 (2010).

[109] K. Aydin, V. E. Ferry, R. M. Briggs, H. A. Atwater, Broadband polarization-independent resonant light absorption using ultrathin plasmonic super absorbers. *Nat. Commun.* **2**, 517 (2011).

[110] J. M. Hao, J. Wang, X. L. Liu, W. J. Padilla, L. Zhou, M. Qiu, High performance optical absorber based on a plasmonic metamaterial. *Appl. Phys. Lett.* **96**, 251104 (2010).

[111] N. Liu, M. Mesch, T. Weiss, M. Hentschel, H. Giessen, Infrared perfect absorber and its application as plasmonic sensor. *Nano Lett.* **10**, 2342-2348 (2010).

[112] F. Brown, R. E. Parks, A. M. Sleeper, Nonlinear optical reflection from a metallic boundary. *Phys. Rev. Lett.* **14**, 1029-1031 (1965).

[113] Y. R. Shen, Surface second-harmonic generation - a new technique for surface studies. *Annu. Rev. Mater. Sci.* **16**, 69-86 (1986).

[114] G. T. Boyd, Z. H. Yu, Y. R. Shen, Photoinduced luminescence from the noble-metals and its enhancement on roughened surfaces. *Phys. Rev. B* **33**, 7923-7936 (1986).

[115] A. Nahata, R. A. Linke, T. Ishi, K. Ohashi, Enhanced nonlinear optical conversion from a periodically nanostructured metal film. *Opt. Lett.* **28**, 423-425 (2003).

[116] M. Hentschel, M. Schaferling, T. Weiss, N. Liu, H. Giessen, Three-dimensional chiral plasmonic oligomers. *Nano Lett.* **12**, 2542-2547 (2012).

[117] A. Taflove, S. C. Hagness, *Computational Electrodynamics : The Finite-Difference Time-Domain Method*. Artech house antennas and propagation library (Artech House, Boston, 2005)

[118] T. W. Ebbesen, C. Genet, S. I. Bozhevolnyi, Surface-plasmon circuitry. *Phys. Today* **61**, 44-50 (2008).

[119] V. J. Sorger, R. F. Oulton, R. M. Ma, X. Zhang, Toward integrated plasmonic circuits. *MRS Bull.* **37**, 728-738 (2012).

[120] N. Liu, H. Giessen, Coupling effects in optical metamaterials. *Angew. Chem. Int. Edit.* **49**, 9838-9852 (2010).

[121] A. V. Krasavin, A. V. Zayats, Photonic signal processing on electronic scales: Electro-optical field-effect nanoplasmonic modulator. *Phys. Rev. Lett.* **109**, 053901 (2012).

[122] C. Haffner, W. Heni, Y. Fedoryshyn, J. Niegemann, A. Melikyan, D. L. Elder, B. Baeuerle, Y. Salamin, A. Josten, U. Koch, C. Hoessbacher, F. Ducry, L. Juchli, A. Emboras, D. Hillerkuss, M. Kohl, L. R. Dalton, C. Hafner, J. Leuthold, All-plasmonic Mach-Zehnder modulator enabling optical high-speed communication at the microscale. *Nat. Photonics* **9**, 525-528 (2015).

[123] Z. L. Samson, K. F. MacDonald, F. De Angelis, B. Gholipour, K. Knight, C. C. Huang, E. Di Fabrizio, D. W. Hewak, N. I. Zheludev, Metamaterial electro-optic switch of nanoscale thickness. *Appl. Phys. Lett.* **96**, 143105 (2010).

[124] A. Minovich, J. Farnell, D. N. Neshev, I. McKerracher, F. Karouta, J. Tian, D. A. Powell, I. V. Shadrivov, H. H. Tan, C. Jagadish, Y. S. Kivshar, Liquid crystal based nonlinear fishnet metamaterials. *Appl. Phys. Lett.* **100**, 121113 (2012).

[125] H. J. Park, T. Xu, J. Y. Lee, A. Ledbetter, L. J. Guo, Photonic color filters integrated with organic solar cells for energy harvesting. *ACS Nano* **5**, 7055-7060 (2011).

[126] S. Y. Chou, W. Ding, Ultrathin, high-efficiency, broad-band, omni-acceptance, organic solar cells enhanced by plasmonic cavity with subwavelength hole array. *Opt. Express* **21**, A60-A76 (2013).

[127] A. S. Vengurlekar, T. Ishihara, Surface plasmon enhanced photon drag in metal films. *Appl. Phys. Lett.* **87**, 091118 (2005).

[128] N. Noginova, V. Rono, F. J. Bezares, J. D. Caldwell, Plasmon drag effect in metal nanostructures. *New J. Phys.* **15**, 113061 (2013).

[129] O. A. Aktsipetrov, A. A. Fedyanin, V. N. Golovkina, T. V. Murzina, Optical second-harmonic generation induced by a dc electric field at the Si-SiO_2 interface. *Opt. Lett.* **19**, 1450-1452 (1994).

[130] A. Nahata, T. F. Heinz, J. A. Misewich, High-speed electrical sampling using optical second-harmonic generation. *Appl. Phys. Lett.* **69**, 746-748 (1996).

[131] D. Xiao, E. Ramsay, D. T. Reid, B. Offenbeck, N. Weber, Optical probing of a silicon integrated circuit using electric-field-induced second-harmonic generation. *Appl. Phys. Lett.* **88**, 114107 (2006).

[132] S. P. Rodrigues, W. Cai, Nonlinear optics: Tuning harmonics with excitons. *Nat. Nanotechnol.* **10**, 387-388 (2015).

[133] B. F. Levine, C. G. Bethea, Molecular hyperpolarizabilities determined from conjugated and nonconjugated organic liquids. *Appl. Phys. Lett.* **24**, 445-447 (1974).

[134] O. Ostroverkhova, A. Stickrath, K. D. Singer, Electric field-induced second harmonic generation studies of chromophore orientational dynamics in photorefractive polymers. *J. Appl. Phys.* **91**, 9481-9486 (2002).

[135] W. Ding, L. C. Zhou, S. Y. Chou, Enhancement and electric charge-assisted tuning of nonlinear light generation in bipolar plasmonics. *Nano Lett.* **14**, 2822-2830 (2014).

[136] K. L. Seyler, J. R. Schaibley, P. Gong, P. Rivera, A. M. Jones, S. F. Wu, J. Q. Yan, D. G. Mandrus, W. Yao, X. D. Xu, Electrical control of second-harmonic generation in a WSe_2 monolayer transistor. *Nat. Nanotechnol.* **10**, 407-411 (2015).

[137] A. G. Brolo, R. Gordon, B. Leathem, K. L. Kavanagh, Surface plasmon sensor based on the enhanced light transmission through arrays of nanoholes in gold films. *Langmuir* **20**, 4813-4815 (2004).

[138] J. M. McMahon, J. Henzie, T. W. Odom, G. C. Schatz, S. K. Gray, Tailoring the sensing capabilities of nanohole arrays in gold films with rayleigh anomaly-surface plasmon polaritons. *Opt. Express* **15**, 18119-18129 (2007).

[139] A. A. Yanik, M. Huang, O. Kamohara, A. Artar, T. W. Geisbert, J. H. Connor, H. Altug, An optofluidic nanoplasmonic biosensor for direct detection of live viruses from biological media. *Nano Lett.* **10**, 4962-4969 (2010).

[140] C. C. Wang, Second-harmonic generation of light at boundary of an isotropic medium. *Phys. Rev.* **178**, 1457-1461 (1969).

[141] H. J. Simon, D. E. Mitchell, J. G. Watson, Optical second-harmonic generation with surface plasmons in silver films. *Phys. Rev. Lett.* **33**, 1531-1534 (1974).

[142] P. Guyotsionnest, W. Chen, Y. R. Shen, General considerations on optical second-harmonic generation from surfaces and interfaces. *Phys. Rev. B* **33**, 8254-8263 (1986).

[143] R. M. Corn, D. A. Higgins, Optical second-harmonic generation as a probe of surface-chemistry. *Chem. Rev.* **94**, 107-125 (1994).

[144] C. K. Chen, T. F. Heinz, D. Ricard, Y. R. Shen, Equilibrium and transient study of adsorption of pyridine on silver in an electrolytic solution. *Chem. Phys. Lett.* **83**, 455-458 (1981).

[145] A. Hamelin, T. Vitanov, E. Sevastyanov, A. Popov, The electrochemical double-layer on sp metal single-crystals - the current status of data. *J. Electroanal Chem.* **145**, 225-264 (1983).

[146] G. L. Richmond, Optical second-harmonic generation as a surface probe of silver electrodes. *Surf. Sci.* **147**, 115-126 (1984).

[147] H. M. Rojhantalab, G. L. Richmond, Characterization of the silver aqueous-electrolyte interface by optical second- harmonic generation and differential capacitance. *J. Phys. Chem.* **93**, 3269-3275 (1989).

[148] G. L. Richmond, Characterization of the silver aqueous-electrolyte interface by optical second-harmonic generation. *Langmuir* **2**, 132-139 (1986).

[149] R. M. Corn, M. Romagnoli, M. D. Levenson, M. R. Philpott, Second-harmonic generation at thin-film silver electrodes via surface-polaritons. *J. Chem. Phys.* **81**, 4127-4132 (1984).

[150] P. Guyotsionnest, A. Tadjeddine, Study of Ag(111) and Au(111) electrodes by optical second-harmonic generation. *J. Chem. Phys.* **92**, 734-738 (1990).

[151] P. B. Johnson, R. W. Christy, Optical-constants of noble-metals. *Phys. Rev. B* **6**, 4370-4379 (1972).

[152] V. M. Shalaev, Optical negative-index metamaterials. *Nat. Photonics* **1**, 41-48 (2007).

[153] N. Meinzer, W. L. Barnes, I. R. Hooper, Plasmonic meta-atoms and metasurfaces. *Nat. Photonics* **8**, 889-898 (2014).

[154] M. Lapine, I. V. Shadrivov, Y. S. Kivshar, Colloquium: Nonlinear metamaterials. *Rev. Mod. Phys.* **86**, 1093-1123 (2014).

[155] S. Linden, F. B. P. Niesler, J. Forstner, Y. Grynko, T. Meier, M. Wegener, Collective effects in second-harmonic generation from split-ring-resonator arrays. *Phys. Rev. Lett.* **109**, 015502 (2012).

[156] J. Reinhold, M. R. Shcherbakov, A. Chipouline, V. I. Panov, C. Helgert, T. Paul, C. Rockstuhl, F. Lederer, E. B. Kley, A. Tunnermann, A. A. Fedyanin, T. Pertsch, Contribution of the magnetic resonance to the third harmonic generation from a fishnet metamaterial. *Phys. Rev. B* **86**, 115401 (2012).

[157] D. B. Anderson, J. T. Boyd, Wideband CO_2 laser second harmonic generation phase matched in gaas thin-film waveguides. *Appl. Phys. Lett.* **19**, 266-268 (1971).

[158] A. Yariv, Coupled-mode theory for guided-wave optics. *IEEE J. Quantum Electron.* **Qe 9**, 919-933 (1973).

[159] H. Shin, S. H. Fan, All-angle negative refraction for surface plasmon waves using a metal-dielectric-metal structure. *Phys. Rev. Lett.* **96**, 073907 (2006).

[160] A. Alu, N. Engheta, Optical nanotransmission lines: Synthesis of planar left-handed metamaterials in the infrared and visible regimes. *J. Opt. Soc. Am. B* **23**, 571-583 (2006).

[161] J. A. Dionne, E. Verhagen, A. Polman, H. A. Atwater, Are negative index materials achievable with surface plasmon waveguides? A case study of three plasmonic geometries. *Opt. Express* **16**, 19001-19017 (2008).

[162] E. Feigenbaum, N. Kaminski, M. Orenstein, Negative dispersion: A backward wave or fast light? Nanoplasmonic examples. *Opt. Express* **17**, 18934-18939 (2009).

[163] T. Yang, K. B. Crozier, Analysis of surface plasmon waves in metal-dielectric-metal structures and the criterion for negative refractive index. *Opt. Express* **17**, 1136-1143 (2009).

[164] E. Verhagen, R. de Waele, L. Kuipers, A. Polman, Three-dimensional negative index of refraction at optical frequencies by coupling plasmonic waveguides. *Phys. Rev. Lett.* **105**, 223901 (2010).

[165] G. I. Stegeman, C. T. Seaton, Nonlinear integrated-optics. *J. Appl. Phys.* **58**, R57-R78 (1985).

[166] H. Ito, H. Inaba, Efficient phase-matched second-harmonic generation method in four-layered optical-waveguide structure. *Opt. Lett.* **2**, 139-141 (1978).

[167] A. K. Popov, V. M. Shalaev, Negative-index metamaterials: Second-harmonic generation, Manley-Rowe relations and parametric amplification. *Appl. Phys. B* **84**, 131-137 (2006).

[168] H. R. Philipp, Optical properties of silicon-nitride. *J. Electrochem. Soc.* **120**, 295-300 (1973).

[169] D. L. Wood, K. Nassau, T. Y. Kometani, D. L. Nash, Optical-properties of cubic hafnia stabilized with yttria. *Appl. Opt.* **29**, 604-607 (1990).

[170] K. Ikeda, R. E. Saperstein, N. Alic, Y. Fainman, Thermal and Kerr nonlinear properties of plasma-deposited silicon nitride/silicon dioxide waveguides. *Opt. Express* **16**, 12987-12994 (2008).

[171] N. L. Boling, A. J. Glass, A. Owyoung, Empirical relationships for predicting non-linear refractive-index changes in optical solids. *IEEE J. Quantum Electron.* **14**, 601-608 (1978).

[172] Y. Nishi, R. Doering, *Handbook of Semiconductor Manufacturing Technology*. (Marcel Dekker, New York, 2000)

[173] E. Hildebrandt, J. Kurian, M. M. Muller, T. Schroeder, H. J. Kleebe, L. Alff, Controlled oxygen vacancy induced p-type conductivity in HfO_2-x thin films. *Appl. Phys. Lett.* **99**, 112902 (2011).

VITA

SHOUFENG LAN

Shoufeng Lan began his scientific career in Tianjin University, where he completed a Bachelor of Engineering in Optoelectronic Science and Technology for a joint program with Nankai University in 2007. He studied polarization-multiplexing in fiber telecommunication systems for his undergraduate research. He was promoted as an entrance-exam-free master student in Tianjin University, where he worked on all-fiber optical coherent tomography systems for the diagnosis of cavities in human teeth and he received the M.E. degree in Optical Engineering in 2009. He received his second master degree (M.S.) in Optical Science and Engineering from the University of New Mexico in 2011. His research at UNM focused on the physics and applications, such as optomechanics, of ultra-high quality factor microresonators. In 2012, he joined the Laboratory of Advanced Photonics and Optics (LAPO) led by Professor Wenshan Cai at the Georgia Institute of Technology. His doctoral research focused on plasmonics and metamaterials, specifically, exploring metallic nanostructures for the development of devices that simultaneously support both optical and electrical functionalities. In recognization of his accomplishment, he received the Materials Research Society (MRS) Graduate Student Award (2015), the Chinese Government Award for Outstanding Students Abroad (2015), and the DJ Lovell Scholarship (2016) from the International Society for Optics and Photonics (SPIE).

PUBLICATIONS

Journal articles corresponding to this dissertation:

1. S. Lan,* S. P. Rodrigues,* M. Taghinejad, W. Cai, "Dark plasmonic modes in diatomic gratings for plasmoelectronics," *Laser & Photonics Reviews*, in press, 2017. (**Chapter 2**)

2. L. Kang,* Y. Cui,* S. Lan,* S. P. Rodrigues, M. L. Brongersma, W. Cai, "Electrifying photonic metamaterials for tunable nonlinear optics," *Nature Communications*, 5, 4680, 2014. (**Chapter 3**)

3. S. Lan, S. P. Rodrigues, Y. Cui, L. Kang, W. Cai, "Electrically tunable harmonic generation of light from plasmonic structures in electrolytes," *Nano Letters*, 16, 5074-5079, 2016. (**Chapter 4**)

4. S. Lan, L. Kang, D. T. Schoen, S. P. Rodrigues, Y. Cui, M. L. Brongersma, W. Cai, "Backward phase-matching for nonlinear optical generation in negative-index materials," *Nature Materials*, 14, 807-811, 2015. (**Chapter 5**)

Other publications for the doctoral research:

1. S. P. Rodrigues,* S. Lan,* L. Kang, Y. Cui, P. Panuski, S. Wang, A. M. Urbas, W. Cai, "Intensity-dependent modulation of optically active signals in a chiral metamaterial," *Nature Communications*, 8, 14602, 2017.

2. X. Wang, S. Lan, "Optical properties of black phosphorus," *Advances in Optics and Photonics*, 8, 618-655, 2016. (Invited Paper)

3. S. Lan, S. P. Rodrigues, L. Kang, W. Cai, "Visualizing optical phase anisotropy in black phosphorus," *ACS Photonics*, 3, 1176-1181, 2016.

4. S. Lan, S. P. Rodrigues, W. Cai, "Backward phase-matching: rethinking nonlinear optical rules," *SPIE Newsroom*, DOI: 10.1117/2.1201508.006089, 2015. (Invited Paper)

5. L. Kang,* S. Lan,* Y. Cui,* S. P. Rodrigues, Y. Liu, D. H. Werner, W. Cai, "An active metamaterial platform for chiral responsive optoelectronics," *Advanced Materials*, 27, 4377-4383, 2015.

6. S. P. Rodrigues, Y. Cui, S. Lan, L. Kang, W. Cai, "Metamaterials enable chiral-selective enhancement of two-photon excitation from quantum emitters," *Advanced Materials*, 27, 1124-1130, 2015.

7. S. P. Rodrigues, S. Lan, L. Kang, Y. Cui, W. Cai, "Nonlinear imaging and spectroscopy of chiral metamaterials," *Advanced Materials*, 26, 6157-6162, 2014.

8. Y. Cui, L. Kang, S. Lan, S. P. Rodrigues, W. Cai, "Giant chiral optical response from a twisted-arc metamaterial," *Nano Letters*, 14, 1021-1025, 2014.

* Authors contributed equally to this work